UNIVERSITI TEKNOLOGI MARA

# FABRICATION AND CHARACTERISATION OF TIN-POLYDIMETHYLSILOXANE (PDMS) COMPOSITE BY LAYERING TECHNIQUE FOR RADIATION ABSORPTION APPLICATIONS

NURUL SYAFIQAH BINTI ROSLAN

MSc

September 2026

# UNIVERSITI TEKNOLOGI MARA

# FABRICATION AND CHARACTERISATION OF TIN-POLYDIMETHYLSILOXANE (PDMS) COMPOSITE BY LAYERING TECHNIQUE FOR RADIATION ABSORPTION APPLICATIONS

**NURUL SYAFIQAH BINTI ROSLAN**

Thesis submitted in fulfilment
of the requirements for the degree of
**Master of Science**
**(Material Science and Technology)**

**Faculty of Applied Sciences**

**September 2026**

# CONFIRMATION BY PANEL OF EXAMINERS

I certify that a Panel of Examiners has met on 27 July 2026 to conduct the final examination of Nurul Syafiqah Binti Roslan on her Master of Science thesis entitled "Fabrication and Characterisation of Tin-Polydimethylsiloxane (PDMS) Composite by Layering Technique for Radiation Shielding Applications" in accordance with Universiti Teknologi MARA Act 1976 (Akta 173). The Panel of Examiners recommends that the student be awarded the relevant degree. The Panel of Examiners was as follows:

Wan Izhan Nawawi Wan Ismail, PhD
Associate Professor
Faculty of Applied Sciences
Universiti Teknologi MARA
(Chairman)

Nor Aziyah Bakhari, PhD
Associate Professor
Faculty of Applied Sciences
Universiti Teknologi MARA
(Internal Examiner)

Wan Nordiana Wan Abd Rahman, PhD
Senior Lecturer
Faculty of Applied Physics
Universiti Kebangsaan Malaysia
(External Examiner)

**PROF DR HJH ZURAEDA IBRAHIM**
Dean
Institute of Postgraduate Studies
Universiti Teknologi MARA

Date: 18 September 2026

# AUTHOR'S DECLARATION

I declare that the work in this thesis was carried out in accordance with the regulations of Universiti Teknologi MARA. It is original and is the results of my own work, unless otherwise indicated or acknowledged as referenced work. This thesis has not been submitted to any other academic institution or non-academic institution for any degree or qualification.

I, hereby, acknowledge that I have been supplied with the Academic Rules and Regulations for Postgraduate, Universiti Teknologi MARA, regulating the conduct of my study and research.

| | | |
|---|---|---|
| Name of Student | : | Nurul Syafiqah Binti Roslan |
| Student ID. No. | : | 2024592857 |
| Programme | : | Master of Science (Material Science and Technology) – AS762 |
| Faculty | : | Applied Sciences |
| Thesis Title | : | Fabrication and Characterisation of Tin-Polydimethylsiloxane (PDMS) Composite by Layering Technique for Radiation Shielding Applications |
| Signature of Student | : | . …….. |
| Date | : | September 2026 |

# ABSTRACT

Lead is widely used as a radiation shielding material due to its high atomic number and density. However, its toxicity, excessive weight, and environmental hazards have motivated the search for safer and more sustainable alternatives. In this study, double-layered tin-polydimethylsiloxane (PDMS) composites were fabricated using pure tin and tin alloy fillers at concentrations of 10 to 60 wt% by layering technique. The objective was to develop lightweight, flexible, and non-toxic radiation shielding materials with attenuation performance comparable to conventional lead. Comprehensive characterisation was conducted to evaluate the physical, structural, and radiation attenuation properties of the fabricated composites. Increasing metal filler content resulted in higher effective density, reaching a maximum of 5.32 g cm-3 for the TM6 composite. Field Emission Scanning Electron Microscopy with Energy Dispersive X-ray Spectroscopy (FESEM-EDX) revealed uniform filler dispersion and strong interfacial adhesion without significant agglomeration. X-ray Diffraction (XRD) confirmed the presence of crystalline tin and tin alloy phases, while Fourier Transform Infrared Spectroscopy (FTIR) indicated the absence of chemical bonding between the fillers and the PDMS matrix, suggesting physical interactions within the composites. Gamma-ray attenuation measurements were performed over photon energies ranging from 59.5 to 1332.5 keV. Shielding performance improved with increasing filler loading, with the TM6 tin irradiation surface exhibiting the highest attenuation capability, achieving a linear attenuation coefficient (LAC) of 16.811 $cm^{-1}$, mass attenuation coefficient (MAC) of 3.160 $cm^2$ $g^{-1}$, half-value layer (HVL) of 0.041 cm, tenth-value layer (TVL) of 0.137 cm, and radiation protection efficiency (RPE) of 96.53% at 88.0 keV. Although TM6 demonstrated the highest overall shielding performance, the TM5 alloy irradiation surface provided a more favourable balance between shielding efficiency and material thickness, achieving an RPE of 41.36% with a lead-equivalent thickness (tPb) of 0.87 mmPb at 356.0 keV. These findings identify TM6 as the optimized composite for maximum radiation attenuation, while TM5 offers a practical compromise between shielding effectiveness and reduced material thickness. Overall, the layered tin–PDMS composites demonstrate strong potential as lead-free radiation shielding materials for applications in medical imaging, nuclear facilities, and aerospace environments.

# ACKNOWLEDGEMENT

Alhamdulillah, all praise to Allah for granting me the strength, patience, and perseverance to complete this thesis.

I would like to express my deepest and most sincere gratitude to my supervisor, Dr. Ainorkhilah Mahmood, for her invaluable guidance, patience, and continuous encouragement throughout this research. Her expertise, insightful feedback, and unwavering support have been instrumental in shaping the direction and quality of my work. My heartfelt thanks also go to my co-supervisor, Ms.Nor Aimi Abdul Wahab, whose advice, encouragement, and constructive input have greatly enriched this study.

Special appreciation is extended to my project leader, Mrs. Nur Maizatul Azra Mukhtar, and research team member, Hanisah Zainal Abidin, for their teamwork, knowledge sharing, and encouragement throughout this project.

I would like to express my sincere gratitude to Mrs. Aishah Zarzali Shah from Universiti Putra Malaysia (UPM) for her assistance with FTIR analysis. My appreciation also goes to Ts. Dr. Mohd Idzat Idris and En. Tazidi Taib from Universiti Kebangsaan Malaysia (UKM) for the invaluable support in radiation characterisation experiments. I am deeply thankful to Professor Dr. Ahmad Azmin Mohamad from Universiti Sains Malaysia (USM) for his expertise and guidance in XRD analysis, as well as to En. Muhammad Fadhirul Izwan Abd Malik and En. Muhammad Faiz Bahrol Anuar, also from USM, for their technical assistance with FESEM-EDX analysis.

I am forever indebted to my beloved parents, and Roslan Bin Ani, for their endless love, prayers, and sacrifices, and to my dear siblings for their unwavering support and motivation during every stage of this journey.

To all who have contributed directly or indirectly to the success of this research, I would like to extend my sincere gratitude. This achievement is as much yours as it is mine.

This research was financially supported by the Ministry of Higher Education (MOHE) through the Fundamental Research Grant Scheme (FRGS/1/2023/STG05/UiTM/03/3). One of my publication also has funded by Institute of Postgraduate UiTM (IPSis UiTM) through Journal Support Fund.

# TABLE OF CONTENTS


| | | Page |
|---|---|---|
| **CONFIRMATION BY PANEL OF EXAMINERS** | | **ii** |
| **AUTHOR'S DECLARATION** | | **iii** |
| **ABSTRACT** | | **iv** |
| **ACKNOWLEDGEMENT** | | **v** |
| **TABLE OF CONTENTS** | | **vi** |
| **LIST OF TABLES** | | **ix** |
| **LIST OF FIGURES** | | **x** |
| **LIST OF SYMBOLS** | | **xiii** |
| **LIST OF ABBREVIATIONS** | | **xiv** |
| **LIST OF NOMENCLATURE** | | **xvi** |
| **CHAPTER 1 INTRODUCTION** | | **1** |
| 1.1 | Research Background | 1 |
| 1.2 | Problem Statement | 3 |
| 1.3 | Research Objective | 4 |
| 1.4 | Research Question | 4 |
| 1.5 | Scope of the Study | 4 |
| 1.6 | Limitations of the Study | 5 |
| 1.7 | Significance of the Study | 6 |
| **CHAPTER 2 LITERATURE REVIEW** | | **8** |
| 2.1 | Introduction | 8 |
| 2.2 | Radiation Exposure and Risk in Various Sectors | 8 |
| | 2.2.1 Medical Sector | 8 |
| | 2.2.2 Industrial and Environmental Field | 9 |
| 2.3 | Radiation Shielding Characteristics | 10 |
| | 2.3.1 Interaction of Photon Rays with Matter | 10 |

2.3.2 Attenuation and Performance of Shielding Materials 12
2.4 Lead as Conventional Shielding Material 15
2.5 Metal-Polymer Composite in Radiation Shielding Application 17
2.6 Introduction of Tin as a Filler of PDMS Matrix for Shielding Application 19
2.7 Factors Affecting Shielding Efficiency 21
2.8 Fabrication of a Composite using the Layering Technique 22
2.9 Radiation Shielding Against High-Energy Emission 24
2.10 Previous Study on Tin and PDMS as Radiation Shielding Application 25

**CHAPTER 3 RESEARCH METHODOLOGY 31**
3.1 Introduction 31
3.2 Stage I: Mixing and Curing Process for Double Layer Composite 31
3.2.1 Raw Material 31
3.2.2 Mixing and Curing of the Composite by the Layering Technique 33
3.2.3 Calculation of Effective Density 35
3.3 Stage II: Sample Characterisation 36
3.3.1 Field Emission Scanning Electron Microscopy / Energy Dispersive X-ray Spectroscopy 37
3.3.2 Fourier Transform Infrared Spectroscopy 37
3.3.3 X-Ray Diffraction 38
3.4 Stage III: Radiation Characterisation 39
3.5 Radiation Parameters Calculation 42

**CHAPTER 4 RESULTS AND DISCUSSIONS 43**
4.1 Introduction 43
4.2 Fabricated Sample 43
4.3 Effective Density 46
4.4 Morphology and Structural Analysis under Field Emission Scanning Electron Microscopy - Elemental Analysis with Energy Dispersive X-ray Spectroscopy 50
4.4.1 Field Emission Scanning Electron Microscopy under 100x magnification and 500x magnification 50
4.4.2 Elemental Analysis with Energy Dispersive X-ray Spectroscopy (EDX) Analysis 64

4.5 Verification of Components Through Fourier Transform Infrared Spectroscopy Analysis 69
4.5.1 FTIR Analysis of PS Series 71
4.5.2 FTIR Analysis of AS Series 72
4.5.3 FTIR Analysis of TM Series 74
4.6 Phase Identification Through X-ray Diffraction Analysis 75
4.6.1 XRD Analysis of PS Series 77
4.6.2 XRD Analysis of AS Series 78
4.6.3 XRD Analysis of TM Series 80
4.7 Radiation Attenuation Through Radiation Characterisation 82
4.7.1 Linear Attenuation Coefficient 82
4.7.2 Mass Attenuation Coefficient 88
4.7.3 Half Value Layer 94
4.7.4 Tenth Value Layer 100
4.7.5 Radiation Protection Efficiency 107
4.8 Radiation Properties for the Best Optimised Samples 114
4.8.1 Comparison of Radiation Shielding Performance with Previous Findings 118
4.8.2 Lead Equivalent of Optimised Sample 124

**CHAPTER 5 CONCLUSIONS 128**
5.1 Conclusion 128
5.2 Recommendation for Future Work 129

**REFERENCES 130**

**AUTHOR'S PROFILE 146**

# LIST OF TABLES


| Tables | Title | Page |
|---|---|---|
| Table 2.1 | Summary of Radiation Dose Comparisons | 9 |
| Table 2.2 | Characteristics of Lead | 15 |
| Table 2.3 | The Properties of Tin | 19 |
| Table 2.4 | Findings from Previous Studies | 27 |
| Table 3.1 | Raw Materials Parameters | 31 |
| Table 3.2 | Composition Ratio of Composite Fabrication | 33 |
| Table 4.1 | Calculated Density for Multilayered Tin-PDMS Composite. | 45 |
| Table 4.2 | Summary of Radiation Characteristics of PDMS, Conventional Lead, and Fabricated Samples | 47 |
| Table 4.3 | EDX Weight Percentage | 63 |
| Table 4.4 | EDX Atomic Percentage | 65 |
| Table 4.5 | LAC Values at Different Gamma Energies for Different Irradiation Surfaces | 81 |
| Table 4.6 | MAC Values at Different Gamma Energies for Different Irradiation Surfaces. | 87 |
| Table 4.7 | HVL Values at Different Gamma Energies for Different Irradiation Surfaces. | 92 |
| Table 4.8 | TVL Values at Different Gamma Energies for Different Irradiation Surfaces | 98 |
| Table 4.9 | RPE Values at Different Gamma Energies for Different Irradiation Surfaces. | 105 |
| Table 4.10 | Radiation Properties of The Optimised Samples at Low Energy (88.0 keV), Moderate Energy (356.0 keV), And High Energy (834.8 keV) | 113 |
| Table 4.11 | Comparison with The Previous Study That Used Similar Sn and PDMS | 116 |
| Table 4.12 | Lead Equivalent Thickness of Optimised Metal Filler Composite | 120 |

# LIST OF FIGURES


| Figures | Title | Page |
|---|---|---|
| Figure 1.1 | PPE in Medical Applications | 2 |
| Figure 2.1 | Chemical Structure of PDMS | 19 |
| Figure 3.1 | Flowchart of Research Methodology | 32 |
| Figure 3.2 | Raw Materials Used to Fabricate Tin-Pdms Composites: (a) Sylgard 184 Silicone Elastomer-Based Pdms; (b) Pure Tin Powder, and (c) Tin Alloy Powder | 32 |
| Figure 3.3 | Instruments Used to Calculate The Physical Properties and Dimensions of Composites: (a) Electronic Vernier Caliper, (c) Weighing Balance | 36 |
| Figure 3.4 | Fesem/Edx Instrumentation and Procedure: (a) Fesem Model and (b) Gold-Coated and Copper Tape Coiled for Fesem Analysis | 37 |
| Figure 3.5 | Fourier Transform Infrared (FTIR) Spectroscopy, Brand Perkinelmer, Model Spectrum 100 Series | 38 |
| Figure 3.6 | Bruker D8 Advance Diffractometer | 39 |
| Figure 3.7 | A Gamma-Ray Spectrometer Used for Radiation Characterisation | 40 |
| Figure 3.8 | Illustration of The Gamma Irradiation Characterisation: (a) PDMS Irradiation Surface and (b) Mixture Irradiation Surface (Tin/Alloy) | 41 |
| Figure 4.1 | Control Samples: (a) PDMS, (b) Tin Plate, and (c) Lead Plate | 44 |
| Figure 4.2 | PS Series: a) Schematic Diagram, and b) Six (6) Fabricated Samples | 45 |
| Figure 4.3 | AS Series: a) Schematic Diagram, and b) Six (6) Fabricated Samples | 45 |
| Figure 4.4 | TM Series: a) Schematic Diagram, and b) Six (6) Fabricated Samples | 46 |
| Figure 4.5 | Effective and Theoretical Density of The Composites | 48 |

| | | |
|---|---|---|
| Figure 4.6 | FESEM Images of Control PDMS at 100x Magnification and 500x Magnification | 51 |
| Figure 4.7 | FESEM Images of The PS Series at 100x Magnification and 500x Magnification of PS1, PS2, PS3, PS4, PS5, and PS6 | 54 |
| Figure 4.8 | FESEM Images of The AS Series at 100x Magnification and 500x Magnification of AS1, AS2, AS3, AS4, AS5, and AS6 | 58 |
| Figure 4.9 | FESEM Images of The TM Series at 100x Magnification and 500x Magnification of TM1, TM2, TM3, TM4, TM5, and TM | 63 |
| Figure 4.10 | FTIR Spectrum of The Control Samples and 40% Metal Filler from Each Series of Samples | 70 |
| Figure 4.11 | Overview of FTIR Results for The PS Series | 71 |
| Figure 4.12 | Overview of FTIR Results for The AS Series | 73 |
| Figure 4.13 | Overview of FTIR Results for The TM Series | 75 |
| Figure 4.14 | XRD Pattern of Control Samples | 76 |
| Figure 4.15 | XRD Patterns of Control Samples and Composite Samples Containing 50% and 60% Metal Fillers for PS Series | 78 |
| Figure 4.16 | XRD Patterns of Control Samples and Composite Samples Containing 50% and 60% Metal Fillers for AS Series | 79 |
| Figure 4.17 | XRD Patterns of Control Samples and Composite Samples Containing 50% and 60% Metal Fillers for TM Series | 81 |
| Figure 4.18 | LAC of Fabricated Composite at 88.0 keV | 85 |
| Figure 4.19 | LAC of Fabricated Composite at 122.1 keV | 86 |
| Figure 4.20 | LAC of Fabricated Composite at 356.0 keV | 86 |
| Figure 4.21 | LAC of Fabricated Composite at 661.7 keV | 87 |
| Figure 4.22 | LAC of Fabricated Composite at 834 keV | 87 |
| Figure 4.23 | MAC of Fabricated Composite at 88.0 keV | 91 |
| Figure 4.24 | MAC of Fabricated Composite at 122.1 keV | 91 |
| Figure 4.25 | MAC of Fabricated Composite at 356.0 keV | 92 |
| Figure 4.26 | MAC of Fabricated Composite at 661.7 keV | 92 |
| Figure 4.27 | MAC of Fabricated Composite at 834.8 keV | 93 |
| Figure 4.28 | HVL of Fabricated Composite at 88.0 keV | 96 |
| Figure 4.29 | HVL of Fabricated Composite at 122.1 keV | 97 |
| Figure 4.30 | HVL of Fabricated Composite at 356.0 keV | 97 |
| Figure 4.31 | HVL of Fabricated Composite at 661.7 keV | 98 |

| | | |
|---|---|---|
| Figure 4.32 | HVL of Fabricated Composite at 834.8 keV | 98 |
| Figure 4.33 | TVL of Fabricated Composite at 88.0 keV | 104 |
| Figure 4.34 | TVL of Fabricated Composite at 122.1 keV | 105 |
| Figure 4.35 | TVL of Fabricated Composite at 356.0 keV | 105 |
| Figure 4.36 | TVL of Fabricated Composite at 661.7 keV | 106 |
| Figure 4.37 | TVL of Fabricated Composite at 834.8 keV | 106 |
| Figure 4.38 | RPE of Fabricated Composite at 88.0 keV | 111 |
| Figure 4.39 | RPE of Fabricated Composite at 122.1 keV | 111 |
| Figure 4.40 | RPE of Fabricated Composite at 356.0 keV | 112 |
| Figure 4.41 | RPE of Fabricated Composite at 661.7 keV | 112 |
| Figure 4.42 | RPE of Fabricated Composite at 834.8 keV | 113 |
| Figure 4.43 | Variation of tPb and RPE of 50% and 60% Samples at 356.0 keV | 125 |
| Figure 4.44 | Variation of tPb And RPE of 50% to 60% Samples at 661.7 keV | 126 |
| Figure 4.45 | Variation of tPb And RPE of 50 to 60% Samples at 834.8 keV | 127 |

# LIST OF SYMBOLS

**Symbols**

| | |
|---|---|
| $\mu$ | Linear Attenuation Coefficient of The Composite |
| A | Cross-Sectional Area of Composite |
| $I_0$ | Initial Intensity of The Radiation Source, Measured Without Sample |
| I | Transmitted Intensity of Radiation, Passing Through The Sample |
| N | Number of Atoms Per Unit Volume |
| $\rho$ | Total Density of Composite |
| $\rho_1$ | Density of The First Layer Composite |
| $\rho_2$ | Density of The Second Layer Composite |
| $\rho_{theoretical}$ | Theoretical Effective Density Value of A Composite |
| $\rho_{calculated}$ | Calculated Effective Density Value of A Composite |
| $t_1$ | Thickness of The First Layer Composite |
| $t_2$ | Thickness of The Second Layer Composite |

# LIST OF ABBREVIATIONS

**Abbreviations**

| | |
|---|---|
| AS Series | Tin Alloy – PDMS Composite Series |
| $Bi_2W_6O$ | Bismuth Tungsten Oxides |
| $Bi_2O_3$ | Bismuth Oxide |
| $CaCO_3$ | Calcium Carbonate |
| CdO | Cadmium Oxide |
| $CeO_2$ | Cerium Oxide |
| CuSn | Copper-Tin Alloy |
| EDX | Energy-Dispersive X-Ray Spectroscopy |
| FESEM | Field Emission Scanning Electron Microscopy |
| FTIR | Fourier Transform Infrared Spectroscopy |
| HVL | Half-Value Layer |
| IAEA | International Atomic Energy Agency |
| keV | Kilo Electron Volt |
| LAC | Linear Attenuation Coefficient |
| MAC | Mass Attenuation Coefficient |
| MeV | Mega Electron Volt |
| NaI (TI) | Sodium Iodide Activated with A Thallium Detector |
| PbO | Lead Oxide |
| PDMS | Polydimethylsiloxane |

| | |
|---|---|
| PPE | Personal Protective Equipment |
| PS Series | Pure Tin – PDMS Composite Series |
| PVC | Polyvinyl Chloride |
| RPE | Radiation Protection Efficiency |
| $SnO_2$ | Tin Oxide |
| TM Series | Tin Mixture – PDMS Composite Series |
| TVL | Tenth-Value Layer |
| TPV | Thermoplastic Vulcanizate |
| $WO_3$ | Tungsten Oxide |
| XRD | X-Ray Diffraction |
| ZnO | Zinc Oxide |

# LIST OF NOMENCLATURE

**Nomenclature**

| | |
|---|---|
| Alloy Irradiation Surface (AS series) | The Tin Alloy PDMS Layer is Placed Facing The Irradiation Probe |
| Control Lead | Standard Lead Plate As A Reference Material for The Theoretical Value of Shielding |
| Control PDMS | 100% PDMS Composite As A Reference Material |
| Control Tin | Standard Tin Plate As A Reference Material |
| PDMS Irradiation Surface (PS series) | The PDMS Layer is Placed Facing The Irradiation Probe |
| Tin Irradiation Surface (PS series) | The Tin PDMS Layer is Placed Facing The Irradiation Probe |

# CHAPTER 1
# INTRODUCTION

## 1.1 Research Background

Medical professionals and radiation workers are the people who are at risk from ionising radiation, especially when the ionising radiation is frequently used to treat and diagnose patients. Ionising radiation is an energy that is emitted by atoms and travels as particles (beta or alpha particles) or electromagnetic waves (gamma or X-rays) (Sobczak & Żyła, 2024). Radioactivity is the term for the spontaneous breakdown of atoms, and the excess energy released is ionising radiation (Alotaibi et al., 2021). About 23 million people worldwide are exposed to ionising radiation during work, as recorded by the International Atomic Energy Agency (IAEA). Out of the 308,279 recognised workers, about 19,748 died of cancer, 684 of leukaemia, and 5802 workers died of lung cancer (Cardis et al., 2005; IAEA Safety Standards for Protecting People and the Environment General Safety Guide No. GSG-7 Occupational Radiation Protection Jointly). Chronic exposure, even at low levels, poses significant risks to children and pregnant women, as it can lead to developmental disorders and other long-term health issues (Calderón - Gerstein & Torres - Samaniego, 2021; Cardis et al., 2005).

Another study reported that female technicians had a markedly elevated risk of developing breast cancer after being exposed to low-dose radiation regularly for several years (Cardis et al., 2005). This harmful exposure proves the need for personal protective equipment (PPE) to safeguard both medical workers and patients, as shown in Figure 1.1 (Occupational Safety and Health Administration U.S. Department of Labor, 2005). Figure 1.1 shows the PPE of lead aprons and thyroid collar. The PPE made up of lead composite was introduced in the early $20^{th}$ century (McGinley et al., 1995). The PPE mainly protects the critical organs such as the heart, lungs, thyroid, and reproductive organs (Boice et al., 2020).

Lead-based materials were commonly employed as radiation barriers to block photon radiation (Al-Balushi et al., 2021). Lead has a high absorption energy due to its high atomic number of 82 and high-density of 11.34 g $cm^{-3}$ (Hubbell & Seltzer, 1995). Dense materials offer good absorption of photon radiation. It can shield employees from

radiation in various radiation-prone industries by using PPE or protective walls and windows (Anderson et al., 2021; Chang et al., 2023).



Figure 1.1 PPE in Medical Applications

Lead aprons, for instance, are used as a precautionary measure to shield employees and patients from unintentional X-ray exposure in diagnostic radiology (Brown, 2020). However, the heavy weight and high toxicity of lead contribute to its disadvantages (Gurumurthi & Rajasekar, 2025). The hazards posed by the PPE not only to the patient, but to the operator in the medical sector have been studied and discovered (Boice et al., 2020).

Researchers are studying different materials and fabrication methods to replace lead-based materials, which have high absorption for high-energy photons and a low potential for scattered radiation, including secondary scattered radiation (Safari et al., 2024). The increasing prevalence of applications requiring effective radiation shielding, from medical imaging to nuclear facilities, necessitates the development of advanced materials that can provide efficient protection against various types of radiation (McGinley et al., 1995).

Shielding materials often face limitations in performance and flexibility. Polydimethylsiloxane (PDMS), a silicon-based polymer, is known for its excellent flexibility, chemical stability, biocompatibility, and ease of processing, but lacks adequate radiation absorption properties when used alone (Resende et al., 2024). Conversely, tin is a metal with a high atomic number and has demonstrated significant potential in radiation shielding due to its ability to attenuate X-rays and gamma rays effectively (Safari et al., 2024).

The challenge lies in fabricating a composite material that combines the desirable mechanical and chemical properties of PDMS with tin's radiation absorption

capabilities. The layering technique has emerged as a promising method for fabricating such a composite, as it allows for precise control over the distribution and integration of tin within the PDMS matrix (Zhang et al., 2017). There is a notable gap in research concerning the effective application of this technique to create a double-layered tin-PDMS composite specifically for radiation absorption. Key issues include achieving a uniform distribution of tin particles, ensuring strong adhesion between layers, and verifying the composite's performance in radiation shielding applications.

## 1.2 Problem Statement

Lead is a good radiation shielding material. Though, lead poses serious health and environmental hazards due to its toxicity and tendency to bioaccumulate. Even with strict safety protocols, medical personnel and industrial workers can still experience radiation-related health problems. Long-term low-dose exposure in radiologic technicians and interventional cardiologists, for example, has been associated with an increased risk of cataracts, cancer, and brain tumours (Vano et al., 2013).

Beyond radiation effects, lead itself is a potent neurotoxin (Boice et al., 2020). Chronic exposure, even at low levels, can cause cognitive impairment, cardiovascular disease, and renal dysfunction. It is particularly harmful to children and pregnant women, leading to developmental disorders and other long-term complications (Calderón - Gerstein & Torres - Samaniego, 2021; Cardis et al., 2005; Jamal AbuAlRoos et al., 2020). Exposure pathways include inhalation of lead dust and ingestion of contaminated materials, making both the use and disposal of lead-based PPE hazardous.

From a structural standpoint, lead's softness and malleability make it prone to deformation under stress, reducing its protective capability over time (Boice et al., 2020). Frequent bending, folding, and handling can lead to cracks and gaps in the material, increasing radiation leakage risk, which may be close to the critical organ site (Daniel & Xaviera, 2018). To maintain optimal protection, lead-based PPE requires regular inspection and maintenance, adding to operational costs. Environmental risks are also significant as they can lead to degradation when exposed to chemicals or moisture, subsequently releasing harmful particles into the surrounding environment. This degradation not only compromises user safety but also contributes to environmental contamination.

Given these health, safety, and environmental concerns, there is a critical need for alternative radiation shielding materials that can provide comparable or superior protection without the drawbacks of lead. Such materials should be non-toxic, durable, and environmentally sustainable, ensuring safety for both users and the environment while reducing maintenance demands and overall lifecycle costs.

## 1.3 Research Objective

The main objectives of this study are outlined as follows:

i. To fabricate a tin-PDMS composite using the layering technique.
ii. To analyse the structural and morphological properties of tin-PDMS composite.
iii. To evaluate the radiation absorption efficiency of tin-PDMS composite.

## 1.4 Research Question

Based on the scope of this study, the research questions are formulated as follows:

i) How can the tin-PDMS composite be effectively fabricated using the layering technique?
ii) How does the distribution of tin filler affect the structural and morphological properties of tin-PDMS composite?
iii) What is the efficiency of tin-PDMS composite against ionising radiation?

## 1.5 Scope of the Study

This research focuses on the fabrication and characterisation of tin-PDMS composites using a layering technique for radiation absorption applications. The study encompasses material preparation, physical properties, elemental analysis, morphological and structural analysis, radiation characterisation, and measurement of attenuation properties. Composite samples with varying tin-PDMS ratios were prepared and studied using , and Fourier Transform Infrared Spectroscopy Analysis (FTIR) for elemental analysis, Field Emission Scanning Electron Microscopy - Energy Dispersive X-ray Spectroscopy (FESEM - EDX), and X-Ray Diffraction (XRD) for surface morphology and structural analysis, and lastly, radiation characterisation and measurement of attenuation properties were assessed over a broad gamma-ray energy

range, covering low to high energy photons, to simulate conditions relevant to medical, nuclear, and aerospace environments. Key attenuation parameters, Linear Attenuation Coefficient (LAC), Mass Attenuation Coefficient (MAC), Half Value Layer (HVL), Tenth Value Layer (TVL), and Radiation Protection Efficiency (RPE), were measured and compared across different metal – filler composite, irradiation orientations, and benchmarked against conventional lead-based shielding materials.

## 1.6 Limitations of the Study

The maximum metal filler concentration that could be homogeneously incorporated into the PDMS matrix was limited to 60%. Beyond this point, the PDMS was unable to adequately embed or wet the metal particles, resulting in a "dry" mixture that lacked proper cohesion between the filler and polymer. This may be due to the viscosity of the PDMS of 3160 cP. 70% of the metal powder could not mix well with 30% PDMS. Restriction reduced the ability to investigate higher filler compositions, which could potentially enhance radiation attenuation. Consequently, the study's comparison of filler loading effects is limited to compositions where uniform embedding within PDMS was achievable.

Methodological constraints were noted in the layering process. Previous studies have fabricated layered composites by oven-heating each layer sequentially (Gilys et al., 2022). Repeated heating cycles can cause thermal degradation of the PDMS matrix, leading to reduced mechanical strength, increased oxygen content, and diminished shielding performance. Conversely, if the composite were cured in a glass jar of silica gel, the composite would shrink as well. Therefore, the oven is not the only cause of polymer shrinkage. Additionally, inadequate bonding between the PDMS matrix and tin particles may result in delamination or incomplete integration, reducing both structural integrity and attenuation efficiency (Farahani et al., 2020).

Lastly, the radiation energy during testing was not fully stable throughout all measurements. Variations in radiation intensity were more apparent at lower energy levels, leading to occasional unreadable or fluctuating detector responses, especially in control lead samples. These inconsistencies were minimised through calibration using cobalt-60 (Co-60), that represent two (2) peaks, which enabled correction and normalisation of energy levels across measurements. However, slight residual fluctuations may still contribute to small uncertainties in the recorded data, particularly

at lower photon energies.

Despite these challenges, this study provides a detailed comparison of shielding effectiveness across multiple composite configurations and orientations, identifying promising tin–PDMS formulations with attenuation characteristics approaching those of lead while offering significant reductions in weight and toxicity. These findings support the potential for developing advanced, non-toxic shielding materials optimised for diverse radiation environments.

## 1.7 Significance of the Study

The significance of this study lies in its potential to contribute to the development of innovative, safer, and more efficient alternative materials for radiation absorption applications with a multilayering technique. Lead has long been the material of choice for radiation shielding due to its high density and strong attenuation capability (McGinley et al., 1995). However, its inherent toxicity, environmental hazards, and handling difficulties due to weight present major drawbacks (Boice et al., 2020). These limitations have driven the search for lead-free shielding materials that are both effective and environmentally sustainable.

The concept of layering metal-polymer composites, first investigated in the 1950 (Ding et al., 2021), offers a promising path toward achieving superior radiation protection performance. In particular, the exploration of tin PDMS composites represent a significant step in this direction. PDMS is a lightweight, flexible, and non-toxic polymer, while tin provides the high-density characteristics required for radiation attenuation (Sharma & Bose, 2021). Although this study does not directly address mechanical or toxicity-related properties, the combination of these materials is expected to yield composites with improved safety, comfort, and handling characteristics, in addition to high shielding efficiency. By optimising the distribution and composition of metal fillers across multiple layers, the proposed layering technique enables fine control of density gradients and absorption profiles, thereby enhancing radiation attenuation while minimising total material thickness.

This multilayer fabrication approach also provides distinct advantages in material design, allowing precise control over layer thickness, density, and composition. Such control facilitates the optimisation of radiation shielding performance while maintaining lightweight and ergonomic properties. The layered structure can achieve

comparable or superior shielding effectiveness to conventional materials with reduced mass, making it highly suitable for extended use in medical, industrial, and aerospace applications. For example, in medical settings, lighter and more flexible shielding materials could enhance the comfort and safety of both patients and healthcare personnel during diagnostic imaging procedures or radiation therapy. Similarly, in nuclear energy sectors, these materials could reduce the physical strain associated with heavy personal protective equipment. In aerospace contexts, they may serve as an important step toward protecting astronauts from cosmic radiation during long-duration space missions, contingent on further validation of mechanical strength and biocompatibility (Anderson et al., 2021; Farahani et al., 2020; Safari et al., 2024).

This study also aligns with Malaysia's national commitment to environmental sustainability and green technology development, as outlined in the *Garis Panduan Perolehan Hijau Kerajaan 2* (Tenaga et al., 2018). These guidelines emphasise the importance of adopting materials and processes that minimise environmental impact, particularly through the reduction or elimination of hazardous substances such as lead. The development of lead-free radiation shielding materials, such as tin–PDMS multilayer composites, directly supports these objectives by offering a safer and more sustainable alternative to conventional lead-based shields (Safari et al., 2024). By reducing reliance on toxic and non-recyclable materials, this research contributes to advancing eco-friendly innovation within Malaysia's materials engineering and manufacturing sectors, promoting safer working environments and supporting the nation's broader green procurement and sustainability goals.

Overall, this study contributes to the broader goals of materials science and public health by addressing the limitations of conventional shielding materials. It provides a scientific foundation for developing non-toxic, effective, and customisable alternatives to lead-based shields, fostering advancements that benefit medical imaging, industrial safety, and space exploration technologies alike.

# CHAPTER 2
# LITERATURE REVIEW

## 2.1 Introduction

Radiation can be divided into two (2) main classifications based on its wavelength and energy of emission, which are ionising radiation and non-ionising radiation (Sobczak & Żyła, 2024). Ionising radiation is a type of radiation that can alter the electrons of matter as it passes through, while non-ionising radiation cannot do so due to its longer wavelength and low energy penetration (Nanda Karmaker et al., 2021a). Radioactive sources have been applied in various medical fields for the diagnosis and treatment of diseases (Jayakumar et al., 2023). When handling high-energy rays such as Gamma rays, the individual must wear suitable PPE to protect themselves from the risk of exposure to ionising radiation. PPE functions to absorb and reflect high-energy rays and protect important organs in humans, such as the kidneys and the heart, from ionising radiation (Kim, 2023). Standard radiation protection PPE usually can be found in 0.5 mmPb thickness which weigh around three (3) to four (4) kg (Kato et al., 2021).

## 2.2 Radiation Exposure and Risk in Various Sectors

Radiation emission exposure is a critical concern across numerous fields, including medical, industrial, aerospace, and environmental sectors (Behzadmehr et al., 2021; Graeff et al., 2023; Nanda Karmaker et al., 2021). Understanding the sources, types, and levels of radiation exposure in these fields is essential for implementing effective protection measures.

### 2.2.1 Medical Sector

In the medical field, radiation exposure is prevalent during diagnostic imaging and therapeutic procedures. For example, a typical chest X-ray exposes a patient to about 0.1 mSv of radiation, which is equivalent to about ten (10) days of natural background radiation exposure (Safari et al., 2024). More intensive procedures, such as a computer tomography (CT) scan of the abdomen and pelvis, can expose patients to

approximately 7.7 mSv, comparable to about 2.6 years of natural background radiation (Brown, 2020; IAEA Safety Standards for Protecting People and the Environment General Safety Guide No. GSG-7 Occupational Radiation Protection Jointly). These exposures, while necessary for accurate diagnosis and treatment, underscore the importance of effective radiation shielding to protect both patients and healthcare workers from unintended exposure. Table 2.1 shows the summary of radiation dose comparisons in the medical field (Roslan, Mukhtar, Mahmood, Abdul Wahab, et al., 2026).

Table 2.1
Summary of Radiation Dose Comparisons

| **Procedure** | **Approximate Effective Dose (mSv)** | **Comparable to Natural Background Radiation** |
|---|---|---|
| Chest X-ray | 0.100 | 10 days |
| Abdominal CT scan | 7.700 | 2.6 years |
| Dental X-ray | 0.005 | 1 day |
| Mammogram | 0.400 | 7 weeks |
| Head CT scan | 1.500 | 6 months |
| PET/CT scan | 22.700 | 7.6 years |

### 2.2.2 Industrial and Environmental Field

In industrial settings, radiation is used in various applications, such as radiography testing for material integrity, nuclear power generation, and industrial radiography (N. M. A. Mukhtar et al., 2024). Workers in these fields can be exposed to varying levels of radiation, depending on the specific tasks and duration of exposure (Behzadmehr et al., 2021). For instance, workers in nuclear power plants might be exposed to annual doses ranging from 1 to 10 mSv, which necessitates stringent safety measures and effective shielding to minimise health risks (Brown, 2020; N. M. A. Mukhtar et al., 2024).

Environmental radiation exposure is another significant concern, especially in areas affected by nuclear accidents or those with naturally high background radiation levels. For example, following the Fukushima Daiichi nuclear disaster, efforts to monitor and mitigate radiation exposure became a top priority to protect public health and safety (IAEA Safety Standards for Protecting People and the Environment General Safety Guide No. GSG-7 Occupational Radiation Protection Jointly Sponsored By,

n.d.). Typically, background radiation levels range from 1 to 3 mSv per year globally. These levels can be significantly higher in contaminated areas, necessitating ongoing remediation and monitoring efforts.

## 2.3 Radiation Shielding Characteristics

Ionising radiation is a type of electromagnetic radiation that has higher energy than non-ionising radiation. It can eject electrons from atoms, producing positively charged ionised atoms and negatively charged free electrons. Any kind of particle or photon, including beta particles, neutrons, gamma rays (γ), and X-rays, can be considered ionising radiation (Cardis et al., 2005; Farahani et al., 2020; Sobczak & Żyła, 2024). Radiation and matter interact in various ways, including the photoelectric effect, Compton scattering, and pair production (Nanda Karmaker et al., 2021c).

### 2.3.1 Interaction of Photon Rays with Matter

The photoelectric effect occurs when the energy of an incoming photon exceeds the binding energy of the core electron. During the process, a core electron is ejected from the atom of the substance exposed to radiation (Yuan et al., 2024). The core electron will fully absorb the incoming photon. As a result, an electron is ejected, and the photon's residual energy is transformed into the kinetic energy of the ejected photoelectron (Ragnvaldsen et al., 2022). When it reverts to its natural state, characteristic X-rays and Auger electrons will be released (Yuan et al., 2024). Energy conservation for the photoelectric effect is between 10 and 100 keV, and it gets stronger as the shield's atomic number rises, providing the cross-section of the photon-photoelectric effect interaction (t) (Chang et al., 2023; Resende et al., 2024).

For tin–PDMS composites, the high atomic number of tin (Z = 50) significantly enhances the probability of photoelectric absorption compared with the PDMS matrix, which consists primarily of low-Z elements (C, H, O, and Si). Consequently, increasing the tin filler loading increases photon absorption at diagnostic X-ray energies, leading to higher linear and mass attenuation coefficients and lower HVL values. In the layered composites developed in this study, the tin-rich irradiation surface further promotes photoelectric interactions by ensuring that incident photons encounter the high-Z tin

particles before penetrating the polymer matrix, thereby improving attenuation efficiency.

Compton scattering primarily occurs between 100 keV and 10 MeV, and the cross-section of interaction (σc) is directly proportional to the atomic number (Z) of the atom (Hubbell & Seltzer, 1995). It is an inelastic scattering in which the incoming photon interacts with an electron and gets deficient with reduced energy (or higher wavelength) after imparting some of its energy to the electron of the irradiated materials. An electron will also get ejected from its orbital position during this interaction (Chang et al., 2023).

Within the investigated energy range of this study, Compton scattering becomes increasingly important at medium and higher photon energies (356.0 – 834.8 keV). The incorporation of tin particles into the PDMS matrix increases the effective electron density of the composite, thereby enhancing Compton interactions. Furthermore, the double-layered structure influences the interaction sequence, where photons transmitted through the first layer undergo additional scattering and attenuation in the second layer. This multiple-interaction pathway contributes to the improved shielding performance observed for the layered tin–PDMS composites, particularly when the alloy-rich surface faces the radiation source.

Pair production occurs when an electron's rest mass is equal to twice the energy of the incoming photon. Pair creation happens when the energy of the incoming photons is more than 1.02 MeV, since an electron's rest mass is 0.511 MeV (Yuan et al., 2024). As the name implies, pair production occurs when an incoming photon interacts with the nucleus, resulting in the ejection of a pair of particles, namely an electron and its antiparticle (positron). The excess energy will be transformed into the electron's kinetic energy. The Coulomb interaction will slow down the ejected electron and positron. By radiation loss with energy much lower than the incident photon, they simultaneously release Bremsstrahlung X-ray photons (Alanazi et al., 2024a; S. Chen et al., 2019). The positron undergoes annihilation to reunite with its antiparticle, the electron, after ionising most of its energy (António et al., 2020). This produces two (2) gamma photons with an energy of at least 0.511 MeV.

Although pair production is theoretically favoured in high-Z materials such as tin, its contribution in this study is expected to be negligible because the highest investigated photon energy (834.8 keV) is below the pair production threshold of 1.022 MeV. Therefore, the radiation attenuation behaviour of the developed tin–PDMS

composites is governed primarily by the photoelectric effect at low photon energies and Compton scattering at intermediate energies.

### 2.3.2 Attenuation and Performance of Shielding Materials

The effectiveness of radiation shielding materials is determined by several parameters that describe how well the material can attenuate ionising radiation. Key metrics include the density (ρ), LAC, MAC, HVL, TVL, and RPE. These parameters help in comparing different materials and in designing effective radiation shields.

#### *2.3.2.1 Density*

In general, materials with higher density exhibit superior shielding performance, since a greater number of atoms per unit volume are available to interact with and attenuate radiation. Density is typically expressed in unit (g $cm^{-3}$), as given in Equation (2.1). For multilayer composites, density can be evaluated using Equations (2.2) and (2.3), while the variation between measured and theoretical values can be quantified as a percentage difference, as shown in Equation (2.4), where A refers to the cross-sectional area of the composite and is the total effective density of the double-layer composite. $\rho_1$ refer to the density of the first layer composite, $t_1$ is the thickness of the first-layer composite, $\rho_2$ is the density of the second-layer composite, $t_2$ refer to the thickness of the second-layer composite, $\rho_{calculated}$ is the effective density of the fabricated composite, and $\rho_{lheoretical}$ refer to the theoretical density of the composite.

$$\rho = \text{mass} / \text{volume} \tag{2.1}$$

$$\rho = \text{total mass} / A(t_1 + t_2) \tag{2.2}$$

$$\rho = (\rho_1 t_1 + \rho_2 t_2) / (t_1 + t_2) \tag{2.3}$$

$$|(\rho_{\text{calculated}} - \rho_{\text{theoretical}}) / \rho_{\text{theoretical}}| \times 100\% \tag{2.4}$$

Maintaining a low percentage difference is important, as it reflects uniformity and consistency in the composite structure. A small variation indicates a well-controlled fabrication process, implying proper dispersion of tin particles within the matrix. Therefore, the calculated density should closely approximate the theoretical density to

ensure optimal shielding performance and structural homogeneity of the composite (S. Chen et al., 2019). Thus, the calculated density should be as close to its theoretical density as feasible for optimal performance and to ensure the homogeneity of the composites.

#### *2.3.2.2 Linear Attenuation Coefficient*

The LAC is a key factor that indicates how well a material can reduce the intensity of gamma photons per unit thickness, with SI unit $cm^{-1}$. The LAC value of composite calculated by using Equations (2.5) and (2.6), where $I_0$ refers to the initial photon intensity, I is the transmitted photon intensity, x refers to the thickness of the composite, and μ is the linear attenuation coefficient of the composite.

$$I = I_0 e^{-\mu x} \tag{2.5}$$

$$\mu = (1/x) \ln (I_0/I) \tag{2.6}$$

Previous studies on metal–polymer composites for radiation shielding have shown that lead–epoxy and tin - PDMS composites exhibit similar LAC values when high-density metals are oriented toward the radiation source. These results are consistent with other research demonstrating that primary photon attenuation is significantly improved in layered structures when denser, high-atomic-number materials are positioned at the front, directly facing the incident radiation (Almuqrin, Sayyed, Khandaker, et al., 2024; Shaker & Abbas, 2024).

#### *2.3.2.3 Mass Attenuation Coefficient*

The MAC describes the capability of the material to attenuate radiation, while the attenuation coefficient is a measure of how easily radiation can pass through a material. The MAC measured in units of centimetre cube per gram ($cm^2\ g^{-1}$) describes how the intensity of radiation decreases as it passes through a material by the material's density, as shown in Equation (2.7), where μ represents the linear attenuation coefficient of the composite and ρ represents the effective density of the double-layer composite.

$$MAC = \mu / \rho \tag{2.7}$$

#### *2.3.2.4 Half Value Layer*

The HVL, measured in units of millimetre (mm) or centimetres (cm), is the thickness of a material required to reduce the intensity of radiation to half its original value. It is a critical parameter for evaluating the shielding efficiency of a material. Radiation performance, as measured by the HVL, is the most used quantitative measure to estimate how well a specific radiation can penetrate an item (Aldawood et al., 2024a). Any material or shield thickness where 50% of the incoming radiation has been attenuated is called HVL. It is sometimes referred to as beam quality and serves as a stand-in for determining the penetrability of an X-ray spectrum. HVL is widely used in clinical practice to characterise X-ray beams and assess filtration. A smaller HVL means the material is more effective in attenuating radiation. HVL readings provide useful details about the radiation's capacity to pierce materials (Al-mugren et al., 2024).

HVL is expressed by Equation (2.8) followed by Equation (2.9), where μ represents the LAC of the composite, $I_0$ refers to the initial photon intensity, and I is the transmitted photon intensity.

$$I/I_0 = e^{-\mu(HVL)} = 1/2 \tag{2.8}$$

$$HVL = \ln(2)/\mu \tag{2.9}$$

#### *2.3.2.5 Tenth Value Layer*

The TVL is an important concept in radiation shielding and dosimetry. It represents the thickness of a given material required to reduce the intensity of radiation by 90% of its original level. This measure is widely used in radiology, nuclear engineering, and health physics to design protective barriers against ionising radiation. Mathematically, radiation attenuation follows an exponential law, shown in Equation (2.10), where μ represents the LAC of the composite. This formula shows that TVL is inversely proportional to the material's LAC.

$$TVL = \ln(10)/\mu \tag{2.10}$$

Materials with high attenuation coefficients, such as lead or tungsten require much thinner layers to achieve the same radiation reduction compared to materials with

lower coefficients, such as concrete or water. From a practical standpoint, TVL is critical in shielding design for medical X-ray rooms, nuclear reactors, and radiation therapy bunkers. Using TVL data allows engineers to calculate the required thickness of shielding material to protect both workers and the public from excessive exposure. Moreover, combining TVL with the concept of HVL, which reduces intensity by half that enables a comprehensive understanding of material shielding properties.

#### *2.3.2.6 Radiation Protection Efficiency*

The RPE of the effectiveness of a shielding material in reducing radiation exposure. It is expressed as a percentage (%) as shown in Equations (2.11) and (2.12) (Libeesh et al., 2022), Where μ represents LAC of the sample at a specific gamma-ray, x is the thickness of the sample, I represent the intensity of radiation after passing through the material, and $I_0$ represents the initial intensity of radiation. Depending on the μ, composite materials' shielding capacities could be assessed using RPE.

$$\text{RPE} = (1 - e^{-\mu x}) \times 100\% \quad (2.11)$$

$$\text{RPE} = (1 - (\, I/I_0\,)) \times 100\% \quad (2.12)$$

## 2.4 Lead as Conventional Shielding Material

Lead has been a cornerstone in radiation shielding for decades due to its unique chemical properties and effectiveness in attenuating ionising radiation. This section provides an in-depth look at lead's chemical properties and its uses as PPE, advantages, disadvantages, and the pressing need to replace it due to its significant toxicity and weight. Lead is a heavy metal with an atomic number of 82, located in Group 14 of the periodic table. It has a high density of 11.34 g $cm^{-3}$, making it effective at absorbing and attenuating gamma rays and X-rays (Burns et al., 2017; Daniel & Xaviera, 2018; Kellens et al., 2022). Lead provides significant electron density, which enhances its ability to block and scatter high-energy photons. However, lead is malleable, ductile, and relatively resistant to corrosion, which contributes to its durability in various applications (Alım, 2020; Gouda et al., 2023).

In medical and industrial settings, lead is commonly used in the form of aprons, gloves, and shields to protect workers from radiation exposure (S. Chen et al., 2019).

Lead aprons, for example, are standard in radiology departments to shield patients and healthcare providers during diagnostic imaging procedures (António et al., 2020). These aprons typically contain lead sheets that are flexible enough to drape over the body, providing a barrier that significantly reduces the radiation dose (Ogul et al., 2024). The primary advantage of lead as a shielding material is its high efficacy in attenuating ionising radiation. The high atomic number and density indicate that even thin layers can provide substantial protection, making it highly effective in environments with high radiation levels. Additionally, lead is relatively inexpensive and widely available, which makes it a practical choice for radiation shielding in many industries (Al-Balushi et al., 2021; Al-mugren et al., 2024).

Despite its effectiveness, lead has several significant disadvantages that have prompted the search for alternative materials. One of the most critical issues is lead toxicity (Jamal AbuAlRoos et al., 2020a). Lead is a potent neurotoxin, and exposure can lead to severe health problems, including cognitive impairment, cardiovascular issues, and renal dysfunction. Lead exposure can occur through inhalation of lead dust or ingestion of lead-contaminated materials, making handling and disposal of lead-containing PPE and waste particularly hazardous. In addition, the significant weight of lead is another major drawback. The high density that makes lead effective as a radiation shield also makes it cumbersome and uncomfortable for use in PPE. Lead aprons and shields are heavy, which can cause fatigue and musculoskeletal strain for workers who need to wear them for extended periods. This physical burden can reduce compliance with safety protocols and potentially compromise the effectiveness of radiation protection measures (Ashraff Rosdi et al., 2018; Farahani et al., 2020). Table 2.2 summarises the characteristics of lead as a conventional shielding material.

Given the health risks and practical challenges associated with lead, there is a pressing need to develop and adopt alternative materials for radiation shielding. Researchers are exploring various high-density elements and composite materials that can offer similar superior radiation protection without the associated toxicity and weight issues. These composites not only reduce the risk of toxic exposure but also improve the comfort and usability of protective gear (Dikra et al., 2024a).

Table 2.2
Characteristics of Lead

| Aspect | Lead |
|---|---|
| Advantages | High atomic number, high density, effective in attenuating gamma rays and X-rays, relatively inexpensive |
| Disadvantages | High toxicity can cause severe health problems, including fatigue and musculoskeletal strain (Jamal AbuAlRoos et al., 2020a). |
| Health impact | Effect on neurotoxicity, cognitive impairment, renal dysfunction, cardiovascular issues, and developmental disorders |
| Environmental impact | Highly toxic, difficult to dispose of safely, and with strict handling regulations (Ashraff Rosdi et al., 2018; Farahani et al., 2020) |

## 2.5 Metal-Polymer Composite in Radiation Shielding Application

The demand for effective radiation shielding materials has grown significantly across various sectors, including medical (Z. Chen et al., 2023; Kaewpirom et al., 2022; Nikeghbal et al., 2020), nuclear, aerospace, and industrial fields. Metal-polymer composites have emerged as a promising solution, offering a unique combination of properties that make them ideal for radiation shielding applications (Z. Chen et al., 2023; El-Khatib, Alabsy, et al., 2024; Kaewpirom et al., 2022; More et al., 2021a; Nikeghbal et al., 2020).

Metal - polymer composites are engineered by embedding metal particles within a polymer matrix, creating a material that harnesses the high atomic number and density of metals along with the flexibility and processing advantages of polymers. This synergy allows for the design of materials that are not only effective in blocking harmful radiation but also lightweight (Safari et al., 2024), flexible (El-Khatib, Alabsy, et al., 2024), and safer to handle. Tin has gained particular attention as a filler due to its favourable characteristics, including a high atomic number (Vano et al., 2013), low toxicity compared to lead, and good compatibility with various polymer matrices (Almurayshid et al., 2021), (Nanda Karmaker et al., 2021). In addition to tin, other metals such as bismuth (Bi) (Gouda et al., 2023), tungsten (W) (El-Khatib, Alabsy, et al., 2024), and gadolinium (Gd) (Kaewpirom et al., 2022) are also utilised in metal-polymer composites (Aldawood et al., 2024b; More et al., 2021). These metals offer high-density alternatives to lead and contribute to the development of composites with tailored properties for specific shielding requirements. For instance, tungsten is known for its very high density and effectiveness in gamma-ray shielding, while gadolinium is

particularly useful in neutron shielding applications due to its high neutron absorption cross-section (Buonanno et al., 2019; Jamal AbuAlRoos et al., 2020a; Ramamoorthy, 2018).

Bismuth is another metal that is widely used in radiation shielding composites. It has an atomic number of 83 with a density of 9.75 g $cm^{-3}$, which makes it highly effective at attenuating radiation. Bismuth-based composites are often used in medical and nuclear applications due to their non-toxic nature compared to lead (More et al., 2021). Next, tungsten with an atomic number of (Z = 74), with a density of 19.35 g $cm^{-3}$, has one of the highest densities among metals, providing excellent shielding properties. Tungsten-polymer composites are used in high-radiation environments, such as in space applications and nuclear reactors. However, tungsten's high density also makes the composites heavier, which can be a disadvantage in some applications (Jamal AbuAlRoos et al., 2020). On the other hand, tin is a post-transition metal with an atomic number of 50 and an atomic mass of 118.71 u. It exhibits a tetragonal crystal structure and a relatively high density of 7.31 g $cm^{-3}$. Although lower than that of lead, it is sufficient for effective radiation attenuation. Tin's high atomic number contributes to its ability to interact with and absorb high-energy photons, making it a suitable material for radiation shielding (Gouda et al., 2023).

Figure 2.1 shows that PDMS is composed of repeating units of siloxane (Si-O-Si) bends with methyl groups attached to the silicon atoms, which confer hydrophobicity and flexibility to the polymer (Hamouni et al., 2019). PDMS is a silicone-based organic polymer known for its density of 1.103 g $cm^{-3}$ (Hamouni et al., 2019), low density, thermal stability, flexibility, and biocompatibility properties make PDMS an ideal matrix for embedding filler materials like tin, enhancing the overall performance of the composite in radiation shielding applications (Al-Balushi et al., 2022; Aldawood et al., 2024). PDMS is widely used in various fields, including medical devices, microfluidics, and electronic components, due to its non-toxic nature and ease of processing.

When used in radiation shielding, PDMS offers several advantages, including flexibility and durability. PDMS flexibility allows for the creation of wearable and adaptable shielding materials that can be applied to blanket (El-Khatib, Alabsy, et al., 2024), curtain, or apron PPE (Ghule et al., 2024; B. Wang et al., 2023). The non-toxic and biocompatible nature of PDMS makes it suitable for applications in medical settings where direct contact with human tissue is required (Chang et al., 2023; Zhang et al.,

2017). Other polymers used in radiation shielding include polyethene, polyvinyl chloride (PVC), and epoxy resins. These polymers, often combined with high-density fillers such as bismuth, tungsten, or gadolinium, offer tailored solutions for specific radiation types and application requirements (Kim, 2023).

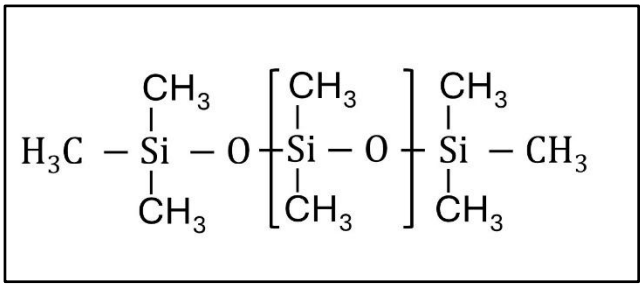

Figure 2.1 Chemical Structure of PDMS

## 2.6 Introduction of Tin as a Filler of PDMS Matrix for Shielding Application

The increasing demand for safer and more efficient radiation shielding materials has driven the exploration of alternative solutions to conventional lead shields. Among the promising candidates, tin has emerged as a potential filler in the PDMS matrix, offering a compelling combination of chemical properties, shielding efficiency, and reduced toxicity. This section provides a detailed overview of tin suitability as a filler in PDMS for radiation shielding applications, highlighting its chemical composition, shielding properties, and comparative toxicity, as well as introducing polymers used in radiation shielding.

The properties of the composite can be improved by applying the properties of the polymer for the lightweight and flexibility of the product (More et al., 2021; Nanda Karmaker et al., 2021a). Current material used for PPE is lead with a density of 11.34 g $cm^{-3}$ and an atomic number of 82. In its elemental form, tin is malleable, ductile, and resistant to corrosion due to the formation of a thin oxide layer that prevents further oxidation. These properties make tin an attractive alternative to lead, particularly when combined with PDMS, which enhances its mechanical flexibility and processing capabilities (Alım, 2020). Tin's efficacy as a radiation shielding material stems from its atomic structure and density, which enable it to attenuate gamma rays and X-rays effectively. Studies have demonstrated that tin-based composites can achieve significant attenuation coefficients, rivalling those of lead shields, while offering

additional benefits such as reduced weight and improved stability (Hubbell & Seltzer, 1995).

Moreover, tin relatively lower toxicity compared to lead and other heavy metals is a significant advantage. Lead exposure is known to cause severe health issues, including neurotoxicity, renal damage, and cardiovascular problems, making it hazardous to both human health and the environment (Cardis et al., 2005). In contrast, tin exhibits lower toxicity, posing less risk to human health and the environment. The properties of tin are summarised in Table 2.3. This reduction in toxicity is critical for applications where prolonged exposure to shielding materials is common, such as in medical and industrial settings (Safari et al., 2024).

Tin is considerably less toxic than lead in its elemental form. However, the toxicity of tin can vary depending on its chemical form, with organotin compounds being more harmful than inorganic tin. Elemental tin is generally considered to have low toxicity. It is not readily absorbed by the human body and is typically excreted without causing significant harm. Acute ingestion of tin can cause mild gastrointestinal distress, but it does not pose severe health risks (Glaser et al., 2023; More et al., 2021b). Compared to lead, tin is significantly less toxic in most of its forms.

Table 2.3
The Properties of Tin

| | |
|---|---|
| Atomic number | 50 |
| Atomic mass | 118.71 u |
| Density | 7.31 g $cm^{-3}$ |
| Crystal structure | Tetragonal |
| Corrosion resistance | High (due to protective oxide layer) |
| Malleability | High |
| Ductility | High |

While organotin compounds pose risks, the use of tin as a radiation shielding material typically involves its elemental or inorganic forms, which have low toxicity. This makes tin a safer alternative to lead, reducing the risk of chronic health issues and environmental contamination (Gouda et al., 2023). Tin is less persistent in the environment compared to lead. It does not bioaccumulate to the same extent and poses fewer risks to ecosystems. The environmental toxicity of tin compounds is also lower, making them less hazardous over long periods.

In addition to tin, other metals such as bismuth, tungsten, and gadolinium have been explored as fillers in metal-polymer composites (More et al., 2021a). Each of these

metals brings unique properties that enhance the composite shielding capabilities. For instance, bismuth and tungsten are known for their high density and effectiveness in gamma-ray attenuation, while gadolinium is particularly useful for neutron shielding due to its high neutron capture cross-section (Al-Balushi et al., 2022). Their research underscored the importance of achieving a fine balance between metal loading and polymer flexibility (R. Wang et al., 2018) to ensure optimal shielding without compromising the composite mechanical properties (Zhao et al., 2020).

Characterisation of metal-polymer composites involves assessing their structural, mechanical, and shielding properties. Techniques such as FESEM, XRD, and EDX have been extensively used to analyse the microstructure and elemental composition of the composites. These analyses are crucial for understanding the distribution of metal particles within the polymer matrix and their impact on the overall performance of the composite (Sahani & Dixit, 2022). The application of metal-polymer composites in radiation shielding has been driven by the need for materials that are not only effective but also safe and environmentally friendly. The transition from lead-based shields to composites made with less toxic metals like tin has been a major focus. Tin-based composites have gained attention due to their favourable properties, including lower toxicity and better compatibility with polymer matrices (Gouda et al., 2023).

## 2.7 Factors Affecting Shielding Efficiency

The efficiency of radiation shielding is influenced by several critical factors, including the material composition, thickness, density, and the energy of the radiation. These factors determine how efficiently a material can attenuate or block radiation, ensuring protection for human health. One of the factors is that the atomic number of the shielding material is a primary determinant of its efficiency (More et al., 2021a). Materials with high atomic numbers, such as lead, are used because lead provides superior attenuation of gamma and X-rays. However, recent research is exploring alternatives like tin and composite materials, which combine high-density elements with polymers to improve flexibility and reduce toxicity (Nakamura et al., 2024a). For instance, tin-PDMS composite leverages tin for its high atomic number and PDMS for its mechanical properties to create an effective, non-toxic shielding solution (Nakamura et al., 2024a; Zhao et al., 2020).

Next, the thickness and density of the shielding material significantly impact its ability to attenuate radiation (Kim, 2023). Greater thickness increases the path length over which radiation interacts with the material, enhancing attenuation. Similarly, higher density enhances the probability of interaction between the radiation and the shielding material atoms. Studies have shown that optimising these parameters can lead to substantial improvements in shielding efficiency. For example, increasing the thickness of a tin-PDMS composite layer can significantly enhance its effectiveness against high-energy radiation (Resende et al., 2024; Safari et al., 2024).

The energy of the radiation also plays a crucial role in determining the shielding efficiency. Low-energy radiation is more easily attenuated by thinner or less dense materials, while high-energy radiation requires more substantial shielding. For instance, composite materials have been engineered to provide optimal protection against both low-density and high-energy radiation, making them versatile for various applications (Gilys et al., 2022; Safari et al., 2024).

The long-term stability and integrity of the shielding material are essential for ensuring consistent protection over time. Factors such as environmental conditions, mechanical stress, and chemical stability can affect the material's performance. Recent advancements in material science have led to the development of composites with enhanced durability and stability, ensuring they maintain their shielding properties under different conditions (Deng et al., 2023; Jung et al., 2023).

Finally, the cost and practicality of the shielding material are important considerations, especially for large-scale or field applications. Materials that are expensive or difficult to fabricate and deploy may not be feasible despite their superior shielding properties. Research has focused on developing cost-effective and easily manufacturable materials, such as tin-PDMS composites, which offer a balance between efficiency, safety, and practicality (Ariati et al., 2021; More et al., 2021b).

## 2.8 Fabrication of a Composite using the Layering Technique

The development and optimisation of metal-polymer composites using layering techniques have been the subject of extensive research over the past few years. These composites, designed to combine the high atomic number and density of metals with the flexibility and processability of polymers, have shown significant promise in radiation shielding applications.

Layering techniques have been at the forefront of fabricating metal-polymer composites, offering precise control over the distribution and orientation of metal particles within the polymer matrix. One of the notable advancements is the layer-by-layer fabrication method, which allows for the sequential deposition of thin layers of metal and polymer. This method ensures uniformity and strong interfacial bonding, which are critical for the mechanical integrity and shielding efficiency of the composite (Gouda et al., 2023).

A study demonstrated the effectiveness of the layering technique in creating composites with enhanced radiation shielding properties. By optimising the thickness of each layer, they achieved a material that not only provided superior gamma-ray attenuation but also maintained flexibility and mechanical strength (Nakamura et al., 2024a; Zhao et al., 2020). Similarly, research on the use of tin as a filler in PDMS matrices highlights the benefits of the layering method in achieving a homogeneous distribution of tin particles and improved shielding performance (Poloskov et al., 2021).

The double-layer tin-PDMS composites in medical radiation shielding demonstrate their potential to replace traditional lead aprons and barriers. The study highlighted the benefits of using tin, including reduced weight and improved wearer comfort, without compromising on shielding efficiency (Alım, 2020). Similarly, researcher investigated the long-term stability of tin-based composites in harsh radiation environments, confirming their durability and consistent performance over extended periods (Chang et al., 2023). The layering technique in fabricating metal-polymer composites offers several advantages: Enhanced shielding efficiency is one of the primary advantages of the double-layered composite structure. The alternating layers of metal and polymer create multiple interfaces that increase the probability of gamma-ray interactions through absorption and scattering processes, thereby improving the overall attenuation performance.

Enhanced shielding efficiency is one of the primary advantages of the double-layered composite structure. The alternating layers of metal and polymer create multiple interfaces that increase the probability of gamma-ray interactions through absorption and scattering processes, thereby improving the overall attenuation performance. Layered composites can be designed to be flexible and conformable, making them suitable for wearable radiation protection and applications requiring material flexibility. Lastly, customisable properties. The properties of the composite can be tailored by adjusting the thickness and composition of the layers, allowing for the optimisation of

shielding efficiency and mechanical properties for specific applications (Dai et al., 2016).

Studies have shown that the layering technique significantly enhances the interfacial bonding between metal particles and the polymer matrix, which in turn improves the composite's mechanical strength and durability. For example, research demonstrated that composites fabricated using the layering technique exhibited superior tensile strength and elongation at break compared to those fabricated using conventional mixing methods (Gilys et al., 2022). The fabrication of metal-polymer composites often involves advanced techniques such as layering, which enhances the material's shielding efficiency and mechanical integrity.

Layering involves creating alternating layers of metal and polymer, which can improve radiation attenuation through multiple scattering and absorption processes. This technique also allows for precise control over the composite's thickness and composition, enabling the customisation of properties to meet specific needs. The development and optimisation of metal-polymer composites for radiation shielding are supported by extensive research and innovation. Studies have demonstrated the potential of these materials to replace traditional lead-based shields, offering significant benefits in terms of safety, environmental impact, and performance. As research progresses, the applications of metal-polymer composites are expected to expand, contributing to safer and more effective radiation protection solutions across various industries.

## 2.9 Radiation Shielding Against High-Energy Emission

High-energy electromagnetic radiation, such as gamma rays, emits high-energy photons capable of interacting with matter through several mechanisms, including the photoelectric effect, Compton scattering, and pair production. In the photoelectric effect, photons transfer their entire energy to tightly bound core electrons, ejecting them from their atomic orbitals if the photon energy exceeds the electron's binding energy. This process is more pronounced in materials with a high atomic number, since their inner-shell electrons are more strongly bound. Consequently, metals with higher density and atomic number (such as lead, W, or Bi) exhibit superior photon absorption properties, making them excellent candidates for radiation shielding materials to protect

human organs when used in PPE (I. J. Boniface & N. M. A. Mukhtar, 2020; J. A. Kamarolzeman & N. M. A, 2020; N. M. A. Mukhtar et al., 2024).

Composite that has features of enhanced flexibility, reduced weight, and improved mechanical strength, metal–polymer composites have emerged as an effective shielding solution. In a layered composite system, when gamma radiation passes through the high-density metallic layer, photoelectric absorption dominates due to the higher probability of photon–electron interactions in heavy atoms. This results in significant attenuation of the incoming photons, converting part of their energy into secondary electrons and characteristic X-rays.

As the attenuated beam passes into the second layer composed of a lower-density polymer, Compton scattering becomes the primary interaction mechanism to reduce the scattering ray (Kwon et al., 2023). Here, photons undergo inelastic collisions with loosely bound outer-shell electrons, resulting in the scattering of lower-energy photons in different directions. This process further reduces the overall photon energy and intensity, enhancing the shielding performance of the composite through a multi-mechanism attenuation process.

Thus, the synergistic effect between high-density metallic layers and low atomic number polymeric layers provides an optimised balance between photon absorption, scattering, and material weight. Such layered metal–polymer composites not only maximise gamma-ray attenuation efficiency but also improve comfort, flexibility, and practicality for radiation protection applications.

## 2.10 Previous Study on Tin and PDMS as Radiation Shielding Application

Table 2.4 summarises all the literature on the development and characterisation of metal-polymer composites as possible radiation shielding materials. Several previous studies have investigated the radiation shielding efficiency of metal and oxide in polymer matrices, particularly using PDMS and Si matrices.

The first study employs multiple-layer fabrication. The multilayered PDMS composites embedded with Sn, $CeO_2$, $WO_3$, and Bi exhibited significant gamma-ray attenuation across an energy range of 3.949 to 4.161 MeV. The metal loading varied between 8.7% and 42.6%, demonstrating that higher concentrations substantially enhance radiation shielding (Gilys et al., 2022). The reported LAC values ranged from 3.949 to 4.161 $cm^{-1}$, while the MAC varied between 0.020 and 0.160 $cm^2\ g^{-1}$.

Correspondingly, the HVL and TVL were in the range of 0.12 to 0.50 cm and 0 to 50 cm, respectively, indicating effective absorption at moderate thicknesses. The RPE reached as high as 94 to 97%, confirming that multilayer composites incorporating high-density elements such as Bi and $WO_3$ achieve excellent photon attenuation.

Next, study on nanoparticle and microparticle tin oxide PDMS. Nanoparticle (NP) and microparticle (MP) $SnO_2$ - Si composites prepared by mixing and curing exhibited a strong dependence of shielding performance on both filler size and concentration. At metal contents of 20% and 50%, and a thickness of 0.5 cm, the materials demonstrated LAC values between 0.059 and 1.408 $cm^{-1}$ (Gouda et al., 2023). MAC values were recorded between approximately 0.25 to 2.12 $cm^2\ g^{-1}$ for nano-particle samples and 0.5 to 6.5 $cm^2\ g^{-1}$ for MP samples. The HVL and TVL varied from 0.053 to 3.187 cm and 0.01 to 9.00 cm, respectively, while the RPE ranged from 11 to 100%. These results show that nanoparticle dispersion notably enhances attenuation, likely due to better interfacial bonding and more uniform distribution within the silicon matrix.

PDMS-based composites loaded with PbO and $SnO_2$ also show promising shielding. The PbO - PDMS composite, fabricated via mixing and curing with a metal loading of 50% and a thickness of 1.00 cm, demonstrated one of the most efficient gamma-shielding behaviours among PDMS-based systems. Over a radiation energy range of 0.059 to 1.332 MeV, the LAC decreased from 4.71 to 0.12 $cm^{-1}$ (Zhao et al., 2020), and the MAC correspondingly reduced from 3.65 to 0.10 $cm^2\ g^{-1}$. The HVL increased from 0.15 to 1.30 cm, while the TVL varied between 0.40 and 3.95 cm. RPE values ranged from 93% to 98%. The high LAC and low HVL confirm PbO superior photon absorption capability due to the high atomic number of leads, which effectively attenuates lower-energy photons through the photoelectric effect.

Similarly, $SnO_2$ - PDMS composites with 50 wt.% loading and 0.5 cm thickness prepared via mixing and curing showed moderate shielding capacity. Over the 0.059 to 1.332 MeV energy range, LAC values ranged from 3.20 to 0.09 $cm^{-1}$, with MAC between 2.59 and 0.05 $cm^2\ g^{-1}$ (Showahy et al., 2022). The HVL and TVL ranged between 1.9 cm and 2.02 cm and 4.30 cm and 6.80 cm, respectively. Despite a much lower RPE (16 to 17%) compared to PbO - PDMS, $SnO_2$ - PDMS remains valuable for lightweight, flexible shielding applications, where transparency and mechanical compliance are desirable over maximal attenuation.

In the other study, the shielding performance result of zinc oxide (ZnO) with PDMS confirms that, though of moderate atomic number, contributes appreciably to attenuation when finely dispersed, with significant efficiency at lower photon energies due to increased photoelectric interactions (Aladailah et al., 2022). ZnO - PDMS composites with 15 wt.% filler content and thicknesses of 0.10 to 0.20 cm showed LAC values decreasing from 5.40 to 0.09 $cm^{-1}$ as photon energy increased from 0.022 to 0.661 MeV. The corresponding MAC values were between 47.18 and 0.08 $cm^2\ g^{-1}$. HVL values ranged from 0.13 to 7.40 cm, and TVL from 0.19 to 24.54 cm.

Another previous study on PDMS fabricated by mechanical mixing and casting incorporating $Bi_2O_3$, $WO_2$, and $SnO_2$ oxides in PDMS matrices achieved excellent photon attenuation over 0.059 to 1.332 MeV. The LAC ranged between 5.500 to 0.055 $cm^{-1}$, and MAC from 4.10 to 0.06 $cm^2\ g^{-1}$ (Nazeri et al., 2025). HVL and TVL values spanned 0.11 to 0.45 cm and 0.36 to 1.48 cm, respectively. The combination of multiple high-density oxides synergistically enhanced attenuation performance while maintaining flexibility. Such hybrid composites balance mass efficiency with structural durability and are promising for flexible radiation barriers.

Composite fabricated by roll mill method also demonstrated high attenuation capability across 0.059 to 1.332 MeV with 10%, 20%, and 40% filler loadings and thicknesses between 2.0 to 8.4 cm (Yılmaz et al., 2020). The LAC and MAC ranged from 3.20 to 0.14 $cm^{-1}$ and 2.45 to 0.10 $cm^2\ g^{-1}$, respectively. The HVL increased from 0.10 to 0.42 cm, and TVL from 0.31 to 1.32 cm. The results confirm that increasing $Bi_2O_3$ content proportionally enhances attenuation due to its high atomic number and density, making it a strong non-toxic substitute for lead-based materials.

Another study on nanoparticle and microparticle fabrication in a PDMS matrix. Both microparticle and nanoparticle versions of these ternary PDMS composites, prepared by mixing and curing, exhibited a strong dependence on filler morphology (Gouda et al., 2023). The LAC values varied from 0.01 to 10.00 $cm^{-1}$ across the 0.059 to 1.408 MeV energy range. The HVL and TVL ranged from 0.03 to 10.00 cm and 0.10 to 35.00 cm, respectively. The nanoparticle-based composites showed smaller HVL and higher LAC values than their microparticle counterparts, emphasising that nanoscale fillers improve photon interaction probability and energy dissipation through enhanced interfacial scattering.

In another study, radiation shielding research was conducted by doping PDMS and TGV with metal fillers. Polymer matrices such as PDMS and TPV doped with

$CaCO_3$, Bi, W, and $Bi_2W_6O$ achieved notable attenuation in the 0.080 to 0.120 MeV energy range. LAC values were between 0.178 to 0.347 $cm^{-1}$ and MAC between 0.0182 to 0.0355 $cm^2\ g^{-1}$. HVL ranged from 0.17 to 1.54 cm (El-Khatib, Zard, et al., 2024a). The presence of heavy elements such as Bi and W contributed substantially to attenuation efficiency, while the TPV matrix provided mechanical flexibility suitable for dynamic shielding environments.

Lastly, thermoplastic polyurethane (TPU) composites layered with W, Bi, Sn, and Te exhibited superior attenuation performance, especially at higher energies (0.060 to 0.090 MeV). The LAC values reached up to 266.53 $cm^{-1}$, with a corresponding MAC of 71.44 to 12.60 $cm^3g^{-1}$. HVL values were as low as 0.007 to 0.002 cm, indicating exceptional photon absorption even at minimal thickness (Kwon et al., 2023). The combination of W and Bi provides dominant photoelectric and Compton scattering contributions, while the TPU matrix ensures processability and impact resistance.

Previous studies have explored layered polymer composites containing multiple high-Z fillers; however, most reported designs focused on incorporating various shielding fillers within polymer matrices or combining different filler compositions to enhance attenuation performance. In contrast, the present study introduces a double-layered Sn-PDMS composite design by arranging two different metal-containing PDMS layers with controlled irradiation surfaces. This approach enables investigation of the influence of filler distribution and irradiation-facing materials on gamma-ray attenuation performance, which has not been extensively reported for tin-based polymer composites.

Table 2.4
Findings from Previous Studies

| References | Metal /Polymer | Fabrication Technique | Metal (%) | Thickness (cm) | Radiation Energy (MeV) | Radiation properties | | | | |
|---|---|---|---|---|---|---|---|---|---|---|
| | | | | | | LAC ($cm^{-1}$) | MAC ($cm^2\ g^{-1}$) | HVL (cm) | TVL (cm) | RPE (%) |
| (Gilys et al., 2022) | Sn, $CeO_2$, $WO_3$, Bi - PDMS | Layering | 8.7<br>21.6<br>42.6<br>14.3 | 3.949 – 4.161 | 0.020 - 0.160 | 3.949 – 4.161 | 0.020 – 0.160 | 0.12 – 0.50 | 0 – 50 | 94-99 |
| (Gouda et al., 2023) | Nano-particle-$SnO_2$ - Si,<br>Micro-particle-$SnO_2$ - Si | Mixing and curing | 20, 50<br>20, 50 | 0.5 | 0.0596 - 1.408 | ~ 0.25- 2.125,<br>~0.5- 6.5<br>~0.25-1.625,<br>~0.5-~5.1 | 0.053 - 3.187 | 0.01-9 | 0.1-25 | 11-100 |
| (Showahy et al., 2022) | ZnO - PDMS | Mixing and curing | 0<br>2.5<br>5<br>7.5<br>10<br>15 | 0.1-0.2 | 0.059 – 1.332 | 2.10 – 0.09 | 1.80 – 0.07 | 0.18 – 0.97 | 0.35 – 1.54 | 72 – 94 |
| (Nazeri et al., 2025) | Micro-particle - $SnO_2$, CdO, $Bi_2O_3$ - PDMS<br>Nano-particle - $SnO_2$, CdO, $Bi_2O_3$ - PDMS | Mixing and curing | 0<br>20<br>50 | - | 0.05954 – 1.408 | 0.01-10 | 0.2186-0.0578<br>1.1663-0.0570<br>2.5578-0.0537 | 0.03 – 10 | 0.10 – 35 | - |

| References | Metal /Polymer | Fabrication Technique | Metal (%) | Thickness (cm) | Radiation Energy (MeV) | Radiation properties | | | | |
|---|---|---|---|---|---|---|---|---|---|---|
| | | | | | | LAC ($cm^{-1}$) | MAC ($cm^2$ $g^{-1}$) | HVL (cm) | TVL (cm) | RPE (%) |
| (Zhao et al., 2020) | $Bi_2O_3$, $WO_2$, $SnO_2$ - PDMS | Mixing and casting | - | 0.08 | 0.059 – 1.332 | 5.50 – 0.055 | 4.10 – 0.06 | 0.11 – 0.45 | 0.36 – 1.48 | - |
| (Yılmaz et al., 2020) | PbO - PDMS | Mixing and curing | 50 | 1.00 | 0.059–1.332 | 4.71 – 0.12 | 3.65 – 0.10 | 0.15 – 1.30 | 0.40 – 3.95 | 93 – 98 |
| (Aladailah et al., 2022) | $Bi_2O_3$ - PDMS | Roll mill | 10<br>20<br>40 | 2.0<br>6.1-6.3<br>8.0-8.4 | 0.059 – 1.332 | 3.20 – 0.14 | 2.45 – 0.10 | 0.10 – 0.42 | 0.31 – 1.32 | 85 – 96 |
| (El-Khatib, Zard, et al., 2024) | W, Bi, Sn, Te - TPU | Layering | - | 0.195-0.415 | 0.060-0.090 | 266.53<br>71.44<br>12.60<br>96.25 | - | 0.007-0.002 | - | 15 - 70 |
| (El-Khatib, Zard, et al., 2024) | $CaCO_3$<br>Bi<br>W<br>$Bi_2W_6O$ - PDMS,TPV | Doping | - | 0.2-0.5 | 0.080 – 0.120 | 0.178 – 0.347 | 0.0182 – 0.0355 | 0.17-1.54 | - | - |

# CHAPTER 3
# RESEARCH METHODOLOGY

## 3.1 Introduction

The methodology for this study is divided into four stages, as illustrated in Figure 3.1. Stage I involves the mixing and curing process for double layer composite. Three series of samples are produced: (i) pure tin - PDMS (PS series), (ii) tin alloy - PDMS (AS series), and (iii) pure tin – PDMS, tin alloy - PDMS (TM series), consisting of tin alloy and pure tin in a PDMS matrix. Stage II focuses on sample characterisation using multiple techniques: FESEM - EDX for morphological and elemental analysis, for functional group identification, and XRD for structural and phase analysis. Stage III evaluates the radiation-shielding properties of the composites by exposing them to photon energies ranging from 59.5 to 1332.5 keV. Radiation characteristics such as LAC, MAC, HVL, TVL, and RPE are measured. Finally, Stage IV involves data analysis and documentation, where all experimental results are processed, compared, and interpreted to assess the shielding effectiveness of the composites.

## 3.2 Stage I: Mixing and Curing Process for Double Layer Composite

### 3.2.1 Raw Material

The raw materials used in this study consisted of metal powders and a polymer matrix. Pure tin powder, with a density of approximately 7.31 g $cm^{-3}$, was obtained from Bendosen, Kuala Lumpur, Malaysia, while the tin alloy powder, with a density of about 8.8 g $cm^{-3}$, was supplied by Sigma Aldrich, Taufkirchen, Germany. Both pure tin and tin alloy powders were provided in micron-sized particulate form, as illustrated in Figure 3.2 (b) and (c). The polymer matrix employed was PDMS, the Sylgard 184 Silicone Elastomer Kit (Dow Corning, USA), which included both the PDMS elastomer base, shown in Figure 3.2 (a).

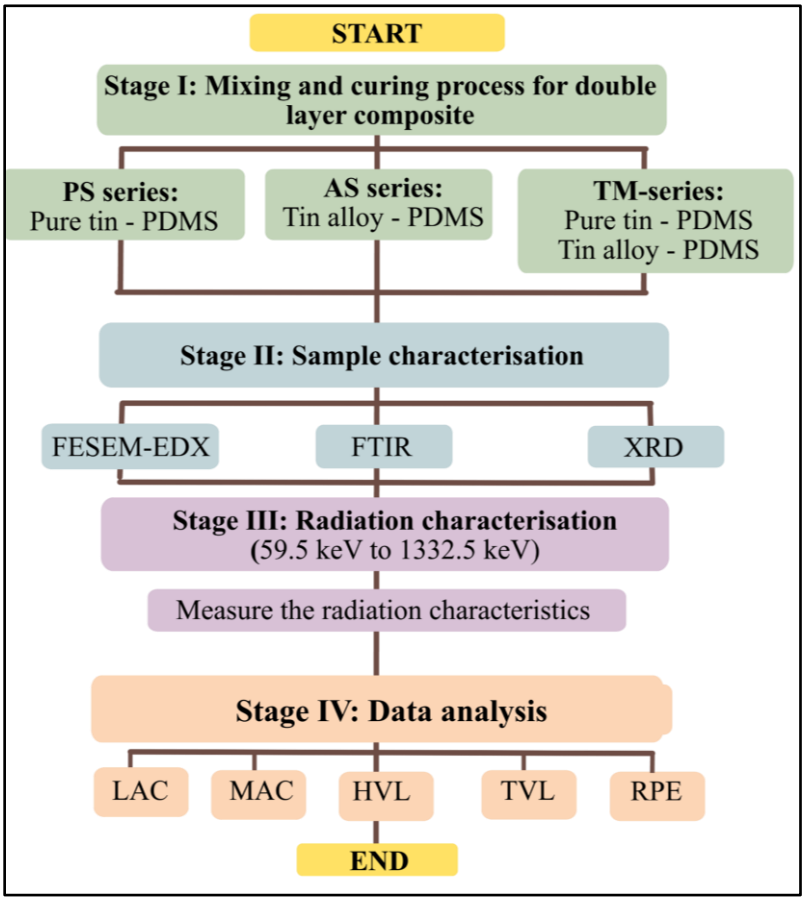


Figure 3.1 Flowchart of Research Methodology




Figure 3.2 Raw Materials Used to Fabricate Tin-PDMS Composites: (a) Sylgard 184 Silicone Elastomer-Based PDMS; (b) Pure Tin Powder, and (c) Tin Alloy Powder

To prepare the polymer, the PDMS elastomer base was mixed with its curing agent at a ratio of 10:1 by weight, in accordance with the supplier's recommendation, producing a cured polymer with a density of approximately 1.103 g $cm^{-3}$. Pure tin has a melting / freezing point of ~231.9 °C, whereas the tin alloy exhibited a slightly broader

melting range (200 – 250 °C), depending on its specific composition. These materials were selected based on their suitable density, stability, and processability, making them appropriate candidates for the development of radiation shielding composites. Other details of the raw material were tabulated in Table 3.1.

Table 3.1
Raw Materials Parameters

| Parameters | Raw materials | | |
|---|---|---|---|
| | **Pure tin** | **Tin alloy** | **PDMS** |
| Manufacturer | Bendosen, Kuala Lumpur, Malaysia | Sigma Aldrich, Taufkirchen, Germany | Dow Corning, USA (Sylgard 184 Kit Set) |
| Symbol | Sn | Sn-based alloy | PDMS |
| Shape/form | Powder (metal powder) | Powder (metal powder) | Liquid polymer (elastomer base + curing agent) |
| Size | Micron-sized powder | Micron-sized powder | - |
| Density | ~7.31 g $cm^{-3}$ | ~8.8 g $cm^{-3}$ | ~1.13 g $cm^{-3}$ |
| Melting temperature | ~231.9 °C | ~200 – 250 °C (composition dependent) | - |
| Freezing temperature | ~231.9 °C | ~200 – 250 °C | - |

### 3.2.2 Mixing and Curing of the Composite by the Layering Technique

A multilayer composite sample with dimensions of 2.0 cm x 2.0 cm x 0.5 cm was fabricated at the UiTM Cawangan Pulau Pinang using the layering technique. Each composite consisted of two layers, approximately 0.25 cm thick per layer. Layer 2 was prepared by mixing tin powder with PDMS polymer in specific composition ratios as shown in Table 3.2. For the PS and AS series, Layer 1 was fabricated using 100% PDMS to provide a pure polymer surface, whereas for the TM series, both Layer 1 and Layer 2 were prepared using tin–PDMS mixtures to achieve higher filler loading and improved shielding characteristics. This design enabled comparison between composites with a pure polymer outer surface and those with fully metal–polymer integrated layers, providing insights into the influence of layering configuration on radiation attenuation.

#### *3.2.2.1 Curing Condition Determination*

At this stage, the curing condition was initially studied and optimised to obtain the best curing conditions for the composite fabrication process. Four (4) curing temperatures and times have been suggested by the PDMS manufacturer, which are room temperature for 24 to 48 hours, 100 °C for 35 minutes, 125 °C for 20 minutes, and 150 °C for 10 minutes.

In this process, 20% pure tin composites, namely Sample A, Sample B, and Sample C, were fabricated with the following curing conditions before being evaluated under FESEM analysis: Sample A at room temperature for 24 hours, Sample B at 100 °C for 35 minutes, and Sample C at 125 °C for 20 minutes. The results suggested the best curing condition was at room temperature for 24 hours. This is due to the composites experiencing high-temperature heating curing at 100 °C and 125 °C, two (2) times for each composite, due to the layer-by-layer fabrication method. Structural characterisation from FESEM images shows that the pure tin particles were well distributed, but for Samples B and C, the PDMS structure of the first layer shrank and showed poor interfacial adhesion between layers. The best structural particles and good interfacial adhesion composite is Sample A, which was cured at room temperature for 24 hours.

#### *3.2.2.2 Sample Fabrication Condition*

As for the first layer, the tin and PDMS were mixed and stirred for about 7 to 10 minutes before being poured into the mould, to ensure the powders can be dispersed uniformly throughout the polymer matrix. The mixture was then cured for 24 hours in a desiccator to ensure complete solidification occurred. The process was repeated for the remaining compositions, such as 10%, 20%, 30%, 40%, 50%, and 60%, to create layers with varying compositions. After the first layer had solidified, fabrication of the second layer continued by preparing a 100% PDMS layer. At this stage, the 100% PDMS liquid polymer was poured on top of the cured mixed monolayer, at the same thickness, followed by the same curing procedure described previously. The overview of the composition ratio is shown in Table 3.2.

Table 3.2
Composition ratio of composite fabrication

| Filler / Matrix | Composite label | Filler composition of each layer | |
|---|---|---|---|
| | | Layer 1 | Layer 2 |
| PDMS | Control PDMS | 100% PDMS | |
| Lead | Control lead | 100% lead | |
| Tin | Control tin | 100% pure tin | |
| Pure tin - PDMS (PS series) | PS1 | 0 | 10% pure tin |
| | PS2 | 0 | 20% pure tin |
| | PS3 | 0 | 30% pure tin |
| | PS4 | 0 | 40% pure tin |
| | PS5 | 0 | 50% pure tin |
| | PS6 | 0 | 60% pure tin |
| Tin alloy - PDMS (AS series) | AS1 | 0 | 10% tin alloy |
| | AS2 | 0 | 20% tin alloy |
| | AS3 | 0 | 30% tin alloy |
| | AS4 | 0 | 40% tin alloy |
| | AS5 | 0 | 50% tin alloy |
| | AS6 | 0 | 60% tin alloy |
| Pure tin – PDMS Tin alloy - PDMS (TM series) | TM1 | 10% pure tin | 10% tin alloy |
| | TM2 | 20% pure tin | 20% tin alloy |
| | TM3 | 30% pure tin | 30% tin alloy |
| | TM4 | 40% pure tin | 40% tin alloy |
| | TM5 | 50% pure tin | 50% tin alloy |
| | TM6 | 60% pure tin | 60% tin alloy |

### 3.2.3 Calculation of Effective Density

The density of each layer in the double-layer tin–PDMS composite differs due to variations in filler concentration and material composition. Therefore, the most appropriate method for determining the density of each sample is to calculate the effective density of the overall composite. After the composite is fully cured, two parameters are recorded: (i) the total weight of the composite and (ii) the thickness of each layer. The thickness of the sample was measured by using an electronic vernier caliper, as shown in Figure 3.3. The reading was repeated three (3) times, and the average was taken.

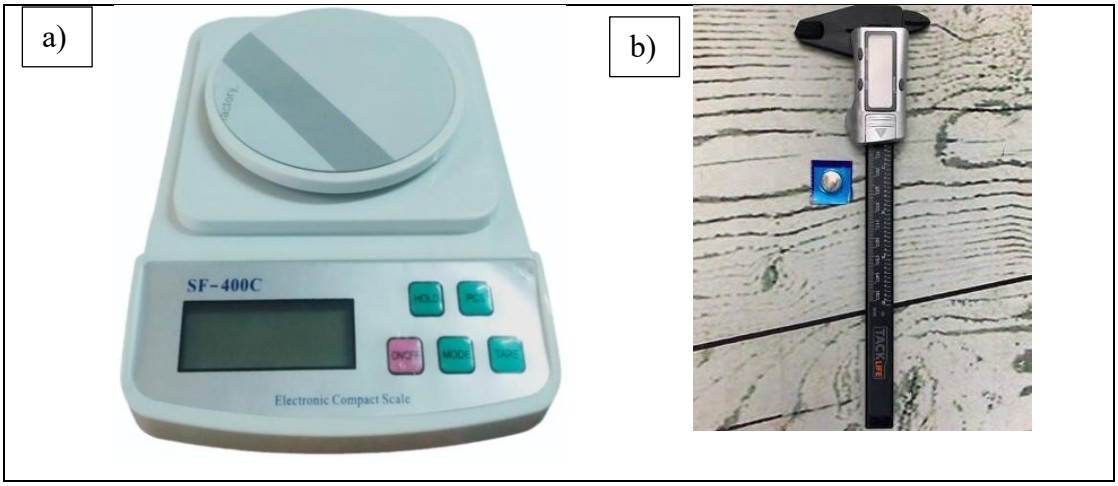


Figure 3.3 Instruments Used to Calculate The Physical Properties and Dimensions of Composites: (a) Weighing Balance, (b) Electronic Vernier Caliper

The mass per unit area of each layer is then calculated based on the known ratio of materials and the measured thickness of the layer. Subsequently, Equations (2.2) and (2.3) in Section *2.3.2.1* are applied to determine the effective density of the composite structure. The theoretical effective density is calculated based on the constituent material densities and their respective volume fractions to assess the accuracy of the measured effective density. The percentage difference between the measured and theoretical values is then determined to ensure that the experimental results are consistent with theoretical expectations and that the fabrication process produced uniform and reliable composite samples.

## 3.3 Stage II: Sample Characterisation

Stage II involved morphological and structural characterisation of the samples. The samples were subjected to a morphological and structural study of the cross-sectional sample using FESEM/EDX, XRD, FTIR. Facilities at Usains Biomics Laboratory Testing Services Sdn Bhd, Universiti Sains Malaysia (USM), were used for FESEM - EDX and XRD analyses. For the FTIR analysis, the procedure was conducted at Universiti Putra Malaysia (UPM).

### 3.3.1 Field Emission Scanning Electron Microscopy / Energy Dispersive X-ray Spectroscopy

FESEM provides high-resolution imaging of material surfaces with nanoscale precision and is an essential technique for analysing morphological and structural characteristics of the composites, as shown in Figure 3.4 (a). EDX determined the elemental composition and measured the oxygen concentration to assess potential microstructural defects, while FESEM offered high-resolution images to study the topography and nanoscale characteristics of each sample. In the procedure, the samples were coated with a gold layer approximately 10 nm thick using a sputter coater, and then fixed to stubs with colloidal copper tape, as shown in Figure 3.4 (b).

The FESEM/EDX analysis was performed using an FEI Verios 460L model, at an accelerating voltage of 15 kV and a beam current of 1.6 nA, which provided adequate surface resolution and minimised charging. A thorough understanding of material properties is made possible by FESEM 3D imaging capabilities.

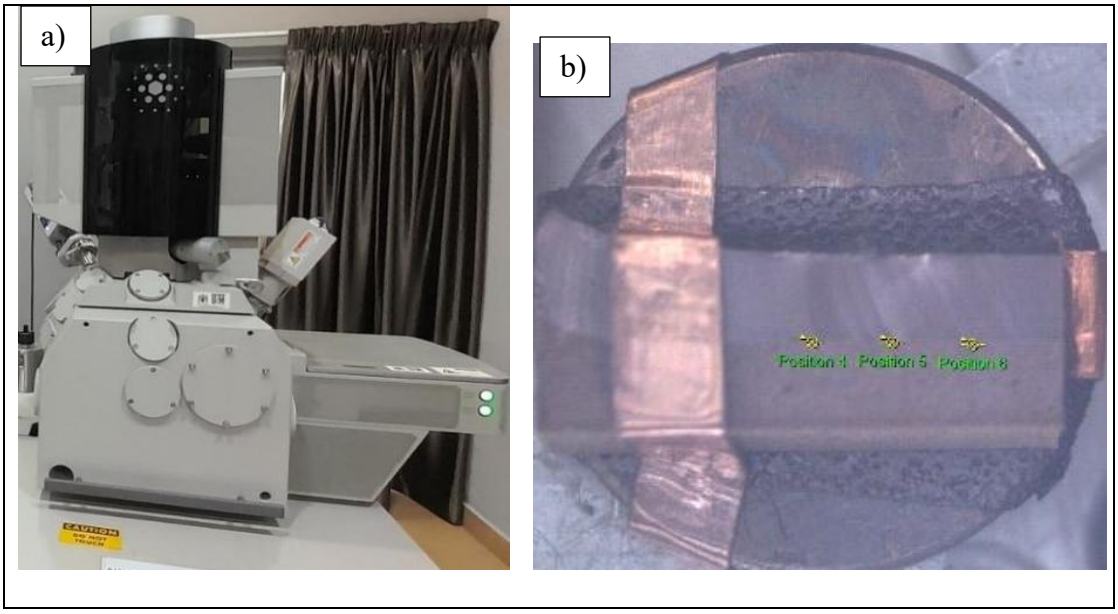


Figure 3.4 FESEM/EDX Instrumentation and Procedure: (a) FESEM Model and (b) Gold-Coated and Copper Tape Coiled for FESEM Analysis

### 3.3.2 Fourier Transform Infrared Spectroscopy

FTIR spectroscopy was conducted at UPM with the facility brand PerkinElmer, model Spectrum 100 series, as shown in Figure 3.5. FTIR spectroscopy analysis generates spectroscopic profiles containing chemical identifiers that enable researchers

to observe both functional group activation and component bonding interactions. The wavenumber range of 4000 to 400 $cm^{-1}$ is used to acquire molecular vibration data on samples at room temperature. This technique analyses infrared vibration and characterises molecular interaction to give chemical structure examination of radiation shield tin-PDMS composites. The sample absorbs infrared wavelengths during the FTIR method of infrared light transmission.



Figure 3.5 Fourier Transform Infrared (FTIR) Spectroscopy, Brand PerkinElmer, Model Spectrum 100 Series

### 3.3.3 X-Ray Diffraction

The crystalline structure and identification of the phase of the samples of the composite were investigated through XRD analysis with a Bruker D8 Advance diffractometer, as shown in Figure 3.6. Using X-ray radiation, the instrument can analyse the principles of atoms in the material to realise qualitative analysis of phases according to diffraction patterns. To collect and analyse the diffraction data, DIFFRAC.EVA Version 1.4 software with the ICDD PDF-2 database was used. The evaluation of the phase was done by making a comparison between the experimental

values of d-spacing and the database d-spacing. This enabled the proper description of mineral or material phases contained in each sample.

In XRD analysis, an X-ray source is directed onto a crystalline sample, causing the crystal lattice to scatter the X-rays. The diffraction pattern created by the diffracted X-rays is analysed to disclose details about the atoms' arrangement within the crystal structure. The test also sheds light on the intricacy of the integration and interaction between metal and polymer. For example, the presence of foreign atoms is expected if the peak displays an additional unknown phase (Jadav et al., 2013).




Figure 3.6 Bruker D8 Advance Diffractometer

## 3.4 Stage III: Radiation Characterisation

All composites were undergoing radiation characterisation utilising photon rays at the Faculty of Science and Technology, UKM, including three control samples. During this process, ionising radiation was evaluated by measuring the gamma intensity of both the incident and transmitted rays as they passed through the composite samples of varying thicknesses. The gamma-ray spectroscopy setup, as illustrated in Figure 3.7, consists of a sodium iodide activated with thallium [NAI(TI)] scintillation detector, an electronic circuitry system, and a multiple pulse-height analyzer (MCA).



Figure 3.7 A Gamma-Ray Spectrometer Used for Radiation Characterisation

By dedicated software, a personal computer functions as the multichannel analyser (MCA), providing enhanced data processing and analytical capabilities. Before measurement, the [NAI(TI)] scintillation detector was calibrated using a cobalt-60 (Co-60) standard source, which emits two well-defined gamma energy peaks at 1173.2 keV and 1332 keV. This calibration ensured accurate energy resolution and intensity measurements throughout the experiment. The identification of radioactive isotopes was achieved by analysing the unique spectral characteristics of the gamma rays and their interaction patterns with the composite materials. These distinct spectral features allow each isotope to be identified based on its characteristic energy peaks. During the radiation characterisation, the composite samples were positioned between the photon source and the [NAI(TI)] scintillation detector to measure the transmitted gamma intensity (I). The corresponding setup used for this measurement is shown in Figure 3.8.

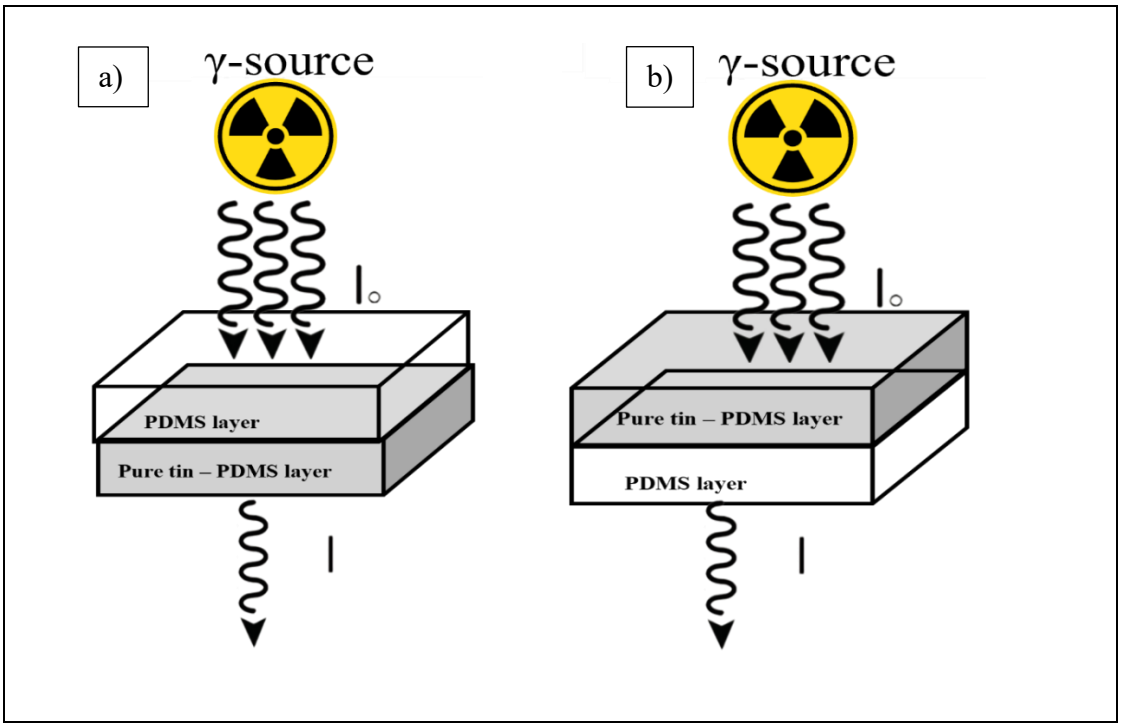


Figure 3.8 Illustration of The Gamma Irradiation Characterisation: (a) PDMS Irradiation Surface and (b) Mixture Irradiation Surface (Tin/Alloy)

Each composite recorded two data sets, corresponding to the direction of radiation, namely, the mixture irradiation surface and the PDMS irradiation surface, shown in Figure 3.8. This study examines the transmitted rays, emitted from radionuclides as tabulated in Table 3.3, that pass through two different composition layers as a radiation shielding. The initial intensity ($I_0$) and transmitted intensity (I) were recorded and used to calculate the radiation properties further, using the equations stated in Section *2.2.3.2* to *2.2.3.6*.

Table 3.3
The Gamma-Ray Sources Used for The Radiation Characterisation

| **Gamma sources** | **Symbol** | **Energy (keV)** |
|---|---|---|
| Americium – 241 | Am-241 | 59.5 |
| Cadmium – 109 | Cd-109 | 88.0 |
| Cobalt – 57 | Co-57 | 122.1 |
| Barium – 133 | Ba-133 | 356.0 |
| Cesium – 137 | Cs-137 | 661.7 |
| Manganese – 54 | Mn-54 | 834.8 |
| Cobalt – 60 | Co-60 | 1173.2<br>1332.5 |

## 3.5 Radiation Parameters Calculation

In this final phase, the results obtained from the experimental work were carefully analysed and interpreted. The raw data from structural, thermal, and radiation characterisations were compiled, summarised, and presented in tables and figures to highlight key trends and compare the performance of the different composite series with the control samples. For the radiation parameters, LAC, MAC, HVL, TVL, and RPE were evaluated over a gamma energy range from 88.0 to 834.8 keV. Comparative analyses were performed for the different irradiation surface configurations to assess their relative shielding effectiveness. The findings were critically interpreted with reference to previous studies and supported by relevant computational data, serving as a basis for validating the results and identifying potential directions for further research. Tables, graphs, and figures were prepared to present the outcomes clearly, allowing both quantitative and qualitative assessment of the materials' performance. The Beer-Lambert law provides a calculation LAC, MAC, and other properties as specified in Chapter 2, Section 2.2.2. The data for each energy were then compared with the theoretical value of the radiation properties of control lead through the software of WinXCOM and Phy-x. This is to ensure the validity of data taken by using the various ranges of energy.

# CHAPTER 4
# RESULTS AND DISCUSSIONS

## 4.1 Introduction

This chapter presents the findings obtained from the characterisation and evaluation of the developed tin–PDMS composites, with a particular focus on their structural, morphological, chemical, and radiation shielding properties. The discussion begins with morphological analysis performed using FESEM, which provides detailed insight into the surface texture, dispersion of fillers, and interfacial adhesion between the polymer and metallic phases. Representative FESEM micrographs are shown for the control PDMS, the PS series, the AS series, and the TM series, serving as the basis for comparative morphological evaluation. Elemental distribution within the composites was further analysed using EDX, allowing both weight and atomic percentage quantification of the constituent elements and enabling assessment of filler incorporation and dispersion uniformity. Structural characterisation was carried out through XRD, which provided phase identification and crystallinity analysis. Meanwhile, chemical bonding and polymer filler interactions were investigated using FTIR. The radiation attenuation performance of the composites was systematically evaluated using key shielding parameters, namely LAC, MAC, HVL, TVL, and RPE. Together, these analyses provide a comprehensive understanding of the influence of filler type, morphology, and concentration on the physical and radiation shielding properties of the composites, enabling comparison across the PS, AS, and TM series and with the control PDMS.

## 4.2 Fabricated Sample

This section presents the schematic diagrams and fabricated samples prepared for this study, including the control samples and the three composite series. Each sample was fabricated according to the optimised composition ratios and curing condition discussed in the Section 3.2.2.2, ensuring uniform thickness and homogeneity distribution of metal filler in the PDMS matrix. Figure 4.1 presents the control samples. Figure 4.1(a) shows the fabricated control PDMS, which was cured at room temperature

for 24 hours. Figures 4.1(b) and 4.1(c) display conventional, commercially purchased metal plates. These plates were cut to dimensions of 2.0 cm x 2.0 cm x 0.5 cm using a hand saw. All 21 fabricated samples were prepared with identical dimensions to ensure consistent comparison of their properties, including radiation shielding performance.

Figure 4.2(a) illustrates the schematic diagram of the double-layer tin–PDMS composite (PS series). In this schematic diagram, the grey layer represents the mixture of pure tin and PDMS, while the transparent layer corresponds to the pure PDMS layer, as shown in Figure 4.2(b). A similar transparent PDMS layer is also present in the AS series, as shown in Figure 4.3. In this series, the brownish layer represents the mixture of tin alloy and PDMS. In contrast, the TM series does not contain a transparent PDMS layer because both layers in this composite consist of mixtures of tin and PDMS. As shown in Figure 4.4, the grey layer corresponds to the mixture of pure tin and PDMS, whereas the brownish layer represents the mixture of tin alloy and PDMS.

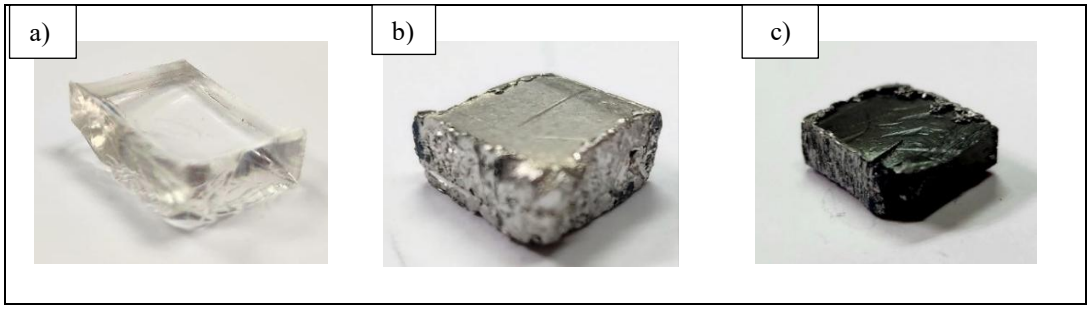


Figure 4.1 Control Samples: (a) PDMS, (b) Tin Plate, and (c) Lead Plate

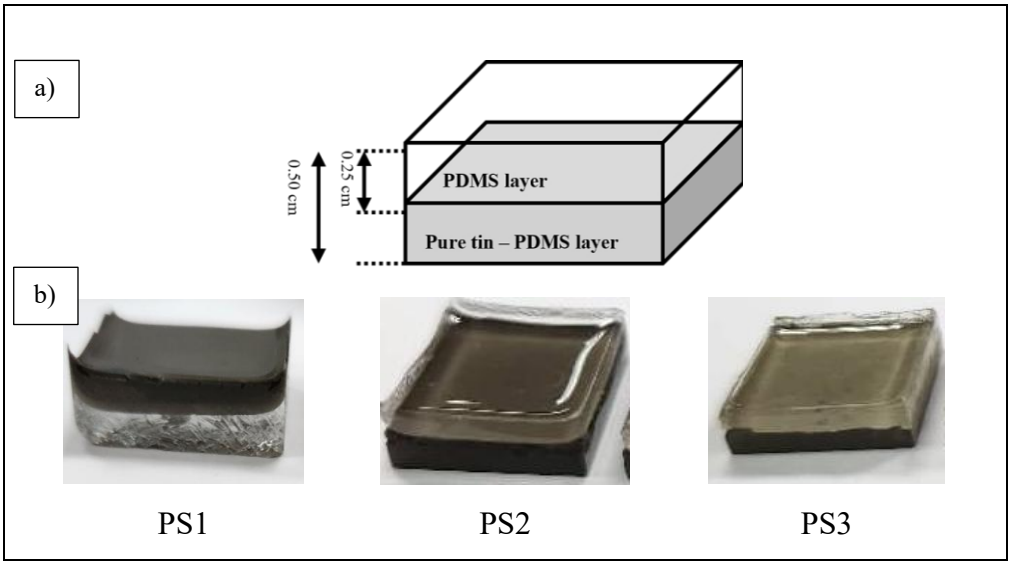




Figure 4.2 PS Series: a) Schematic Diagram, and b) Six (6) Fabricated Samples

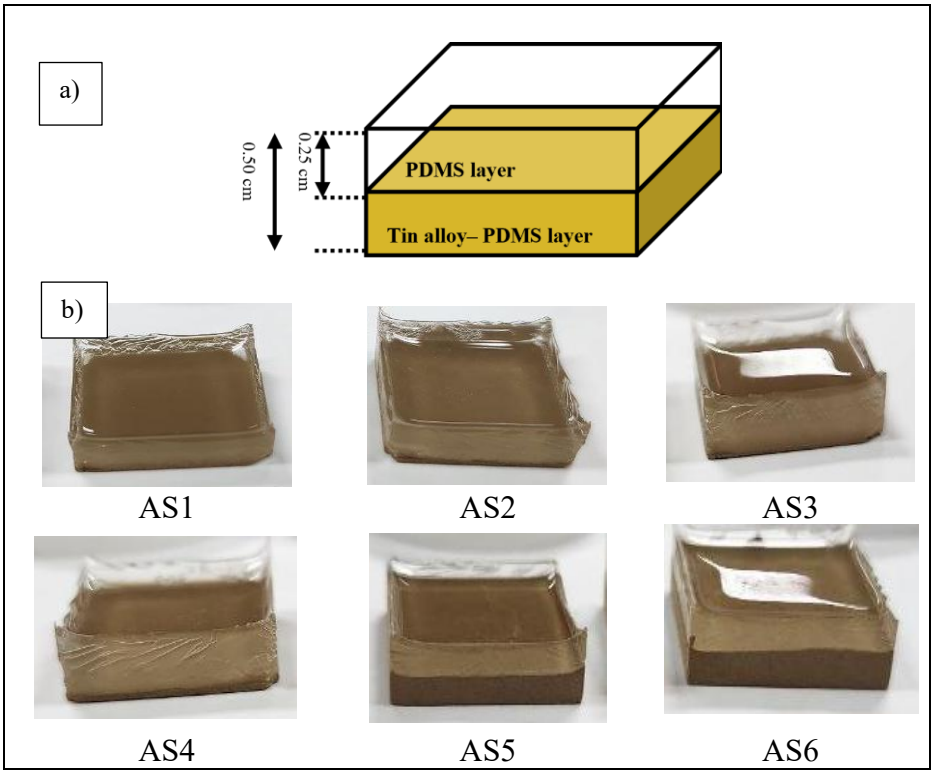


Figure 4.3 AS Series: a) Schematic Diagram, and b) Six (6) Fabricated Samples

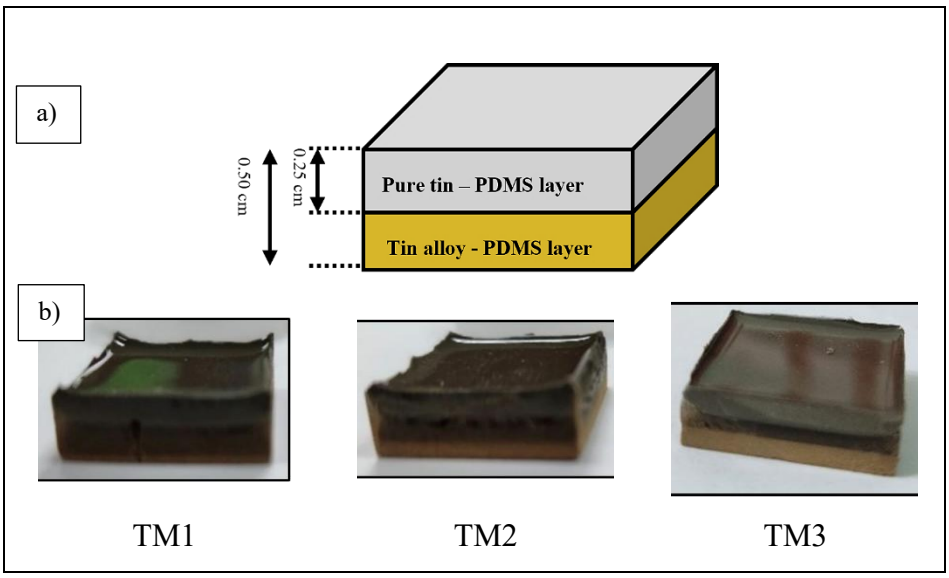

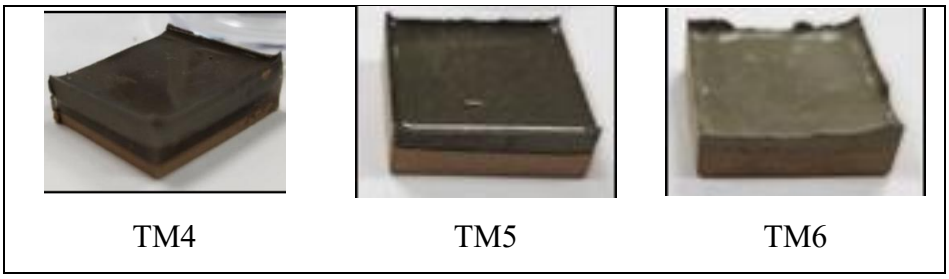

Figure 4.4 TM Series: a) Schematic Diagram, and b) Six (6) Fabricated Samples

## 4.3 Effective Density

The effective density represents the overall density of the double-layer tin–PDMS composite, calculated using Equations (2.1) to (2.4) in Section 2.2.2.1. The density results of the control and composite samples are summarised in Table 4.1. For the control materials, only theoretical densities were considered 1.103 g $cm^{-3}$ for PDMS, 7.31 g $cm^{-3}$ for pure tin, and 11.34 g $cm^{-3}$ for lead. These values reflect the intrinsic densities of the constituent materials and serve as reference benchmarks for evaluating the fabricated composites.

For the composite series, both effective and theoretical densities were determined to assess the influence of filler incorporation and fabrication quality. The percentage difference between the two values indicates the degree of packing efficiency, filler distribution uniformity, and potential porosity within the multilayer structure.

The PS series exhibited a steady increase in both effective and theoretical density with higher tin content, from 1.36 g $cm^{-3}$ for PS1 to 3.15 g $cm^{-3}$ for PS6. This trend confirms the successful integration of the high-density tin filler within the PDMS matrix. However, relatively large percentage differences (3.54 to 20.53%) were recorded, particularly in PS2 (20.53%) and PS4 (16.78%), suggesting the presence of microvoids or uneven filler dispersion during curing. In contrast, PS6 demonstrated a much closer agreement between effective and theoretical densities, differing by only 6.11%, indicating improved homogeneity and reduced porosity at higher filler loading.

The AS series also showed a consistent upward trend in density, ranging from 1.24 g $cm^{-3}$ in AS1 to 3.42 g $cm^{-3}$ in AS6. Early samples (AS1 and AS2) displayed larger discrepancies of 16.52% and 22.35%, respectively, which may be attributed to irregular filler dispersion or air entrapment during processing. As the filler concentration increased, the differences between measured and predicted densities decreased

significantly, reaching only 2.77% for AS5 and an exceptional 0.07% for AS6. The near-perfect match for AS6 signifies highly compact filler packing, excellent interfacial bonding, and minimal porosity, confirming an improvement in fabrication consistency at higher alloy loadings.

Table 4.1
Calculated Density for Multilayered Tin-PDMS Composite.

| Composite Label | Density | | |
|---|---|---|---|
| | Effective (g $cm^{-3}$) | Theoretical (g $cm^{-3}$) | Percentage difference (%) |
| Control PDMS | 0.96 | 1.10 | 12.72 |
| Control Lead | - | 11.34 | - |
| Control Tin | - | 7.31 | - |
| PS1 | 1.36 | 1.41 | 3.54 |
| PS2 | 1.37 | 1.72 | 20.53 |
| PS3 | 1.83 | 2.03 | 10.20 |
| PS4 | 1.95 | 2.34 | 16.78 |
| PS5 | 2.34 | 2.66 | 12.05 |
| PS6 | 3.15 | 2.97 | 6.11 |
| AS1 | 1.24 | 1.49 | 16.52 |
| AS2 | 1.45 | 1.87 | 22.35 |
| AS3 | 2.32 | 2.26 | 2.90 |
| AS4 | 2.79 | 2.64 | 5.62 |
| AS5 | 3.11 | 3.03 | 2.77 |
| AS6 | 3.42 | 3.41 | 0.07 |
| TM1 | 1.77 | 1.80 | 1.57 |
| TM2 | 2.47 | 2.49 | 0.90 |
| TM3 | 3.24 | 3.19 | 1.61 |
| TM4 | 3.96 | 3.88 | 1.91 |
| TM5 | 4.69 | 4.58 | 2.40 |
| TM6 | 5.32 | 5.27 | 0.94 |

The TM series demonstrated the highest overall densities and the smallest variations between calculated and theoretical values. The effective density increased from 1.77 g $cm^{-3}$ for TM1 to 5.32 g $cm^{-3}$ for TM6, while the percentage difference remained consistently low (0.90 to 2.40%). TM6 achieved an effective density of 5.32 g $cm^{-3}$ compared to a theoretical density of 5.27 g $cm^{3}$, with only a 0.94% difference, indicating superior filler dispersion, compact structure, and near-ideal packing efficiency. The excellent agreement between experimental and theoretical densities

confirms that the layering and curing process effectively minimised void formation and ensured strong interfacial adhesion between layers.

The bar chart in Figure 4.5 visually compares the effective and theoretical densities for the PS, AS, and TM series, highlighting the overall agreement between measured and predicted values. In most cases, the effective densities closely follow the theoretical trend, with minor deviations attributable to slight porosity, microstructural irregularities, or experimental uncertainties. The PS and AS series show progressive improvements across their sample range, while the TM series demonstrates remarkable consistency and accuracy.

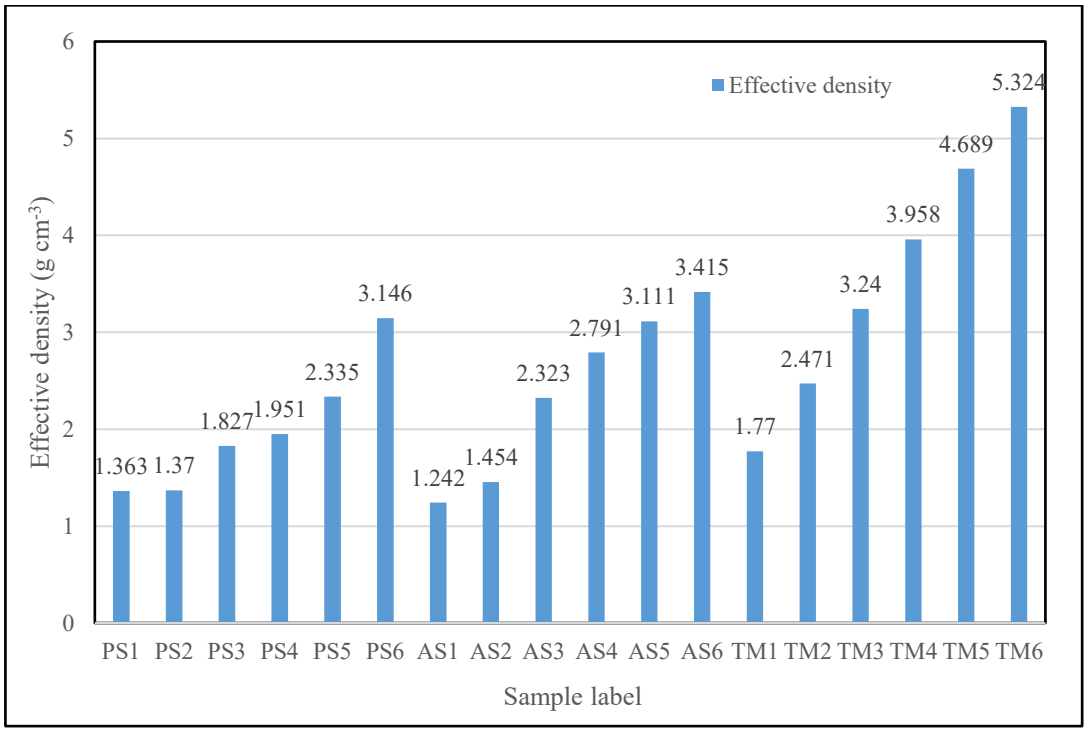


Figure 4.5 Effective and Theoretical Density of The Composites

In some samples, such as AS6, TM4, TM5, and TM6, the effective density slightly exceeds the theoretical prediction, which may indicate tighter packing and reduced internal voids. Conversely, small negative deviations in certain PS samples can be attributed to entrapped air or incomplete filler consolidation during fabrication.

Overall, the density results confirm that increasing the metallic filler content enhances the compactness of the composite, while the dual-filler TM configuration provides the best structural homogeneity. Among all samples, TM6 stands out with the highest effective density and near-perfect agreement with theoretical values, verifying

its superior fabrication quality and supporting its later demonstrated excellence in radiation shielding performance.

Table 4.2 presents a comparative data of the density and radiation attenuation characteristics of PDMS, conventional lead, pure tin, and the fabricated tin–PDMS composite samples (AS5, AS6, TM5, and TM6). The data reflect the effect of the density of composites towards radiation parameters.

Pure PDMS exhibits the lowest density (1.103 g $cm^{-3}$), which corresponds to its limited radiation attenuation performance. Its low atomic number and polymeric nature make it effective only for low-energy photon scattering, providing minimal shielding against higher-energy radiation.

Table 4.2
Summary of Radiation Characteristics of PDMS, Conventional Lead, and Fabricated Samples

| **Samples** | **Density (g $cm^{-3}$)** | **Radiation attenuation characteristics** |
|---|---|---|
| PDMS | 1.103 | Low density; provides minimal attenuation, mainly for low-energy scatter. |
| Lead | 11.340 | Highest density; excellent attenuation for a broad range of photon energies. |
| Tin | 7.310 | Moderate–high density; good attenuation for medium-energy photons. |
| AS5 | 3.110 | Balanced density and structure; flexible composite shielding. |
| AS6 | 3.420 | Slightly higher density than AS5; improved attenuation while remaining flexible. |
| TM5 | 4.690 | Intermediate density; suitable for medium-level shielding applications. |
| TM6 | 5.320 | high-density metallic composite; suitable for flexible shielding applications. |

In contrast, pure tin and conventional lead, with densities of 7.31 g $cm^{-3}$ and 11.34 g $cm^{-3}$, respectively, demonstrate substantially greater attenuation capabilities. Tin provides moderate to high attenuation suitable for medium-energy photons, while lead remains the benchmark material for radiation shielding due to its very high density and broad-spectrum attenuation effectiveness. However, lead's brittleness, toxicity, and lack of flexibility make it less suitable for applications requiring lightweight or flexible materials.

Among the fabricated composites, AS5 and AS6 show promising improvements over pure PDMS. AS5, with a density of 3.11 g $cm^{-3}$, presents a good balance between structural flexibility and radiation attenuation, making it a viable lightweight shielding material. AS6, slightly denser at 3.42 g $cm^{-3}$, demonstrates improved attenuation

efficiency while retaining flexibility, suggesting that higher tin loading enhances radiation shielding without significantly compromising mechanical properties. TM5 and TM6 exhibit higher densities of 4.69 g $cm^{-3}$ and 5.32 g $cm^{-3}$, respectively. These samples are particularly effective for medium-level radiation shielding applications, where a trade-off between flexibility and attenuation performance is acceptable. Their intermediate densities indicate a well-integrated composite structure capable of absorbing more radiation compared to AS-series samples, yet still lighter and more manageable than pure metallic shields (Akhdar, 2025).

Overall, the data emphasise that the tin–PDMS composites bridge the gap between lightweight polymers and dense metallic materials. They offer a combination of density, flexibility, and shielding performance. Among the samples studied, AS6 and TM6 emerge as optimal candidates for flexible radiation protection applications, balancing attenuation efficiency with mechanical adaptability.

## 4.4 Morphology and Structural Analysis under Field Emission Scanning Electron Microscopy - Elemental Analysis with Energy Dispersive X-ray Spectroscopy

### 4.4.1 Field Emission Scanning Electron Microscopy under 100x magnification and 500x magnification

FESEM was conducted to examine the surface morphology and microstructural characteristics of the PDMS-based composites. This high-resolution imaging technique enables visualisation of surface features at both micro- and nanoscale levels, providing valuable information on particle dispersion, filler–matrix interaction, and morphological uniformity. FESEM analysis was conducted on the Control PDMS sample and its cross-section of all fabricated composites to assess the influence of filler incorporation on surface topology and structural integrity. The comparative examination of these images facilitates a detailed understanding of how filler type, morphology, and loading affect the microstructural evolution of the polymer matrix, thereby supporting correlations with elemental distribution through EDX and crystallinity through XRD analyses.

The FESEM images presented in Figure 4.6 depict the surface morphology of the Control PDMS sample at magnifications of 100x and 500x, providing a detailed understanding of the pristine polymer matrix before the introduction of metallic fillers. At the lower magnification (100x), the PDMS surface appears macroscopically smooth, continuous, and devoid of cracks, voids, or embedded particulates, signifying the intrinsic homogeneity and structural integrity of the pure, uncross-linked polymer. This featureless topology reflects the uniform polymer chain distribution characteristic of PDMS, which arises from its highly flexible siloxane backbone and low surface energy (Li et al., 2021).

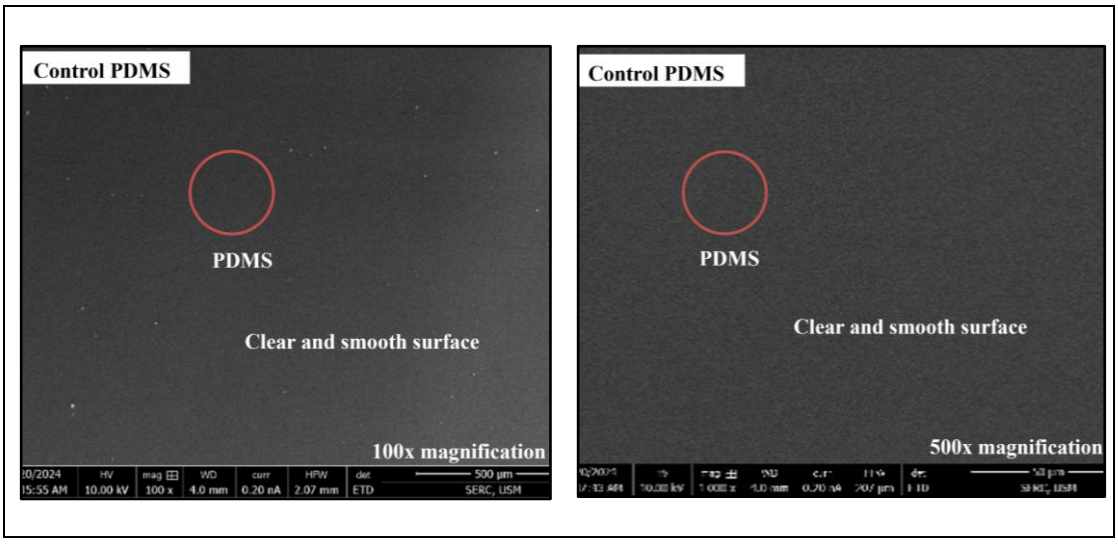


Figure 4.6 FESEM Images of Control PDMS at 100x Magnification and 500x Magnification

At a higher magnification of 500x, the surface remains largely smooth and homogeneous, though a fine microtexture becomes discernible. This subtle surface texture is uniformly distributed and lacks any evidence of agglomerates, microvoids, or phase separation, confirming the amorphous nature of PDMS and the absence of crystalline domains, in agreement with the XRD results.

Similar morphological behaviours of PDMS has been widely reported in literature, where FESEM images consistently reveal a smooth, nonporous surface indicative of amorphous polymer networks (Ding et al., 2021). The observed smoothness and lack of particulate matter reinforce that the PDMS matrix is structurally stable and free of foreign inclusions, validating its role as a control specimen for subsequent composite analysis.

This morphological uniformity establishes the Control PDMS as a benchmark sample for comparative evaluation with the PS, AS, and TM composites. Any deviations from this baseline, such as the appearance of discrete filler particles, roughened textures, or microstructural discontinuities, can be directly attributed to the incorporation of metallic fillers (Kaewpirom et al., 2022, (bualroos et al., 2024; Zainal Abidin, Mukhtar, Mahmood, Abdul Wahab, Zainon, Roslan, et al., 2025). Such comparative analysis is critical for understanding how filler morphology, dispersion, and loading influence the composite's microstructure, and by extension, its physical and mechanical properties, as further corroborated by EDX and XRD analyses.

#### *4.4.1.1 FESEM Analysis of PS Series*

The cross-sectional FESEM images in Figure 4.7 illustrate the morphological characteristics of the PS series at magnifications of 100x and 500x, across varying tin contents from PS1 (10 wt.%) to PS6 (60 wt.%). At 100x magnification, the composites display a distinct laminar configuration between the PDMS matrix and the embedded pure tin phase throughout the 0.25 cm-thick cross-section. The PDMS layer appears smooth, continuous, and free from visible cracks, voids, or delamination, signifying excellent structural cohesion. Embedded within the matrix, bright, irregularly shaped tin particles are observed, and their density and prominence increase progressively with higher tin content. This irregular morphology is characteristic of solidified pure tin domains, which naturally form angular or faceted structures rather than spherical particles (Gouda et al., 2023). The absence of particle agglomeration or clustering suggests effective dispersion of tin within the PDMS during composite preparation, and the strong interfacial bonding between phases indicates efficient physical adhesion and mechanical interlocking.

At 500x magnification, the FESEM images more clearly reveal the irregular morphology of pure tin particles embedded within the smooth PDMS phase. The tin–PDMS interfaces appear clean and well-defined, with no evidence of interfacial voids, peeling, or cracks, confirming excellent adhesion between the metal and polymer layers. The PDMS matrix fully encapsulates the tin particles, maintaining a continuous texture across the interface. This strong adhesion and uniform integration are consistent with prior studies on PDMS–metal composites, where PDMS flexibility and surface conformity promote intimate interfacial contact (Laysandra et al., 2025).

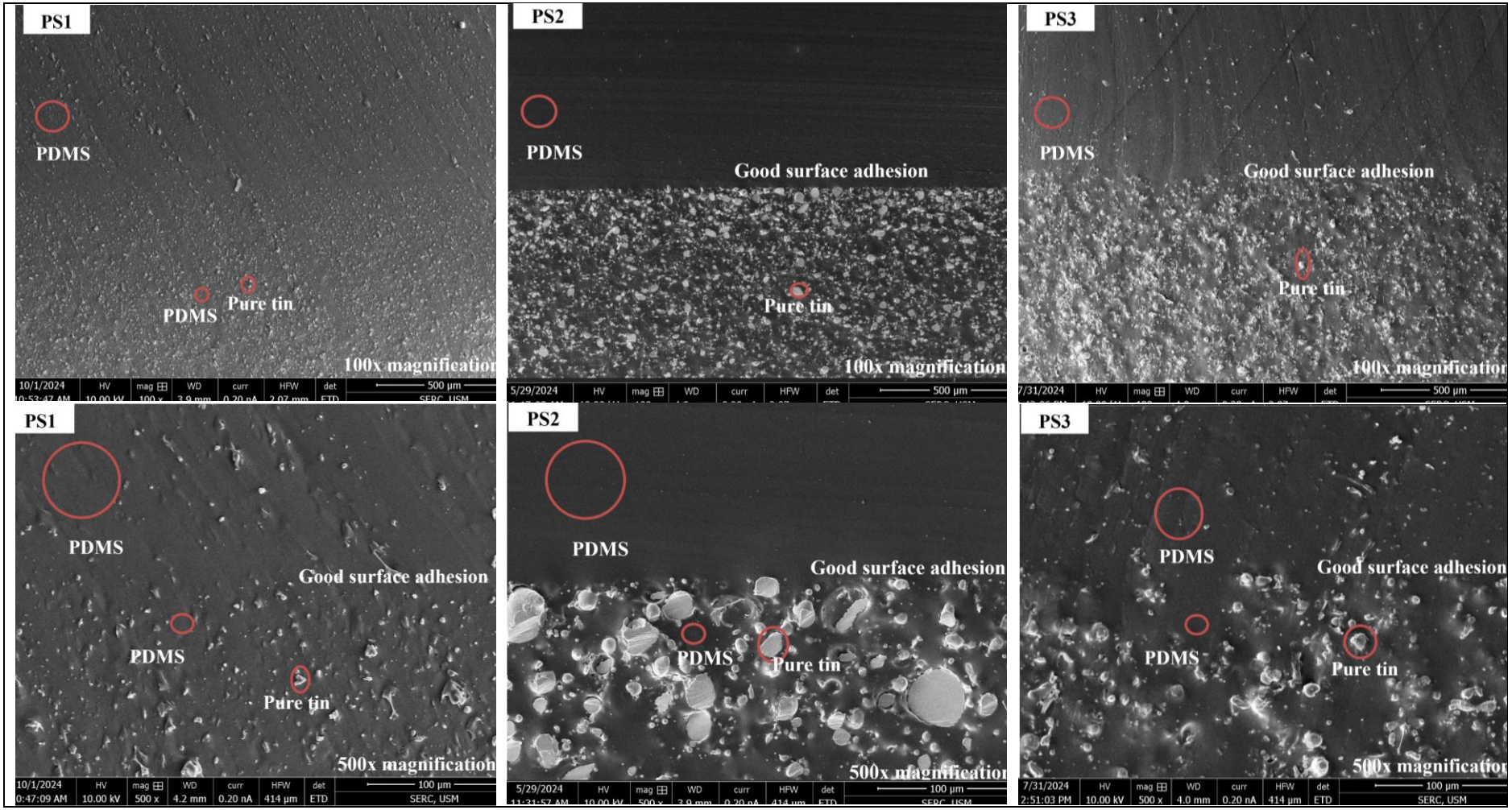
PS1
PDMS
PDMS
Pure tin
100x magnification
10/1/2024
HV
mag
WD
curr
HFW
det
500 µm
PS2
PDMS
Good surface adhesion
Pure tin
100x magnification
5/29/2024
HV
mag
WD
curr
HFW
det
500 µm
PS3
PDMS
Good surface adhesion
Pure tin
100x magnification
7/31/2024
HV
mag
WD
curr
HFW
det
500 µm
PS1
PDMS
Good surface adhesion
PDMS
Pure tin
500x magnification
10/1/2024
0:47:09 AM
HV
10.00 kV
mag
500 x
WD
4.2 mm
curr
0.20 nA
HFW
414 µm
det
ETD
100 µm
SERC, USM
PS2
PDMS
Good surface adhesion
PDMS
Pure tin
500x magnification
5/29/2024
HV
10.00 kV
mag
500 x
WD
curr
0.20 nA
HFW
414 µm
det
ETD
100 µm
SERC, USM
PS3
PDMS
Good surface adhesion
PDMS
Pure tin
500x magnification
7/31/2024
2:51:03 PM
HV
10.00 kV
mag
500 x
WD
4.0 mm
curr
0.20 nA
HFW
414 µm
det
ETD
100 µm
SERC, USM

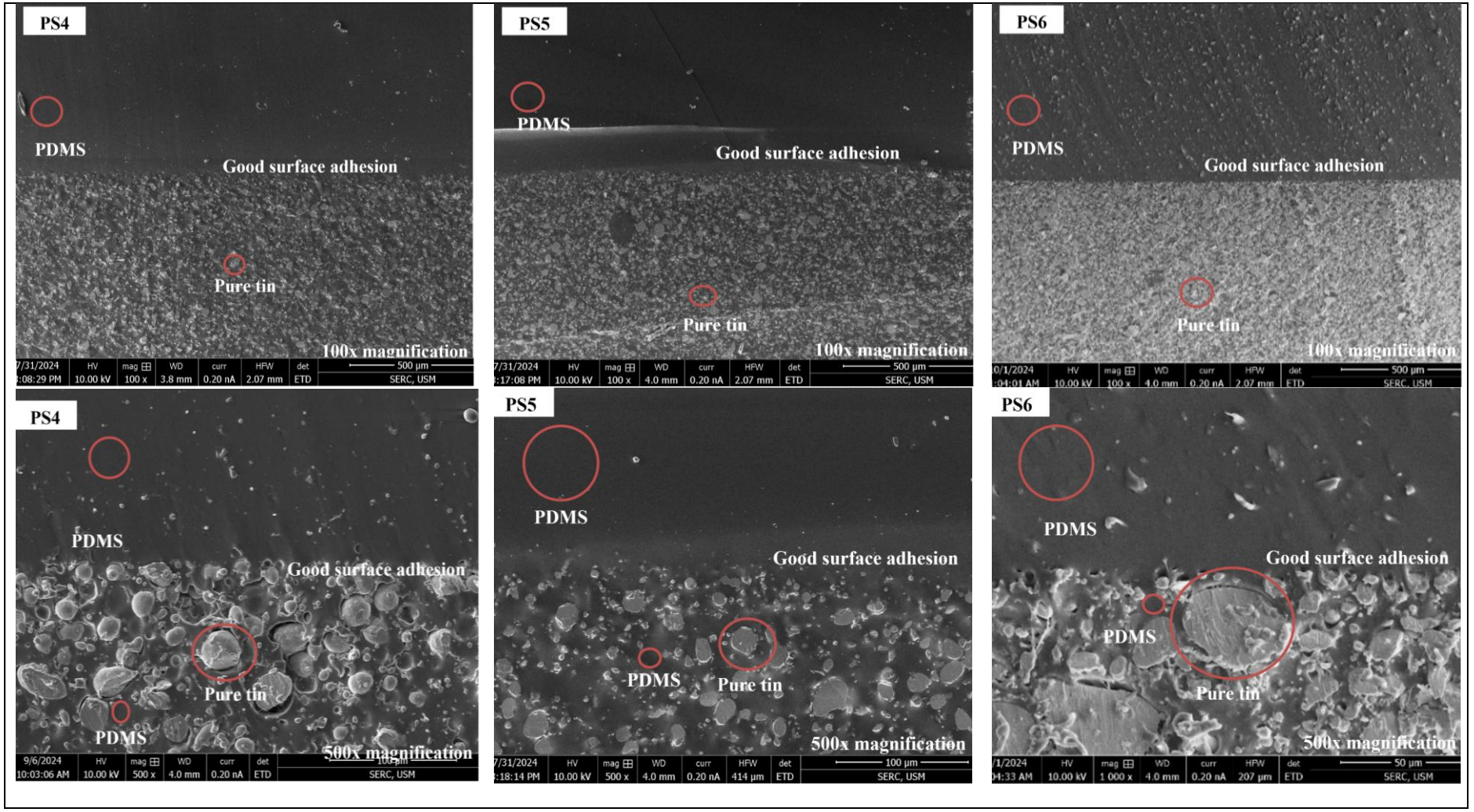


Figure 4.7 FESEM Images of The PS Series at 100x Magnification and 500x Magnification of PS1, PS2, PS3, PS4, PS5, and PS6

The microstructure remains compact and homogeneous even at higher filler concentrations, reflecting both effective mixing and stable curing behaviours during composite fabrication. A progressive trend is observed across the PS series as the tin loading increases. At low concentrations (PS1 and PS2), only a few small irregular tin particles are visible within the PDMS matrix, whereas PS3 and PS4 exhibit a moderate increase in particle density while maintaining uniform dispersion and strong adhesion.

In the higher-loaded composites (PS5 and PS6), the tin phase becomes significantly more visible, forming a dense metallic framework within the polymer matrix. The FESEM images confirm that, despite this high tin content, the overall structure remains cohesive, with no agglomeration or delamination observed. The clear laminar interface and dense packing of irregular tin particles within the PDMS phase provide a robust microstructural foundation for mechanical and functional performance. The observations summarised above demonstrate a controlled microstructural evolution across the PS series. At low tin concentrations, the composites exhibit a smooth PDMS phase with sparsely distributed tin inclusions and excellent adhesion. As tin content increases, more irregular tin particles become visible and densely packed, yet maintain homogeneous dispersion and strong interface bonding. The absence of voids, peeling, or cracks across all samples confirms the cohesive nature of the PDMS-tin interface.

This indicates that the irregular morphology of pure tin facilitates mechanical interlocking within the elastomer matrix, further enhancing adhesion and structural stability (Putz et al., 2023). The high-density irregular tin regions observed in PS5–PS6 contribute significantly to radiation attenuation performance. The greater atomic density and irregular geometry of pure tin particles increase photon scattering paths and absorption probability, resulting in improved shielding efficiency (Hussain et al., 2011). The PDMS layer complements this by reducing radiation backscattering and providing elastic energy dissipation, ensuring that the absorbed energy is uniformly distributed within the composite (AbuAlRoos et al., 2019). This combination of irregular metallic inclusions and flexible polymer confinement results in a balanced structure with high radiation absorption and excellent mechanical resilience.

Overall, the FESEM results confirm that the PS series possesses a homogeneous, well-bonded, and defect-free cross-sectional morphology across all tin loadings. The irregularly shaped tin particles are effectively encapsulated within the PDMS matrix, maintaining structural cohesion and laminar uniformity. The observed microstructure directly supports enhanced radiation-shielding performance, validating

the PS series as a robust and flexible material system suitable for protective and electronic applications (Ahmed et al., 2020; Gouda et al., 2023).

#### *4.4.1.2 FESEM Analysis of AS Series*

In the AS series, the FESEM micrographs at 100x magnification (Figure 4.8) reveal a noticeably denser and more compact microstructure compared to the PS series. Even at lower filler concentrations (AS1 – AS2), the spherical tin alloy particles are clearly discernible and appear to be uniformly dispersed within the PDMS matrix. This uniform dispersion can be attributed to the relatively high wettability and interfacial compatibility between the alloy surface and the silicone-based polymer chains, which reduces surface tension and inhibits early-stage agglomeration during mixing and curing (More et al., 2021). As the filler content increases (AS5 – AS6), the particle packing becomes increasingly dense, resulting in the formation of a more interconnected filler network. This network structure is significant as it enhances both the mechanical stiffness and the probability of photon–electron interactions, thereby improving the material's overall radiation attenuation capability (Alanazi et al., 2024).

At a magnification of 500x, the interfacial morphology between the PDMS matrix and the tin alloy fillers appear homogenous, with fewer interfacial voids and microcracks compared to the PS series containing pure tin particles. The spherical morphology of the alloy fillers facilitates close packing and effective stress transfer across the filler–matrix interface, resulting in a smoother boundary and reduced defect density (S. Chen et al., 2025). This improvement in interfacial bonding can be explained by the alloy's enhanced surface energy balance and its ability to undergo limited surface oxidation, which promotes better adhesion to the siloxane groups in PDMS. Consequently, the composite exhibits strong filler–matrix adhesion with minimal particle detachment or interfacial delamination, even at higher filler loadings (AS6).

While slight agglomeration is observed in AS6, the degree of clustering remains minimal and does not disrupt the continuity of the filler network. The observed stratification within the composite, where denser tin alloy particles accumulate toward the bottom region, is consistent with the density gradient effect during room-temperature curing. This gravitational segregation is typical in metal–polymer composites with a significant density contrast between the filler and matrix (Samal, 2020).

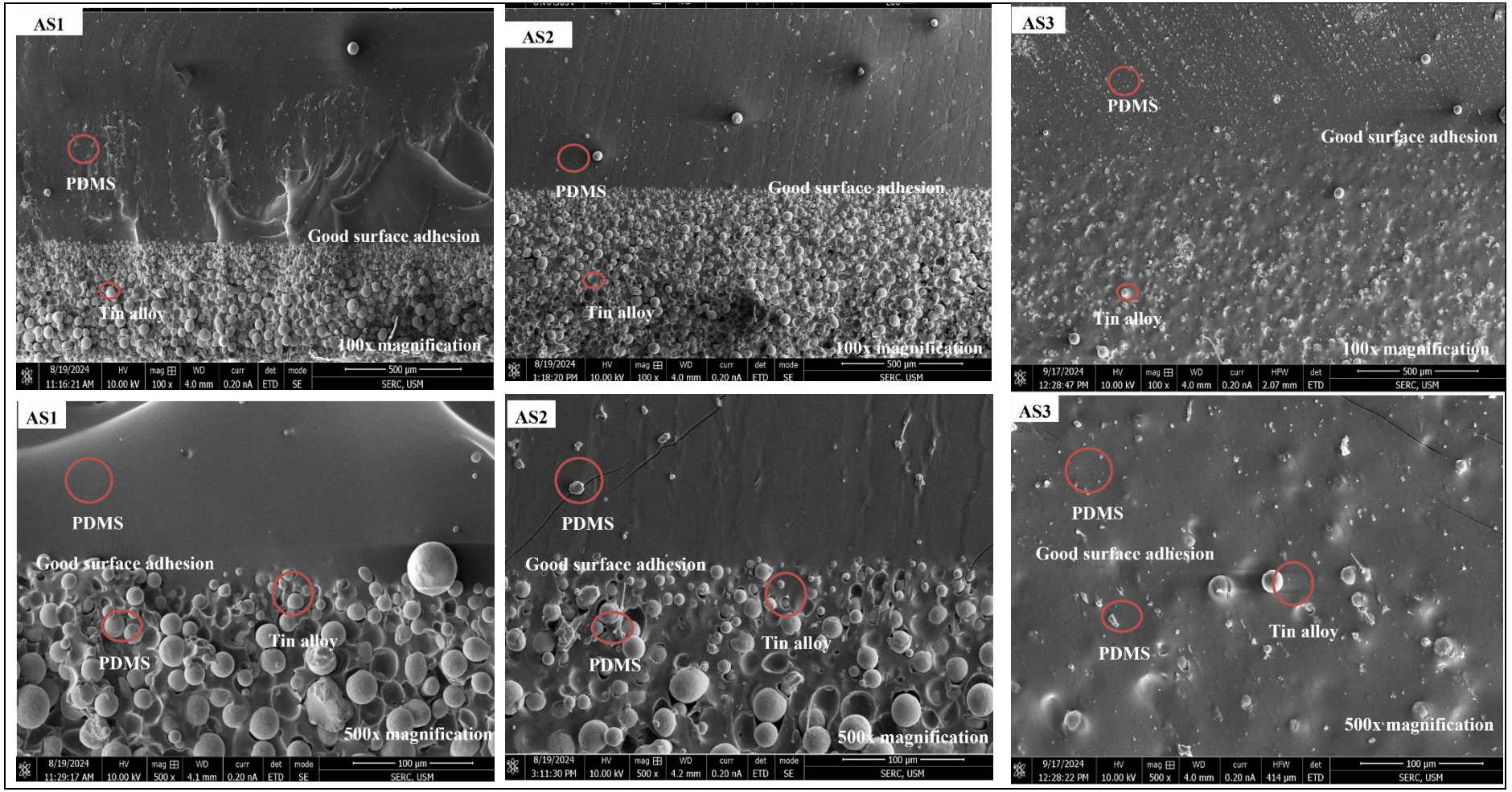
AS1
PDMS
Good surface adhesion
Tin alloy
100x magnification
8/19/2024 11:16:21 AM HV 10.00 kV mag 100 x WD 4.0 mm curr 0.20 nA det ETD mode SE 500 µm SERC, USM
AS2
PDMS
Good surface adhesion
Tin alloy
100x magnification
8/19/2024 1:18:20 PM HV 10.00 kV mag 100 x WD 4.0 mm curr 0.20 nA det ETD mode SE 500 µm SERC, USM
AS3
PDMS
Good surface adhesion
Tin alloy
100x magnification
9/17/2024 12:28:47 PM HV 10.00 kV mag 100 x WD 4.0 mm curr 0.20 nA HFW 2.07 mm det ETD 500 µm SERC, USM
AS1
PDMS
Good surface adhesion
Tin alloy
PDMS
500x magnification
8/19/2024 11:29:17 AM HV 10.00 kV mag 500 x WD 4.1 mm curr 0.20 nA det ETD mode SE 100 µm SERC, USM
AS2
PDMS
Good surface adhesion
Tin alloy
PDMS
500x magnification
8/19/2024 3:11:30 PM HV 10.00 kV mag 500 x WD 4.2 mm curr 0.20 nA det ETD mode SE 100 µm SERC, USM
AS3
PDMS
Good surface adhesion
Tin alloy
PDMS
500x magnification
9/17/2024 12:28:22 PM HV 10.00 kV mag 500 x WD 4.0 mm curr 0.20 nA HFW 414 µm det ETD 100 µm SERC, USM

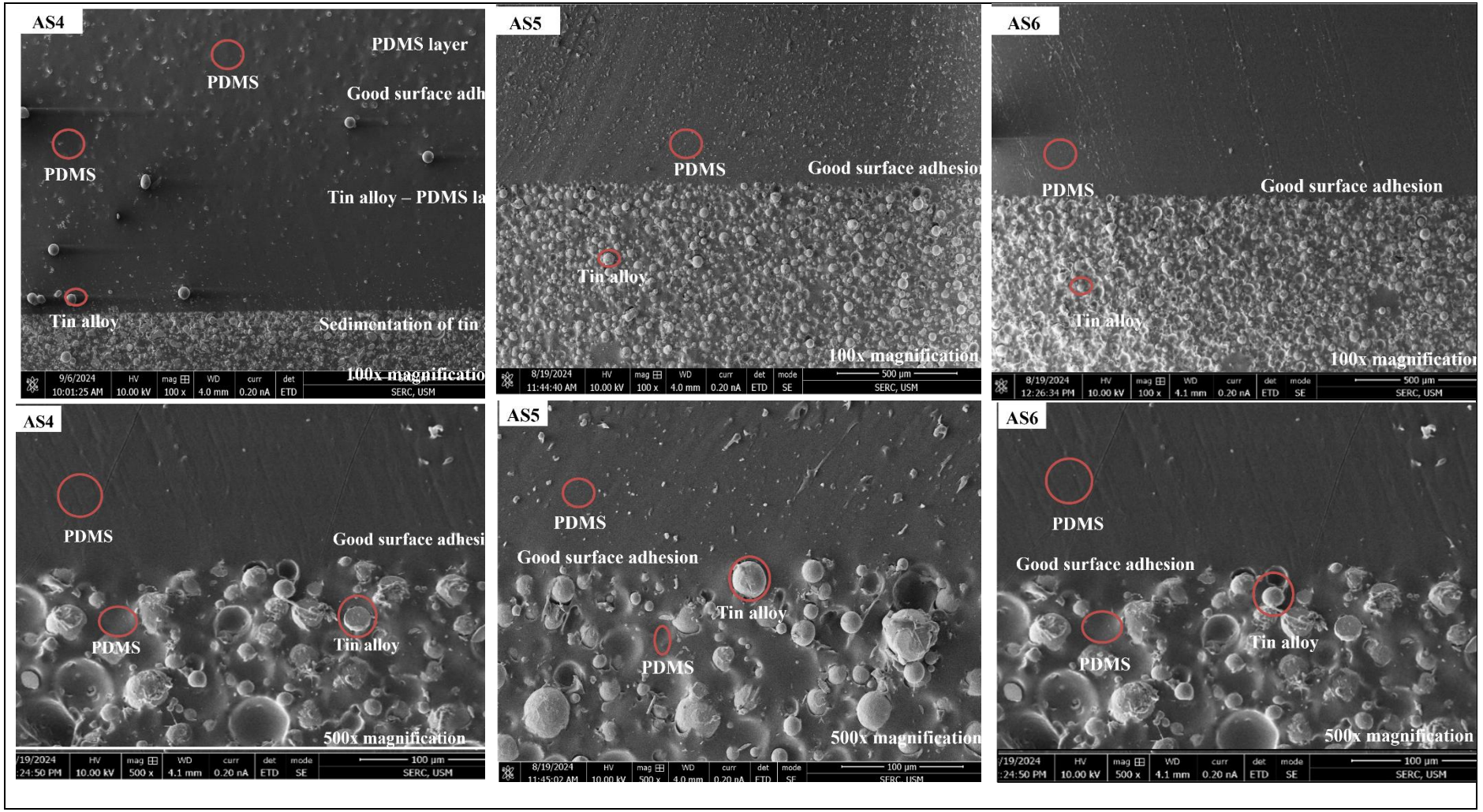


Figure 4.8 FESEM Images of The AS Series at 100x Magnification and 500x Magnification of AS1, AS2, AS3, AS4, AS5, and AS6

However, in the AS series, the gradual transition between the PDMS-rich upper layer and the filler-rich lower layer maintains structural continuity, preventing void formation or delamination across the interface. This indicates strong adhesion and high cohesive energy between layers, ensuring that the overall radiation shielding performance remains unaffected despite the slight compositional gradient. In summary, the AS series demonstrates superior filler dispersion, improved particle–matrix interfacial bonding, and a stable layer architecture compared to the PS series. From a radiation shielding perspective, the microstructural observations of the AS series composites provide strong evidence that filler morphology and dispersion directly influence photon attenuation behavior. The formation of a continuous tin alloy network within the PDMS matrix establishes multiple interfaces that enhance the probability of photon–electron interactions, thereby increasing energy absorption efficiency (Vashishtha et al., 2025). The higher atomic number and density of the tin alloy facilitate photoelectric absorption and Compton scattering, while the PDMS phase acts as a low-density moderator that reduces the scattering intensity of secondary radiation (Yazdankish, 2024).

Furthermore, the spherical morphology of the alloy fillers enhances isotropic packing, which contributes to uniform stress distribution under thermal and mechanical loads. This isotropic behavior minimises microcrack initiation and prevents filler detachment during radiation exposure or mechanical deformation (Samal & Blanco, 2021a). The FESEM results thus correlate with the superior adhesion and mechanical resilience observed in macroscopic tests, where composites with spherical and well-bonded fillers typically exhibit enhanced durability and stable shielding coefficients (Samal & Blanco, 2021a).

Interestingly, the gravitational settling of dense tin alloy particles during curing forms a subtle compositional gradient, creating a bottom-heavy microstructure with an alloy-rich lower zone. This arrangement, while initially a by-product of density differences, may actually benefit radiation protection by positioning the high-density materials nearer to the direction of incident radiation, thereby maximising primary photon absorption (Nakamura et al., 2024b). Consequently, the PDMS-rich upper layer acts as a secondary barrier, effectively attenuating scattered photons and contributing to the composite's dual-layer shielding mechanism .

In short, the AS series composites exhibit an optimised microstructural architecture where the spherical alloy fillers enhance interfacial bonding, structural

uniformity, and photon attenuation. The synergistic effects of filler density, morphology, and dispersion result in a composite that balances flexibility and shielding capacity, demonstrating that microstructural control is a critical design parameter for advanced PDMS-based radiation shielding materials (Samal, 2020; Tian et al., 2025; Yazdankish, 2024).

#### *4.4.1.3 FESEM Analysis of TM Series*

In the TM series, the FESEM micrographs at 100x magnification (Figure 4.9) reveal a distinctly heterogeneous surface morphology characterised by the coexistence of spherical tin alloy particles and irregular pure tin fillers. At lower loadings (TM1 – TM3), both filler types are uniformly distributed within the PDMS matrix, though minor separation zones suggest slight differences in surface energy and wetting behaviours between the two filler morphologies. As the filler concentration increases (TM5 – TM6), particle overlap becomes more pronounced, leading to partial layering and a denser filler network. This hybridised configuration forms an intricate composite microstructure that balances the flowability of the spherical alloy particles with the interlocking rigidity of the irregular tin fillers, resulting in improved filler packing and overall density (R. Wang et al., 2018).

At a magnification of 500x, the dual-filler interaction becomes more evident. The spherical alloy particles promote enhanced interfacial contact with the PDMS matrix due to their low aspect ratio and smooth surface, enabling improved wetting and polymer infiltration around the filler boundaries. Conversely, the irregular tin fillers contribute to localised surface roughness, which enhances mechanical interlocking and density but may also induce minor stress concentrations within the polymer network (Lunsford & Contoyannis, 2019). Although limited agglomeration and partial particle detachment are observed at higher loadings (TM6), the interfacial adhesion remains superior to that of the PS series, indicating that the presence of alloy fillers improves the overall matrix compatibility.

This hybrid filler configuration offers several functional advantages. The spherical alloy particles act as lubricating nodes that enhance dispersion and reduce interparticle friction during curing, while the irregular tin fillers occupy void regions, thereby increasing packing efficiency and effective density (R. Wang et al., 2018). As a result, the TM composites display improved continuity of the filler network,

facilitating the formation of more effective radiation attenuation pathways. The high atomic number of both copper and tin provides dual-mode attenuation via photoelectric and Compton scattering processes, while the PDMS matrix contributes to backscattered radiation moderation.

Furthermore, the observed layered structure at higher filler loadings may stem from the differential sedimentation of tin and alloy particles during room-temperature curing, as denser fillers migrate downward under gravitational influence (R. Wang et al., 2018). This stratified architecture, however, is hypothesised to reinforce shielding efficiency by creating a graded density profile where high-density filler concentration near the lower region enhances radiation absorption, and the PDMS layer reduces secondary photon scattering. Overall, the TM series demonstrates that combining fillers of distinct morphology and density can yield synergistic effects in composite performance.

The spherical tin alloy particles improve interfacial bonding and dispersion, while the irregular tin fillers contribute mass density and mechanical strength. This morphological synergy underpins the TM composites' superior radiation shielding performance, structural integrity, and interfacial stability compared to single-filler composite (Samal & Blanco, 2021a; Vashishtha et al., 2025; Zainal Abidin, Mukhtar, Mahmood, Abdul Wahab, Zainon, Roslan, et al., 2025). From a mechanistic standpoint, the superior shielding behaviours of the TM composites can be attributed to the synergistic interaction between the tin alloy and pure tin fillers. The combination of spherical and irregular morphologies results in a hierarchical microstructure that optimises both electronic and physical attenuation pathways. This allows for more effective absorption of low-energy photons via the photoelectric effect, while maintaining minimal voids and reduced backscattering (Nagaraja et al., 2020). In contrast, the irregular tin particles, with their sharper geometrical edges, act as high-density scattering centres, contributing to secondary attenuation through Compton scattering mechanisms (Avcıoğlu, 2025). Such a configuration mirrors engineered multilayer radiation barriers, where optimised filler distribution leads to enhanced linear attenuation coefficients without compromising material flexibility (Dikra et al., 2024b).

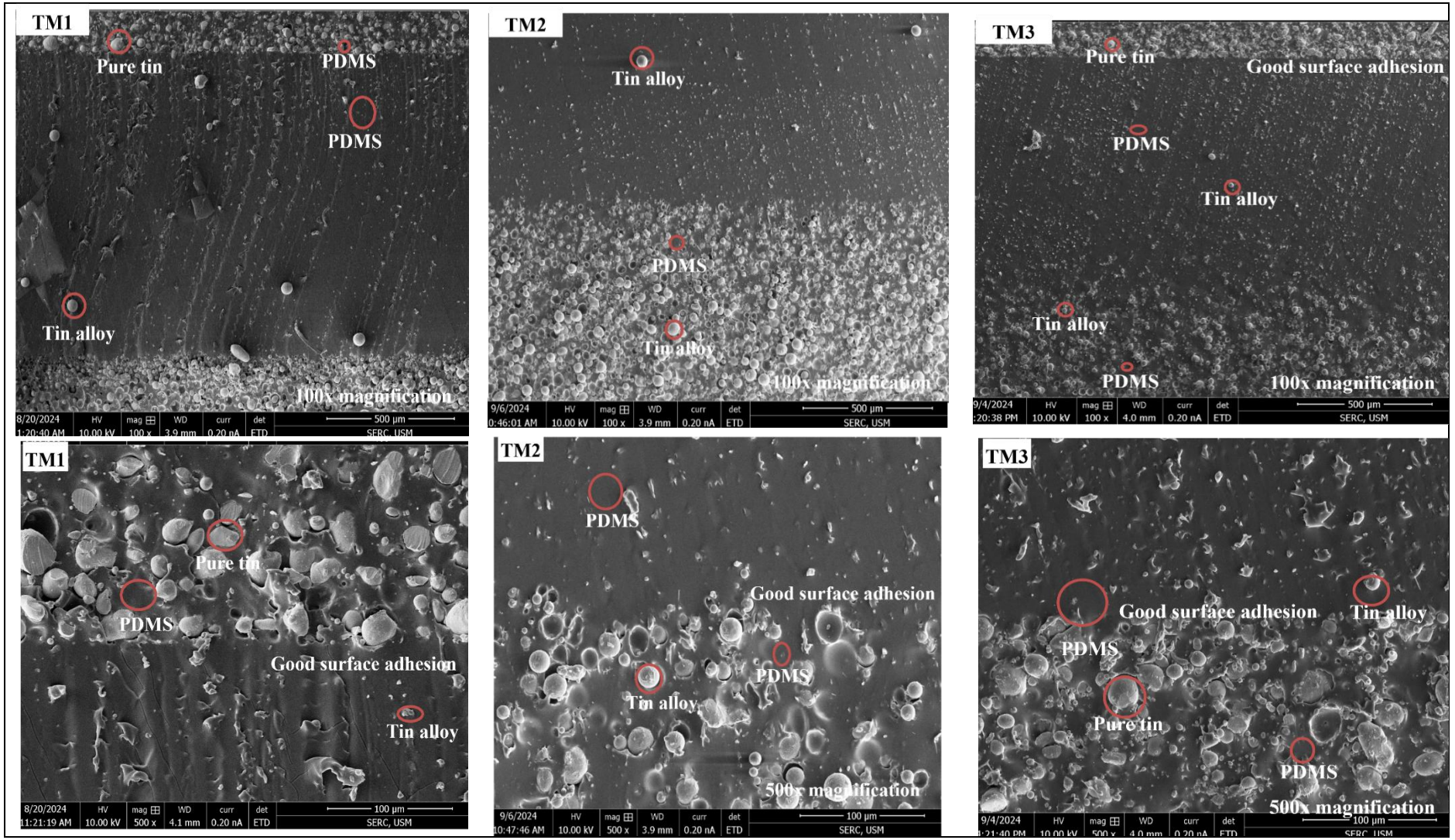
TM1
Pure tin
PDMS
PDMS
Tin alloy
100x magnification
8/20/2024 HV mag WD curr det 500 µm
10.00 kV 100 x 3.9 mm 0.20 nA ETD SERC, USM
TM2
Tin alloy
PDMS
Tin alloy
100x magnification
9/6/2024 HV mag WD curr det 500 µm
0:46:01 AM 10.00 kV 100 x 3.9 mm 0.20 nA ETD SERC, USM
TM3
Pure tin
Good surface adhesion
PDMS
Tin alloy
Tin alloy
PDMS
100x magnification
9/4/2024 HV mag WD curr det 500 µm
:20:38 PM 10.00 kV 100 x 4.0 mm 0.20 nA ETD SERC, USM
TM1
Pure tin
PDMS
Good surface adhesion
Tin alloy
8/20/2024 HV mag WD curr det 100 µm
11:21:19 AM 10.00 kV 500 x 4.1 mm 0.20 nA ETD SERC, USM
TM2
PDMS
Good surface adhesion
PDMS
Tin alloy
500x magnification
9/6/2024 HV mag WD curr det 100 µm
10:47:46 AM 10.00 kV 500 x 3.9 mm 0.20 nA ETD SERC, USM
TM3
Good surface adhesion
Tin alloy
PDMS
Pure tin
PDMS
500x magnification
9/4/2024 HV mag WD curr det 100 µm
10.00 kV 500 x 4.0 mm 0.20 nA ETD SERC, USM

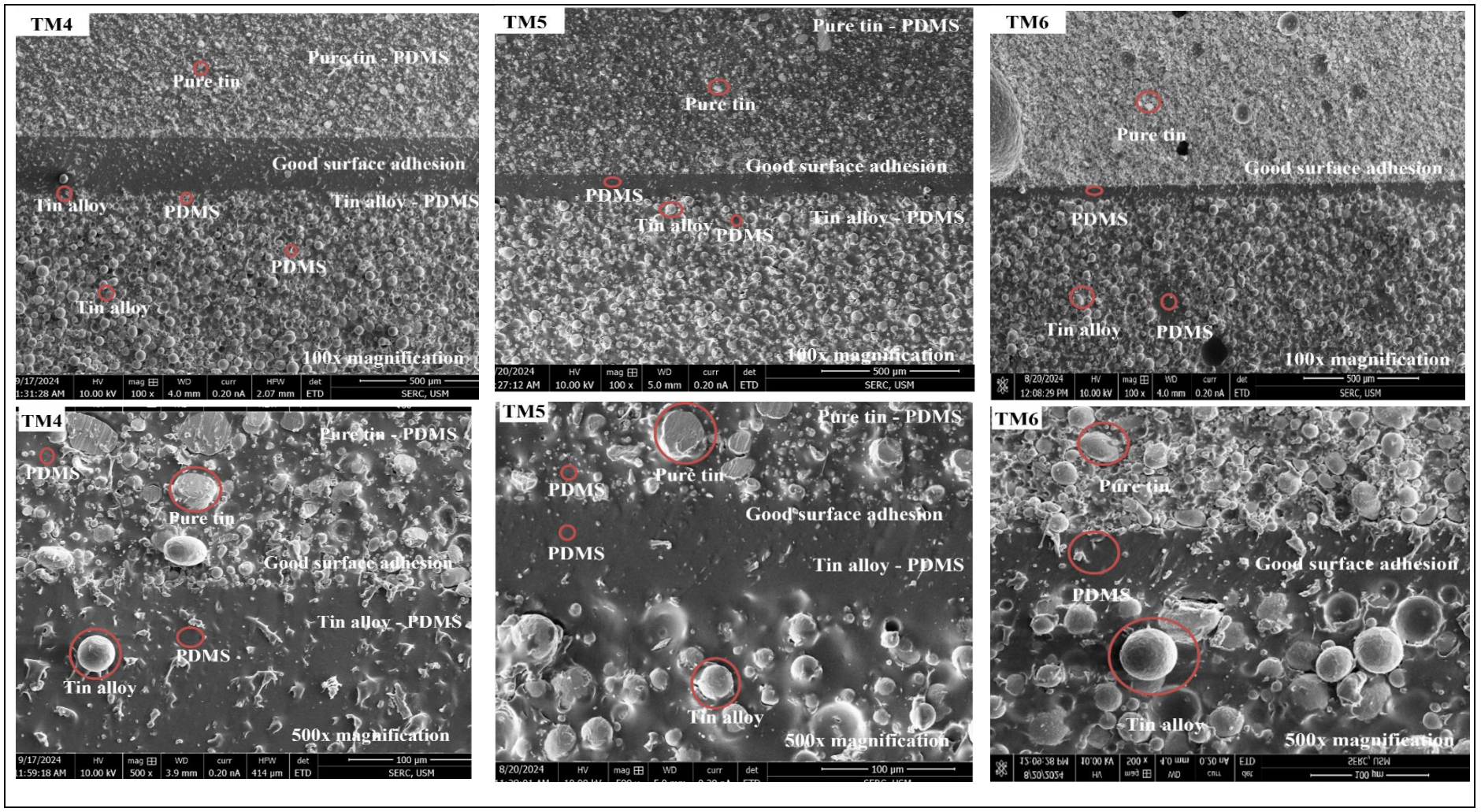


Figure 4.9 FESEM Images of The TM Series at 100x Magnification and 500x Magnification of TM1, TM2, TM3, TM4, TM5, and TM6

As a summary, the FESEM investigation provided comprehensive insights into the surface and cross-sectional morphologies of the PDMS-based composites and established clear correlations between filler type, morphology, dispersion behaviours, and interfacial integrity. The Control PDMS exhibited a smooth, defect-free surface with uniform microtexture and no particulate features, confirming the homogeneity of the pure polymer matrix. This baseline morphology served as a crucial reference point for assessing the effects of metallic filler incorporation on composite microstructure.

### 4.4.2 Elemental Analysis with Energy Dispersive X-ray Spectroscopy (EDX) Analysis

#### *4.4.2.1 Elemental Analysis of Weight Percentage*

To complement the FESEM observations, EDX analysis was conducted at a magnification of 2kx on all samples: control PDMS, PS series, AS series, and TM series, tabulated in Table 4.3 to determine their elemental composition. Across all samples, the predominant elements detected were tin, silicon, carbon, oxygen, and copper. The presence of copper in the AS and TM series is attributed to the tin alloy incorporated in these materials. In contrast, the trace amount observed in the PS series is likely due to minor compositional impurities. Across all samples, carbon, oxygen, silicon, copper, and tin are consistently detected, corresponding to the PDMS matrix and the incorporated tin-based alloy fillers.

For the PS series, a general increase in tin content is observed as the sample sequence progresses from PS1 to PS6, indicating successful incorporation of the metallic filler within the PDMS matrix. Tin content increases from 9.48 wt.% in PS1 to 30.11 wt.% in PS4 and remains relatively high in PS6 (29.54 wt.%). This overall trend confirms that increasing filler loading enhances the probability of tin exposure at the analysed surface (Adeniyi & Ighalo, 2021). Concurrently, carbon and silicon contents tend to decrease, reflecting partial replacement of the polymer phase by the denser metal filler. Oxygen remains within the range of 11.27–26.57 wt.%, which is consistent with the inherent Si–O–Si backbone of PDMS and the possible presence of surface oxides on the metallic particles (Sharma & Bose, 2021). Despite the overall increasing trend, certain PS samples exhibit non-monotonic variations, such as the lower tin content in PS3 (16.40 wt.%) compared to PS2 (22.93 wt.%). These fluctuations can be attributed

to the spot-based nature of EDX analysis, where the detected composition depends on the local region selected for measurement. In heterogeneous polymer–metal composites, metallic particles may be unevenly distributed or partially embedded beneath the polymer surface. As a result, an EDX spot may intersect a polymer-rich region with reduced metal exposure, leading to lower apparent tin content even when the overall filler loading is higher. Therefore, these variations do not indicate poor filler incorporation but rather reflect local compositional heterogeneity (Samal & Blanco, 2021b).

In the AS series, tin content remains relatively low across most samples, typically below 3 wt.%, except for AS4, which exhibits a higher tin value of 14.59 wt.%. The elemental profile of the AS series is dominated by carbon (20.77 to 25.27 wt.%), oxygen (21.36 to 22.74 wt.%), and silicon (26.82 to 34.59 wt.%), indicating that the PDMS matrix predominantly occupies the analysed surface (Peng et al., 2021). Copper, however, is consistently detected at appreciable levels (15.91 to 23.15 wt.%), confirming the presence of the tin alloy filler. The low tin signal in most AS samples is likely due to alloy particles being partially encapsulated within the polymer matrix rather than exposed at the surface. Since EDX probes only a shallow interaction volume, metallic particles located beneath the polymer surface may not be effectively detected. The elevated tin content in AS4 suggests that the analysed spot coincided with a region where alloy particles were more exposed, further highlighting the influence of local surface morphology on EDX results (Zou et al., 2021).

Table 4.3
EDX Weight Percentage

| | **Element by weight percentage (wt.%)** | | | | |
|---|---|---|---|---|---|
| **Sample Label** | **Carbon** | **Oxygen** | **Silicon** | **Copper** | **Tin** |
| PS1 | 19.55 | 19.18 | 33.42 | 18.37 | 9.48 |
| PS2 | 17.29 | 26.57 | 29.81 | 3.41 | 22.93 |
| PS3 | 14.48 | 16.60 | 34.48 | 18.05 | 16.40 |
| PS4 | 9.76 | 11.27 | 27.93 | 20.94 | 30.11 |
| PS5 | 18.67 | 25.58 | 25.26 | 9.42 | 21.08 |
| PS6 | 13.69 | 20.54 | 24.02 | 12.23 | 29.54 |
| AS1 | 24.96 | 22.07 | 27.26 | 23.15 | 2.58 |
| AS2 | 25.27 | 21.48 | 28.73 | 22.53 | 2.01 |
| AS3 | 24.20 | 21.36 | 34.59 | 18.50 | 1.37 |
| AS4 | 20.77 | 21.92 | 26.82 | 15.91 | 14.59 |
| AS5 | 24.63 | 22.22 | 28.65 | 21.96 | 2.54 |

| | | | | | |
|---|---|---|---|---|---|
| AS6 | 24.44 | 22.74 | 29.81 | 20.65 | 2.39 |
| TM1 | 20.68 | 22.88 | 24.77 | 14.81 | 16.87 |
| TM2 | 20.32 | 23.70 | 26.20 | 15.54 | 14.25 |
| TM3 | 18.35 | 21.24 | 26.98 | 19.72 | 13.72 |
| TM4 | 20.27 | 21.80 | 29.20 | 17.94 | 10.80 |
| TM5 | 23.47 | 21.44 | 34.45 | 19.57 | 1.09 |
| TM6 | 17.51 | 23.13 | 24.26 | 13.30 | 21.81 |

The TM series exhibits moderate to high tin contents ranging from 1.09 wt.% in TM5 to 21.81 wt.% in TM6, accompanied by relatively stable copper concentrations. Most TM samples show balanced contributions from carbon, oxygen, and silicon, indicating that the PDMS network remains continuous while accommodating the metallic filler. The notably low tin content observed in TM5 can again be explained by the spot characterisation nature of EDX, where the selected region may have been dominated by polymer or silicon-rich phases, masking the underlying metal particles. Nevertheless, when considered collectively, the TM series demonstrates a more uniform elemental distribution compared to the PS and AS series, suggesting improved filler dispersion and reduced segregation.

Overall, while each sample occasionally displays lower tin weight percentages than expected, these variations are inherent to localised EDX measurements and do not undermine the general compositional trends. The EDX results should therefore be interpreted as representative surface compositions rather than absolute bulk values. When viewed across multiple samples and series, the data clearly confirm successful incorporation of tin-based alloy fillers, with compositional differences governed by filler loading, dispersion quality, and surface exposure. These findings are consistent with the heterogeneous nature of polymer–metal composites and align well with the morphological features observed in FESEM analysis.

#### *4.4.2.2 Elemental Analysis of Atomic Percentage*

The atomic percentage (at.%) analysis provides further insight into the elemental distribution within the composites, complementing the weight percentage results. Unlike weight percentage, atomic percentage is more sensitive to lighter elements such as carbon and oxygen, and therefore provides valuable insight into surface chemistry, elemental distribution, and potential interfacial interactions within

the polymer–metal composites (Torres-Rivero et al., 2021). Table 4.4 presents the elemental composition of the PS, AS, and TM sample series expressed in atomic percentage, which reflects the relative number of atoms present at the analysed surface region.

In the PS series, carbon and oxygen collectively dominate the atomic composition, reflecting the PDMS-based matrix, which consists primarily of Si–O–Si linkages with organic methyl groups (Nguyen et al., 2024). A gradual reduction in carbon atomic percentage is observed from PS1 (37.57 at.%) to PS4 (26.23 at.%), indicating increasing surface coverage by metallic fillers as the sample sequence progresses. Silicon remains relatively stable between 23.00 and 31.80 at.%, confirming the persistence of the PDMS network even at higher filler contents (Torres-Rivero et al., 2021). Copper and tin atomic percentages increase from PS1 to PS4, with tin rising from 1.26 at.% to 8.32 at.%, demonstrating improved exposure of metallic particles at the surface. Minor deviations in this trend, such as the lower tin atomic percentage in PS3 compared to PS2, can be attributed to localised heterogeneity and uneven filler dispersion. Given that EDX probes only a limited interaction volume, the selected analysis spot may coincide with polymer-rich regions, resulting in lower detected metal content despite increased overall filler loading.

The AS series is characterised by consistently high carbon atomic percentages exceeding 38 at.% across all samples, indicating that the polymer matrix dominates the analysed surface. Oxygen content remains within 27.34 to 31.35 at.%, consistent with the siloxane backbone and surface oxidation effects. Silicon is present at moderate levels (20.16 to 25.23 at.%), confirming the stability of the PDMS framework (Nguyen et al., 2024).

Copper atomic percentage remains relatively uniform between 5.57 and 7.57 at.%, confirming the presence of the tin alloy filler. However, tin atomic percentages are notably low, typically below 0.5 at.% for most AS samples, with the exception of AS4 (3.10 at.%). This low tin signal is attributed to alloy particles being partially embedded beneath the polymer surface, thereby limiting their direct exposure within the EDX interaction volume. The elevated tin value in AS4 suggests that the analysed spot intersected a region with greater metallic exposure, reinforcing the spot-dependent nature of EDX measurements.

Table 4.4
EDX Atomic Percentage

| Sample Label | Elements by atomic percentage (at.%) | | | | |
|---|---|---|---|---|---|
| | Carbon | Oxygen | Silicon | Copper | Tin |
| PS1 | 37.57 | 25.72 | 28.73 | 6.72 | 1.26 |
| PS2 | 32.38 | 37.79 | 24.12 | 1.24 | 4.48 |
| PS3 | 30.94 | 25.84 | 31.80 | 7.81 | 3.63 |
| PS4 | 26.23 | 23.00 | 31.79 | 10.67 | 8.32 |
| PS5 | 26.68 | 34.05 | 24.57 | 6.03 | 8.67 |
| PS6 | 30.63 | 34.51 | 23.00 | 5.18 | 6.70 |
| AS1 | 43.17 | 28.65 | 20.16 | 7.57 | 0.45 |
| AS2 | 43.47 | 27.73 | 21.14 | 7.33 | 0.35 |
| AS3 | 41.25 | 27.34 | 25.23 | 5.96 | 0.24 |
| AS4 | 38.34 | 31.35 | 21.65 | 5.57 | 3.10 |
| AS5 | 42.48 | 28.75 | 21.14 | 7.21 | 0.45 |
| AS6 | 41.83 | 29.22 | 21.81 | 6.74 | 0.42 |
| TM1 | 38.37 | 33.06 | 19.94 | 5.05 | 3.59 |
| TM2 | 37.59 | 33.42 | 20.86 | 5.32 | 2.83 |
| TM3 | 35.80 | 31.50 | 22.70 | 7.18 | 2.82 |
| TM4 | 37.78 | 30.61 | 23.26 | 6.28 | 2.07 |
| TM5 | 40.40 | 27.70 | 25.34 | 6.38 | 0.19 |
| TM6 | 34.93 | 34.70 | 20.87 | 5.05 | 4.45 |

In the TM series, carbon and oxygen remain the dominant elements, with carbon ranging from 34.93 to 40.40 at.% and oxygen from 27.70 to 34.70 at.%. These values indicate a balanced organic–oxide surface environment. Silicon content remains relatively stable between 19.94 and 25.34 at.%, suggesting that the PDMS network remains intact across the series. Copper atomic percentages vary modestly from 5.05 to 7.18 at.%, indicating consistent alloy presence. Tin atomic percentages range from as low as 0.19 at.% in TM5 to 4.45 at.% in TM6. The very low tin content in TM5 is most likely due to the analysed spot being dominated by polymer or silicon-rich regions rather than a true absence of tin within the composite. When considered collectively, the TM series exhibits a more uniform distribution of metallic elements compared to the PS and AS series, indicating improved filler dispersion and reduced surface segregation (Nguyen et al., 2024). Overall, the atomic percentage results highlight the dominance of lighter elements at the composite surfaces while confirming the successful incorporation of metallic fillers across all sample series (Samal & Blanco, 2021a).

Apparent reductions in tin atomic percentage in certain samples do not reflect poor filler loading but rather arise from the localised and surface-sensitive nature of EDX analysis. Therefore, the atomic percentage data should be interpreted as representative of the general surface composition rather than absolute bulk stoichiometry. When evaluated in conjunction with the weight percentage results and FESEM observations, the EDX atomic percentage analysis provides a comprehensive understanding of elemental distribution, filler dispersion, and surface chemistry within the investigated composites.

## 4.5 Verification of Components Through Fourier Transform Infrared Spectroscopy Analysis

FTIR spectroscopy was employed to evaluate the chemical structure of the control materials of PDMS, tin, and lead and to compare them with selected composite samples (PS1, AS1, and TM1) containing tin-based fillers dispersed within the PDMS matrix, as shown in Figure 4.10. The control spectra provide essential reference signatures for identifying the contribution of each component to the final composite. Control tin demonstrated the lowest transmittance across the entire wavenumber range, particularly below 1500 $cm^{-1}$, where highly conductive metallic phases tend to produce strong IR absorption due to free-electron interactions with incident infrared radiation. This behaviour aligns with reported spectral responses of metal surfaces, where broad, diffuse absorption is typical (Putz et al., 2023).

In contrast, Control PDMS exhibited consistently high transmittance, exceeding 90% throughout much of the spectrum, indicative of its well-known optical transparency and low IR absorption characteristics. The presence of distinct peaks associated with C–H stretching, Si–$CH_3$ bending, and Si–O–Si network vibrations confirm the characteristic siloxane backbone of PDMS (Bistričić et al., 2013). Control Lead, meanwhile, displayed intermediate transmittance values (approximately 75 – 80%), suggesting moderate absorption that is stronger than PDMS but weaker than tin. This behaviour is consistent with the more limited IR activity of lead compared to tin due to differences in electronic structure and oxide formation tendencies.

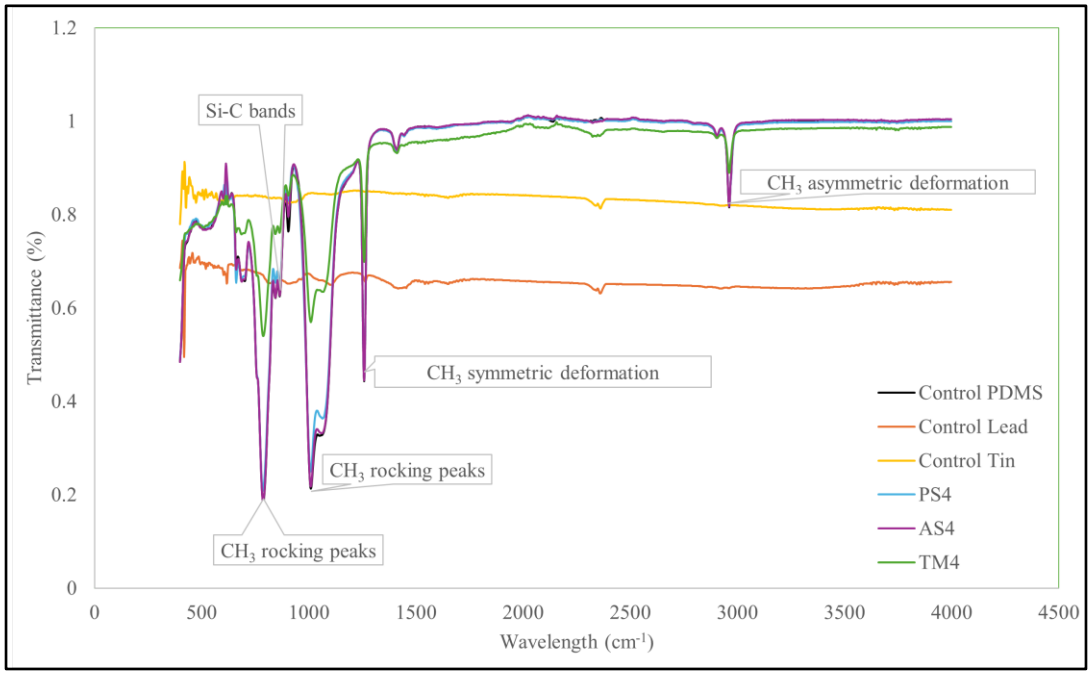


Figure 4.10 FTIR Spectrum of The Control Samples and 40% Metal Filler From Each Series of Samples

Across all composite samples, the characteristic PDMS absorption peaks remained visible, indicating that the underlying polymer network remained chemically intact after incorporation of metallic fillers. This preservation of key functional groups confirms that tin and alloy fillers did not chemically degrade or break down the siloxane framework. However, the composite spectra showed noticeable reductions in transmittance compared to pure PDMS (Bistričić et al., 2013a), reflecting the increasing presence of metal particles within the matrix and their interaction with IR radiation.

Furthermore, subtle changes in the fingerprint region (1500 to 500 $cm^{-1}$), including additional shoulders and peak broadening, indicate weak interactions occurring at the polymer–filler interface. These spectral features support the conclusion that metallic fillers were successfully integrated into the PDMS network, even though they did not form strong chemical bonds with the polymer. Such modifications are consistent with literature reporting the influence of metal–polymer interfacial contacts on IR absorption behaviour (Zainal Abidin, Mukhtar, Mahmood, Abdul Wahab, Zainon, & Roslan, 2025).

Overall, the FTIR results confirm that the chemical integrity of PDMS was preserved while metallic fillers were effectively incorporated, producing systematic reductions in transmittance and minor spectral shifts. These subtle modifications align

with the expected behaviour of polymer–metal composites and correlate with the structural characteristics observed from FESEM and XRD analyses.

### 4.5.1 FTIR Analysis of PS Series

The FTIR spectra of the PS series presented in Figure 4.11, consistently exhibited the fundamental absorption bands of PDMS, including the C–H stretching vibrations around 2960–2850 $cm^{-1}$, the Si–$CH_3$ bending mode at approximately 1260 $cm^{-1}$, and the dominant Si–O–Si asymmetric stretching peak near 1020 $cm^{-1}$ (Bistričić et al., 2013b). The retention of these peaks across all samples demonstrates that the PDMS matrix remained chemically stable and did not undergo degradation despite the increasing incorporation of pure tin.

As tin content increased from PS1 to PS6, a progressive reduction in overall transmittance was observed, most prominently in the fingerprint region below 1500 $cm^{-1}$. This reduction signifies a higher degree of IR absorption by the metallic filler, consistent with tin's intrinsic absorption behaviour. The change in transmittance is clear evidence that tin particles were successfully embedded within the polymer network and increasingly dominated the spectral signature at higher loadings.

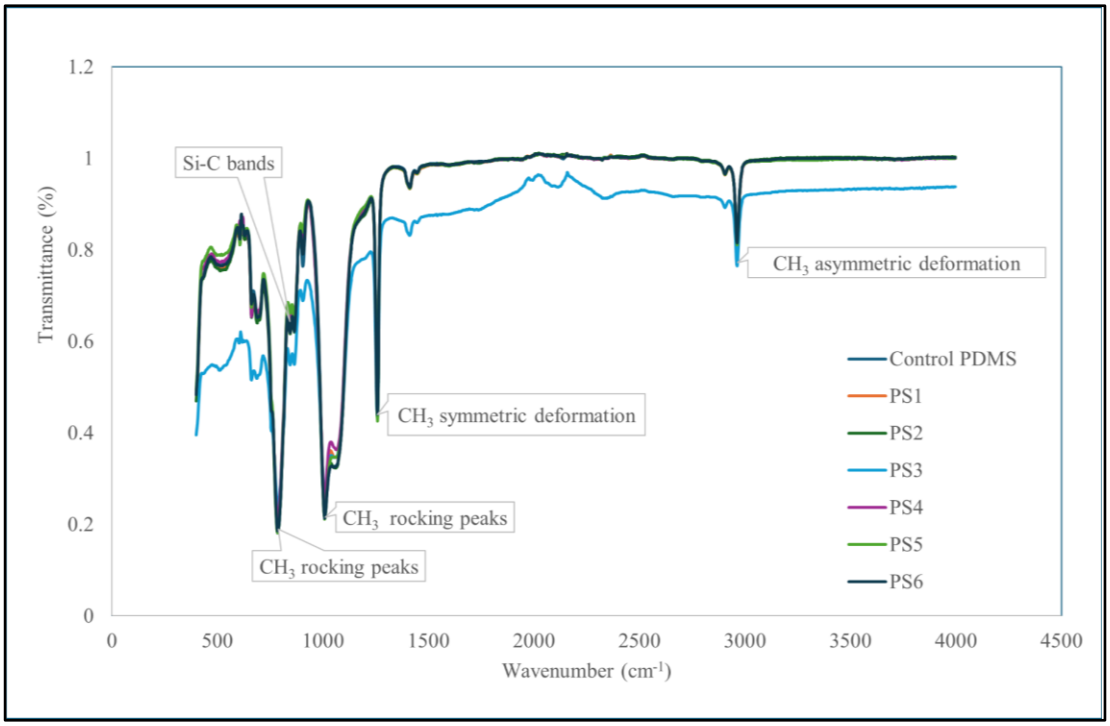


Figure 4.11 Overview of FTIR Results for The PS Series

The PS series also exhibited the appearance of weaker absorption shoulders within the 600–700 $cm^{-1}$ range. These features likely correspond to metal–oxygen vibrational modes arising from the presence of oxidised tin species on particle surfaces or weak interactions between tin and the PDMS siloxane network. Although these interactions are not strong enough to form new covalent bonds, they indicate light interfacial contact between the polymer and filler.

At higher filler contents (PS5 and PS6), the spectra showed more pronounced reductions in transmittance accompanied by slight peak broadening in the Si–O–Si region. This broadening suggests increased structural heterogeneity, likely caused by differences in local filler distribution and restrictions on polymer chain mobility. These spectral changes correlate with FESEM observations of microgaps and limited interfacial adhesion, indicating that tin is present throughout the matrix (Bistričić et al., 2013b).

In summary, the FTIR behaviour of the PS series confirms successful incorporation of tin with minimal chemical interaction, resulting in decreased transmittance but preserved polymer functionality. The spectral evolution across the series reflects the transition from a PDMS-dominated matrix to a tin-dominated one, consistent with increased rigidity and improved shielding performance observed at higher tin loadings.

### 4.5.2 FTIR Analysis of AS Series

The FTIR spectra of the AS series, shown in Figure 4.12, similarly retained the primary PDMS absorption peaks, indicating that the siloxane backbone remained chemically stable throughout the incorporation of tin alloy particles. As in the PS series, the C–H, Si–$CH_3$, and Si–O–Si vibrational bands were clearly identifiable in all AS samples, confirming the polymer matrix was structurally preserved (Bistričić et al., 2013b).

Compared to the PS series, however, the AS composites exhibited stronger absorption features in the lower wavenumber region between 1000 and 500 $cm^{-1}$. This enhanced absorption is attributed to the presence of tin alloy particles, which possess a more complex vibrational behaviour than pure tin and exhibit broader IR responses due to their multiphase nature. The smoother, more spherical morphology of the alloy

particles, confirmed by FESEM analysis, likely facilitated better physical contact with PDMS chains, contributing to the observed spectral intensification.

The reduction in transmittance observed from AS1 to AS6 reflects the increasing influence of metallic filler content. AS6, which contains the highest loading of alloy particles, demonstrated the most pronounced reduction in transmittance, particularly in regions associated with Si–O–Si stretching. This suggests that the alloy exerted a stronger effect on polymer chain mobility, slightly perturbing the siloxane environment without chemically altering it.

Subtle peak broadening and the appearance of additional shoulders further suggest weak but more favourable polymer–filler interactions compared to the PS series. These differences are consistent with FESEM findings showing improved interfacial adhesion in the AS series. The spherical shape and lower surface irregularity of alloy particles reduce the formation of microgaps, allowing for a more uniform dispersion within the PDMS matrix.

Overall, the FTIR results for the AS series indicate that alloy fillers have a more pronounced and more uniform influence on the polymer structure compared to pure tin. The spectra support the conclusion that alloy incorporation enhances interfacial compatibility while maintaining the chemical integrity of PDMS, contributing to improved structural and shielding performance.

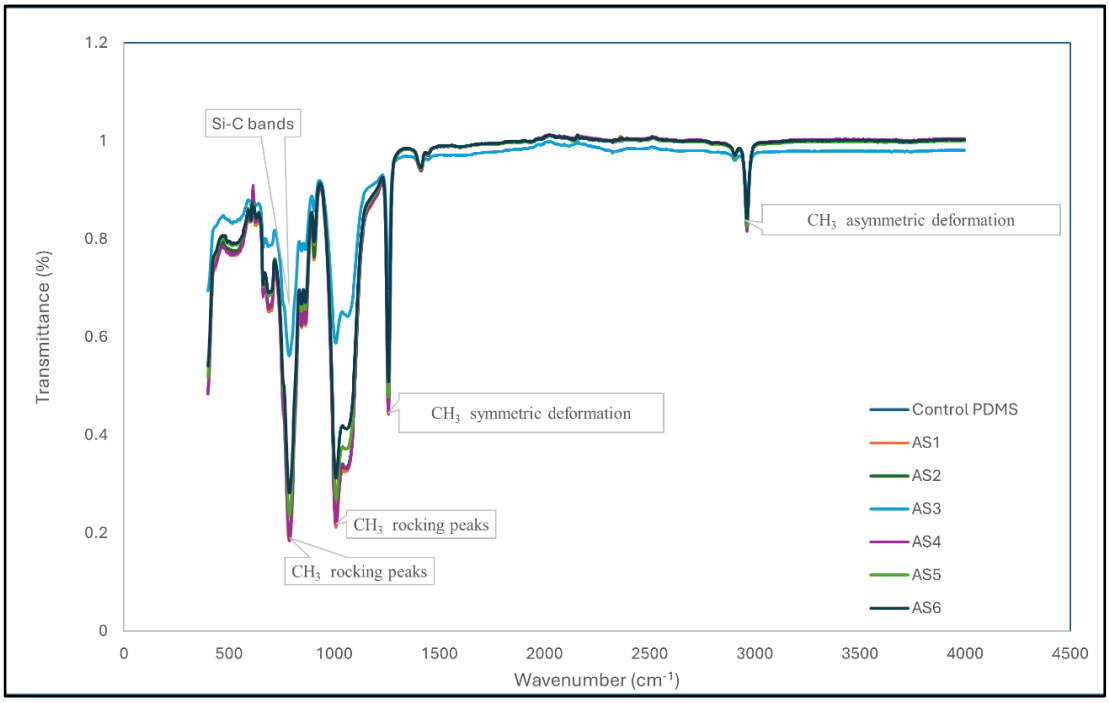


Figure 4.12 Overview of FTIR Results for the AS Series

### 4.5.3 FTIR Analysis of TM Series

The TM series exhibited spectral characteristics combining features from both the PS and AS series, reflecting the hybrid nature of their filler composition. As shown in Figure 4.13, the fundamental PDMS peaks remained present in all samples, confirming that the polymer network remained intact despite the incorporation of both pure tin and tin alloy.

With increasing filler content, the TM spectra demonstrated moderate yet consistent reductions in transmittance across the entire wavenumber range. Unlike the PS series, where sharp transmittance drops occurred suddenly at high filler loadings, or the AS series, where changes were more uniform but stronger, the TM series displayed a balanced intermediate response. This pattern suggests that the simultaneous presence of irregular tin particles and spherical alloy particles produced a more complex but harmonised interaction with the polymer matrix.

Additional absorption bands below 700 $cm^{-1}$ became increasingly prominent at higher filler contents. These bands likely arise from overlapping contributions of tin-oxygen and alloy-related vibrations, resulting in broadened features due to the heterogeneous nature of the mixed fillers. The broadened fingerprint region is consistent with XRD observations showing multiphase crystalline contributions in the TM samples.

The coexistence of two filler types also influenced polymer–filler interactions. The irregular morphology of tin introduces small microgaps and local imperfections, while the smoother alloy particles promote better adhesion. This complementary effect leads to spectral patterns that reflect both limited chemical bonding and improved physical compatibility. FESEM results support this interpretation, showing that TM samples possess more uniform filler dispersion than PS but slightly less interfacial cohesion than AS.

Overall, the FTIR spectra of the TM series confirm effective integration of mixed fillers while maintaining PDMS structural stability. The balanced spectral reductions and combined absorption characteristics demonstrate that TM composites benefit from synergistic interactions between tin and alloy phases, supporting their superior mechanical structure and optimal radiation shielding performance. performance.

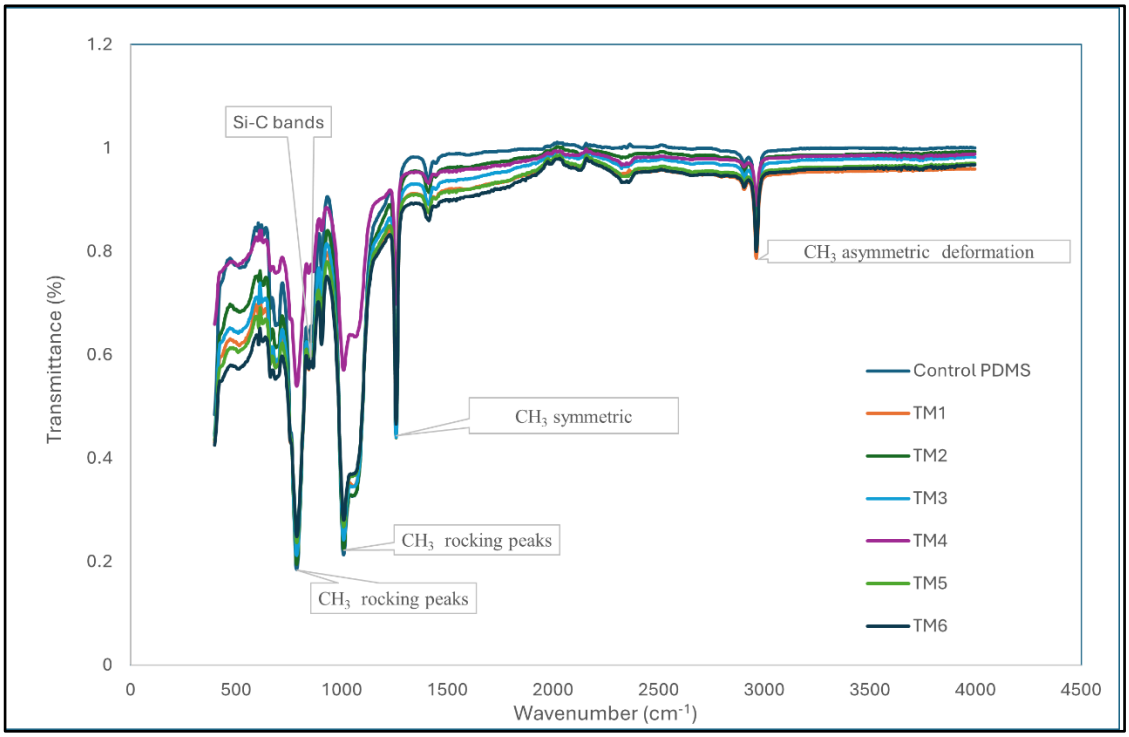


Figure 4.13 Overview of FTIR Results for the TM Series

The FTIR analysis confirms the successful incorporation of tin filler into the PDMS matrix without introducing new chemical bonds or altering the polymer's backbone structure. All samples consistently exhibit characteristic PDMS functional groups, such as Si–O–Si stretching, Si–$CH_3$ bending, and C–H vibrations, indicating that the polymer network remains chemically stable despite increasing metal loading (Bistričić et al., 2013a).

Comparisons between the control and composite samples show that the presence of tin primarily influences the peak intensity rather than peak position, reflecting physical interaction and uniform filler dispersion rather than chemical modification. Overall, the FTIR results validate that all PS, AS, and TM composites maintain structural integrity, making them suitable for subsequent mechanical and radiation-shielding evaluations.

## 4.6 Phase Identification Through X-ray Diffraction Analysis

XRD analysis was conducted to examine the phase composition, crystallinity, and structural evolution of the control materials and the fabricated composite series. The inclusion of control samples in every dataset provides a consistent baseline for

evaluating changes in diffraction behaviour due to metal–polymer interactions and variations in filler concentration. XRD patterns were recorded in the 2θ range of interest to capture both the amorphous halo associated with PDMS and the crystalline peaks characteristic of metallic tin, tin alloy, and lead in Figure 4.14. These reference profiles are essential for identifying shifts in peak intensity, peak broadening, and phase contributions that arise when metals are dispersed within the PDMS matrix. Such comparative interpretation enables detailed structural correlation with the composites' density and radiation shielding behaviour, which is discussed in the subsequent section.

The control PDMS exhibited its typical broad amorphous halo at approximately 12° – 20°, confirming the absence of long-range ordering in its siloxane backbone, a phenomenon well documented for elastomeric silicone materials (Sharma & Bose, 2021). In contrast, control tin displayed sharp and intense peaks corresponding to the tetragonal β-Sn phase, particularly near 30.6°, 32.0°, and 44.9°, verifying the crystalline nature of the metal filler. Control lead showed high-intensity diffraction peaks associated with the face-centred cubic (FCC) Pb phase (Kumar et al., 2013). This repetition facilitates identification of how metal loading influences structural transitions, including peak enhancement, suppression, or broadening due to particle–matrix interactions.

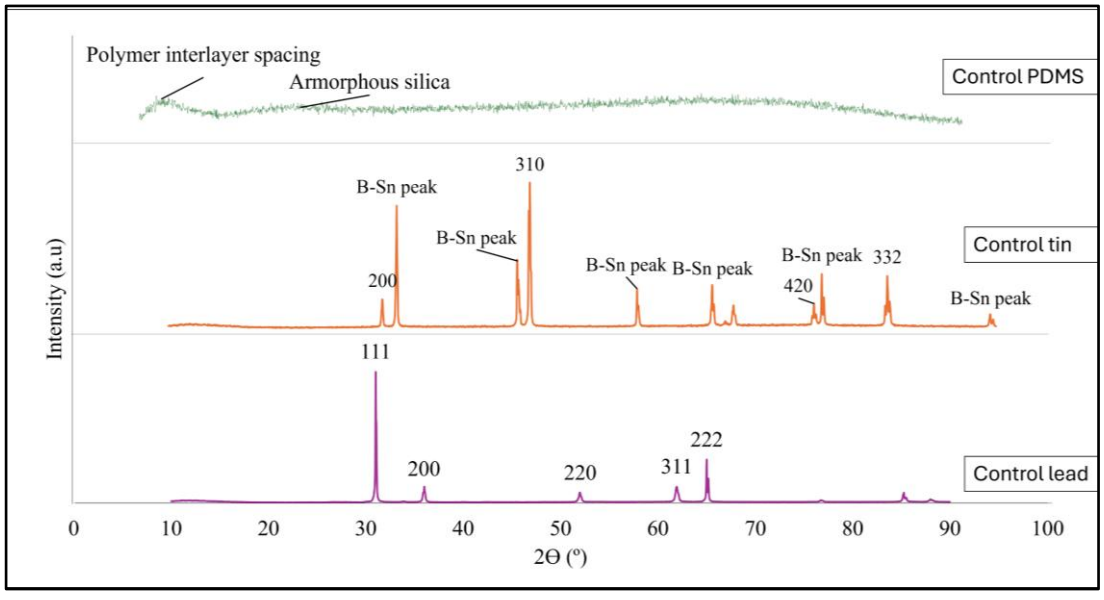


Figure 4.14 XRD Pattern of Control Samples

### 4.6.1 XRD Analysis of PS Series

The PS series consists of composites incorporating pure tin filler at 50% (PS5) and 60% (PS6) concentrations, with the control PDMS, control tin, and control lead XRD profiles included in Figure 4.15. The tin reflections were present but remained partially masked by the polymer background, indicating sufficient dispersion of tin particles within the matrix. This behaviour suggests that, at 50% loading, the polymer network still plays a dominant structural role, with tin contributing moderate crystallinity without overwhelming the amorphous signature.

Comparison with control tin highlights how the peaks in PS5 appear slightly reduced and broadened, likely due to strain effects and reduced crystallite size as tin particles interact with the PDMS matrix. Such broadening is expected when metallic particles undergo partial encapsulation or limited mobility within a polymer, which restricts full lattice development (Abdullah et al., 2019). Meanwhile, comparison with control PDMS confirms the retention of the amorphous halo, illustrating that the polymer matrix maintains its structural identity even in the presence of substantial filler content.

At PS6, the tin peaks became significantly more intense and sharper, closely resembling the control tin profile. This increase in peak definition indicates a transition toward filler-dominated structural behaviour (Adeniyi & Ighalo, 2021). The PDMS amorphous halo remains visible but is substantially subdued, reflecting reduced polymer dominance within the diffraction signal. The stronger crystallinity at PS6 is consistent with the larger tin fraction, which provides more continuous domains of β-Sn, promoting improved structural ordering.

A close comparison between PS5, PS6, and control lead also confirms that none of the PS composites exhibit the FCC-Pb diffraction pattern, confirming the structural purity of the Sn–PDMS composite without phase contamination. The progressive crystallinity enhancement from PS5 to PS6 aligns with density measurements for the series, where higher metal content yields higher structural compactness, indirectly supporting improved radiation attenuation.

Overall, the PS series demonstrates a clear and progressive structural transition from PDMS-dominated amorphous behaviour at lower tin loading to tin-dominated crystalline behaviour at higher loading. This evolution is particularly important as it

explains the observed increase in MAC and RPE in later sections, where crystalline dominance correlates with improved shielding performance (Fidan et al., 2022).

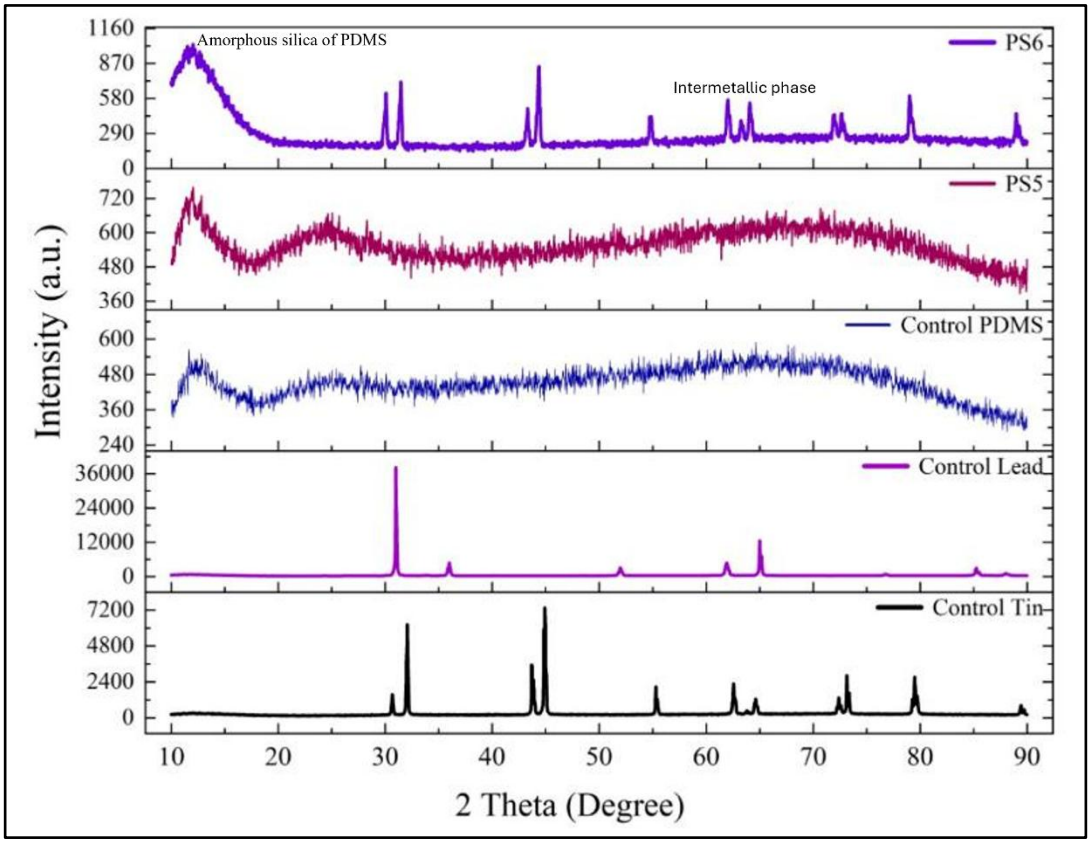


Figure 4.15 XRD Patterns of Control Samples and Composite Samples Containing 50% and 60% Metal Fillers for PS Series

### 4.6.2 XRD Analysis of AS Series

The AS composites incorporate tin alloy as the metallic filler, with AS5 (50%) and AS6 (60%) compared directly against control PDMS, control tin, and control lead in Figure 4.16. In AS5, both the PDMS halo and several crystalline peaks resembling β-Sn are observed, accompanied by lower-intensity peaks attributable to tin intermetallic phases, such as $Cu_6Sn_5$ or $Cu_3Sn$ (Kumar et al., 2013). These alloy-based reflections distinguish the AS series from the PS series, indicating a more complex phase composition due to the multiphase nature of the alloy filler.

Compared with control tin, the peaks in AS5 appear slightly broader and less symmetric, likely due to lattice distortion from copper incorporation. The reduced peak sharpness in AS5 suggests the presence of microstrain or imperfect ordering caused by

the alloying process. The PDMS amorphous halo remains detected, though partly overshadowed by metal contributions, similar to PS5 but with additional interference from copper-containing phases.

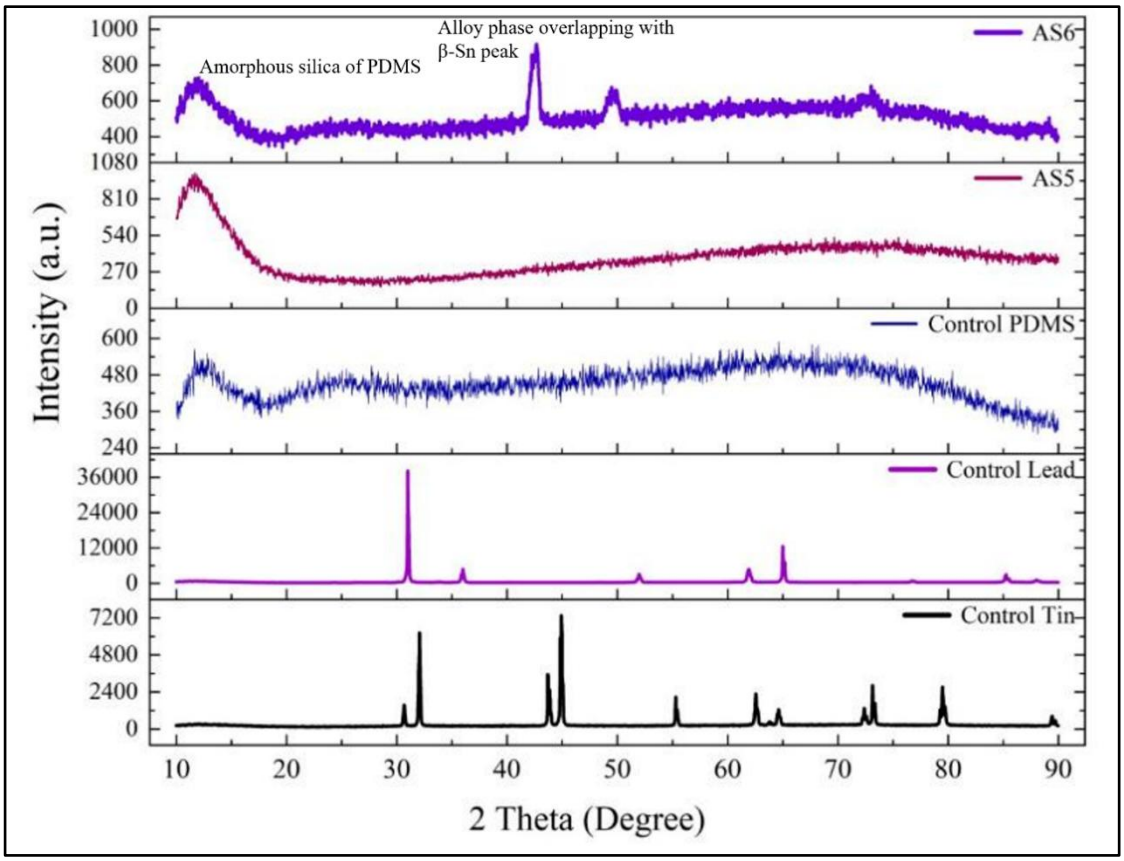


Figure 4.16 XRD Patterns of Control Samples and COMPOSITE SAMPLES Containing 50% and 60% Metal Fillers for AS series

At AS6, the XRD pattern becomes more sharply defined, with intensified reflections from both β-Sn and tin phases. The increased peak resolution indicates improved crystallinity as filler content increases, consistent with greater metallic continuity within the PDMS matrix. The alloy peaks in AS6 are more pronounced compared with AS5, supporting the conclusion that tin alloy microstructures are more structurally influential at high loading levels.

The inclusion of control lead once again provides a structural reference, confirming the absence of Pb-related peaks and ensuring there is no phase contamination during fabrication. The AS series differs from the PS series by exhibiting slightly broader peaks at both AS5 and AS6, consistent with multiphase alloy-induced.

This behaviour also suggests that the alloy fillers may contribute differently to shielding compared with pure tin, a hypothesis supported by later MAC and RPE analysis. In summary, the AS series shows a structured evolution where both tin and tin alloy phases co-exist, producing more complex crystallographic signatures. This dual-phase behaviour may enhance photon interaction mechanisms, but peak broadening suggests microstructural heterogeneity, which may influence scattering, density distribution, and ultimately RPE.

### 4.6.3 XRD Analysis of TM Series

The TM series consists of composites containing a combination of both pure tin and tin alloy, making it structurally more complex than the PS and AS single-filler composite. Control PDMS, control tin, and control lead profiles are again included to allow systematic comparison with TM5 and TM6 in Figure 4.17. At TM5, the diffraction pattern shows tin peaks as the dominant crystalline features, supported by weaker reflections corresponding to tin intermetallics. This indicates that tin maintains structural dominance even in the presence of the alloy, particularly at 50% loading.

Compared with PS5, the tin peaks in TM5 appear slightly sharper, likely due to reduced matrix interference when alloy filler is also present. Compared with AS5, TM5 displays fewer broad alloy-induced peaks, supporting the interpretation that pure tin remains structurally dominant. The PDMS amorphous halo is still visible, but weaker than in PS5 and AS5, suggesting a more crystalline-rich system at equivalent loading (Abdullah et al., 2019).

At TM6, the XRD pattern becomes strongly crystalline, with sharp, intense β-Sn peaks and well-defined tin reflections. The combination of two crystalline phases yields a higher overall crystallinity than either PS6 or AS6 alone. The reduced prominence of the PDMS halo indicates minimal amorphous contribution at high loading, with the microstructure increasingly dominated by metallic pathways (Kumar et al., 2013).

Comparison with control tin shows close alignment of major β-Sn peaks, confirming the preservation of the tin crystalline structure even in the presence of alloy phases. Meanwhile, the difference from the control lead confirms the structural purity of the TM series. The alloy peaks in TM6 are clearer than in TM5, demonstrating that tin phases integrate more effectively at higher filler concentration. Overall, the TM

series exhibits the highest crystallinity among all composites, supported by the strongest and sharpest peaks. The dual-phase crystalline reinforcement explains the superior density and radiation-shielding performance reported later, where TM6 in particular demonstrates enhanced MAC and RPE values consistent with its highly organised crystalline microstructure.

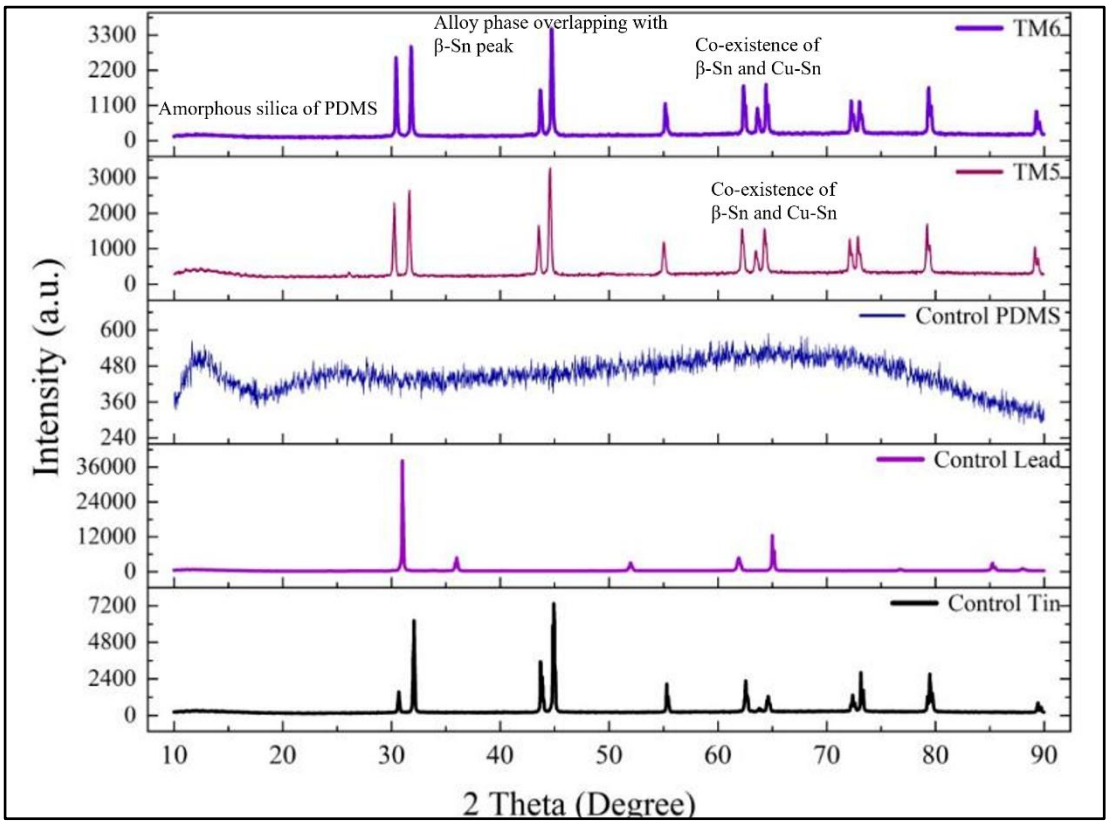


Figure 4.17 XRD Patterns of Control Samples and Composite Samples Containing 50% and 60% Metal Fillers for TM Series

The XRD analysis confirms clear structural differences among the PS, AS, and TM composite series, each influenced by the nature and percentage of metal filler. Repetition of control PDMS, tin, and lead in every table provides a consistent baseline that highlights the structural shift from amorphous to crystalline dominance. PS composites exhibit a straightforward transition with increasing tin content; AS composites show more complex multiphase behaviour due to alloying; and TM composites demonstrate the strongest overall crystallinity due to combined tin and alloy reinforcement.

These structural observations directly support the radiation characterisation findings discussed in the next section. Composites with more intense and sharper

crystalline peaks, indicating higher density and more ordered atomic structures, correspondingly exhibit higher MAC and RPE values. The XRD behaviour provides a fundamental explanation for the shielding performance hierarchy observed among the PS, AS, and TM series.

## 4.7 Radiation Attenuation Through Radiation Characterisation

In this section, the focus is on evaluating the radiation shielding performance of composite samples by evaluating LAC, MAC, HVL, TVL, and RPE. These parameters offer insights into the effectiveness of composite materials in attenuating gamma radiation, which is widely utilised in radiation shielding studies. All calculations were performed by Equations (2.5) to (2.12) presented in Section *2.3.2.2* to Section *2.3.2.6.* Understanding the mathematical foundations of these equations is essential, as they link the physical properties of the material, such as density, thickness, and atomic composition, to their photon interaction probabilities, thereby enabling the estimation of shielding performance over a range of gamma energies (Adeniyi & Ighalo, 2021).

The analytical goal here is to compare the attenuation capabilities of different irradiation surface configurations: tin irradiation surface, alloy irradiation surface, and PDMS irradiation surface within the fabricated composites, as well as benchmark them against pure control materials. This comparative approach helps identify the most effective surface orientation for gamma shielding applications. Since gamma-ray interaction mechanisms (photoelectric absorption, Compton scattering, and pair production) are highly energy-dependent, the assessment includes multiple discrete photon energy levels. This not only shows the influence of material composition and structure but also offers insights into the optimal configuration for specific radiation energy ranges. Through this systematic analysis, it becomes possible to determine which material arrangements achieve the best balance between attenuation efficiency, material thickness, and practical considerations such as weight and mechanical flexibility (Hussain et al., 2011; Mahmoud et al., 2020; Mohammed & Mosa, 2025).

### 4.7.1 Linear Attenuation Coefficient

The LAC values for the control materials and the double-layer tin–PDMS composites at various gamma-ray energies are summarised in Table 4.5 and illustrated

in Figures 4.18 to 4.22. The results clearly indicate that gamma-ray attenuation performance is affected by both photon energy and irradiation surface orientation.

Among the control samples, lead and tin exhibit exceptionally high attenuation at lower photon energies. At 88.0 keV, tin achieves an LAC of 7.010 $cm^{-1}$, while lead shows complete photon absorption, indicating near-total attenuation dominated by the photoelectric effect (Yuan et al., 2024). However, as photon energy increases to 356.0 keV and 661.7 keV, the LAC values for lead and tin decrease to 3.935 $cm^{-1}$ and 1.341 $cm^{-1}$ for lead, and 1.534 $cm^{-1}$ and 0.662 $cm^{-1}$ for tin, respectively. This steady reduction demonstrates the expected transition from photoelectric absorption to Compton scattering, where interaction probability decreases with increasing photon energy (Yuan et al., 2024).

In contrast, control PDMS shows consistently low LAC values across all energies (from 0.247 $cm^{-1}$ at 88 keV to 0.020 $cm^{-1}$ at 834.8 keV), confirming that PDMS alone is a poor gamma attenuator due to its low density and low effective atomic number. When tin is integrated with PDMS in bilayer composites, the attenuation performance improves substantially, particularly when the tin layer faces the incident beam. The tin irradiation surface, LAC values for the PS series increase progressively with higher filler content. At 88 keV, the LAC rises from 2.100 $cm^{-1}$ (PS1) to 7.360 $cm^{-1}$ (PS6), demonstrating a strong correlation between tin concentration and photon absorption efficiency.

Even at higher energies (661.7 keV), PS6 maintains a relatively high LAC of 0.439 $cm^{-1}$, compared to 0.329 $cm^{-1}$ for PS1. This confirms that the photoelectric absorption by high-density tin atoms in the first layer effectively reduces photon penetration before reaching the underlying polymer (Kwon et al., 2023). Conversely, when the PDMS layer faces the source, attenuation decreases due to the lower initial interaction probability. For instance, at 88 keV, PS6 records an LAC of 5.127 $cm^{-1}$ for PDMS-side irradiation, significantly lower than 7.360 $cm^{-1}$ for pure tin irradiation, indicating that surface orientation plays a key role in shielding effectiveness (Putz et al., 2023).

A similar trend is observed in the AS and TM composite series. In the AS series, the alloy irradiation surface shows moderate LAC values that increase with Sn–Cu content, rising from 0.318 $cm^{-1}$ (AS1) to 3.202 $cm^{-1}$ (AS6) at 88 keV. For PDMS-side irradiation, LAC values remain below 1.7 $cm^{-1}$ at 88 keV, further confirming limited metallic exposure on the surface.

Table 4.5
LAC Values at Different Gamma Energies for Different Irradiation Surfaces

| Surface irradiation | Samples | LAC ($cm^{-1}$) | | | | |
|---|---|---|---|---|---|---|
| | | **88.0 keV** | **122.1 keV** | **356.0 keV** | **661.7 keV** | **834.8 keV** |
| Control | Control PDMS | 0.247 | 0.144 | 0.127 | 0.109 | 0.020 |
| | Control Lead | 0.000 | 0.000 | 3.935 | 1.341 | 0.862 |
| | Control Tin | 0.000 | 7.010 | 1.534 | 0.662 | 0.424 |
| Tin Irradiation Surface | PS1 | 2.100 | 0.965 | 0.416 | 0.329 | 0.179 |
| | PS2 | 4.459 | 1.755 | 0.368 | 0.387 | 0.204 |
| | PS3 | 4.307 | 1.907 | 0.490 | 0.384 | 0.264 |
| | PS4 | 5.888 | 2.325 | 0.515 | 0.427 | 0.231 |
| | PS5 | 7.028 | 2.908 | 0.486 | 0.399 | 0.182 |
| | PS6 | 7.360 | 3.639 | 0.790 | 0.439 | 0.306 |
| PDMS Irradiation Surface | PS1 | 1.376 | 0.710 | 0.308 | 0.257 | 0.016 |
| | PS2 | 3.630 | 1.578 | 0.416 | 0.320 | 0.033 |
| | PS3 | 2.916 | 1.402 | 0.577 | 0.321 | 0.081 |
| | PS4 | 4.152 | 1.711 | 0.526 | 0.339 | 0.128 |
| | PS5 | 5.224 | 2.434 | 0.545 | 0.448 | 0.279 |
| | PS6 | 5.127 | 3.590 | 0.714 | 0.471 | 0.247 |
| Alloy irradiation Surface | AS1 | 0.318 | 0.268 | 0.282 | 0.078 | 0.144 |
| | AS2 | 0.679 | 0.446 | 0.518 | 0.213 | 0.138 |
| | AS3 | 1.656 | 1.538 | 1.012 | 0.215 | 0.322 |
| | AS4 | 5.043 | 2.185 | 1.538 | 0.630 | 0.354 |
| | AS5 | 2.543 | 1.970 | 1.553 | 0.670 | 0.447 |
| | AS6 | 3.202 | 2.032 | 1.396 | 0.553 | 0.379 |
| PDMS Irradiation Surface | AS1 | 1.178 | 0.804 | 0.928 | 0.492 | 0.229 |
| | AS2 | 1.258 | 0.890 | 1.094 | 0.506 | 0.296 |
| | AS3 | 0.609 | 0.499 | 0.447 | 0.248 | 0.135 |
| | AS4 | 1.673 | 0.860 | 0.686 | 0.306 | 0.220 |
| | AS5 | 1.369 | 0.892 | 0.879 | 0.326 | 0.084 |
| | AS6 | 1.125 | 1.155 | 1.156 | 0.322 | 0.102 |
| Tin Irradiation Surface | TM1 | 1.284 | 0.731 | 0.917 | 0.237 | 0.100 |
| | TM2 | 3.421 | 1.615 | 1.088 | 0.340 | 0.117 |
| | TM3 | 6.574 | 3.320 | 1.787 | 0.618 | 0.478 |
| | TM4 | 24.589 | 8.444 | 4.313 | 1.479 | 0.842 |
| | TM5 | 14.640 | 4.954 | 2.719 | 0.953 | 0.399 |
| | TM6 | 16.811 | 6.509 | 2.858 | 1.012 | 0.638 |
| Alloy irradiation Surface | TM1 | 4.712 | 1.699 | 1.813 | 0.577 | 0.229 |
| | TM2 | 4.757 | 2.211 | 1.315 | 0.465 | 0.211 |
| | TM3 | 4.189 | 2.153 | 1.370 | 0.425 | 0.274 |

| | | | | | | |
|---|---|---|---|---|---|---|
| | TM4 | 9.531 | 4.747 | 2.416 | 0.845 | 0.458 |
| | TM5 | 6.295 | 2.701 | 1.618 | 0.517 | 0.367 |
| | TM6 | 9.711 | 4.759 | 2.163 | 0.996 | 0.561 |

The TM series demonstrates the most effective shielding among all composites, reflecting its balanced dual-filler composition. When irradiated on the tin surface, LAC values increase sharply from 1.284 $cm^{-1}$ (TM1) to an impressive 24.589 $cm^{-1}$ (TM4) at 88 keV, before moderating slightly for higher filler ratios (16.811 $cm^{-1}$ for TM6). Even at 661.7 keV, TM4 maintains an LAC of 1.479 $cm^{-1}$, substantially higher than those recorded for the PS and AS series. This confirms superior photon attenuation arising from synergistic absorption by both tin and tin alloy atoms (Gouda et al., 2023).

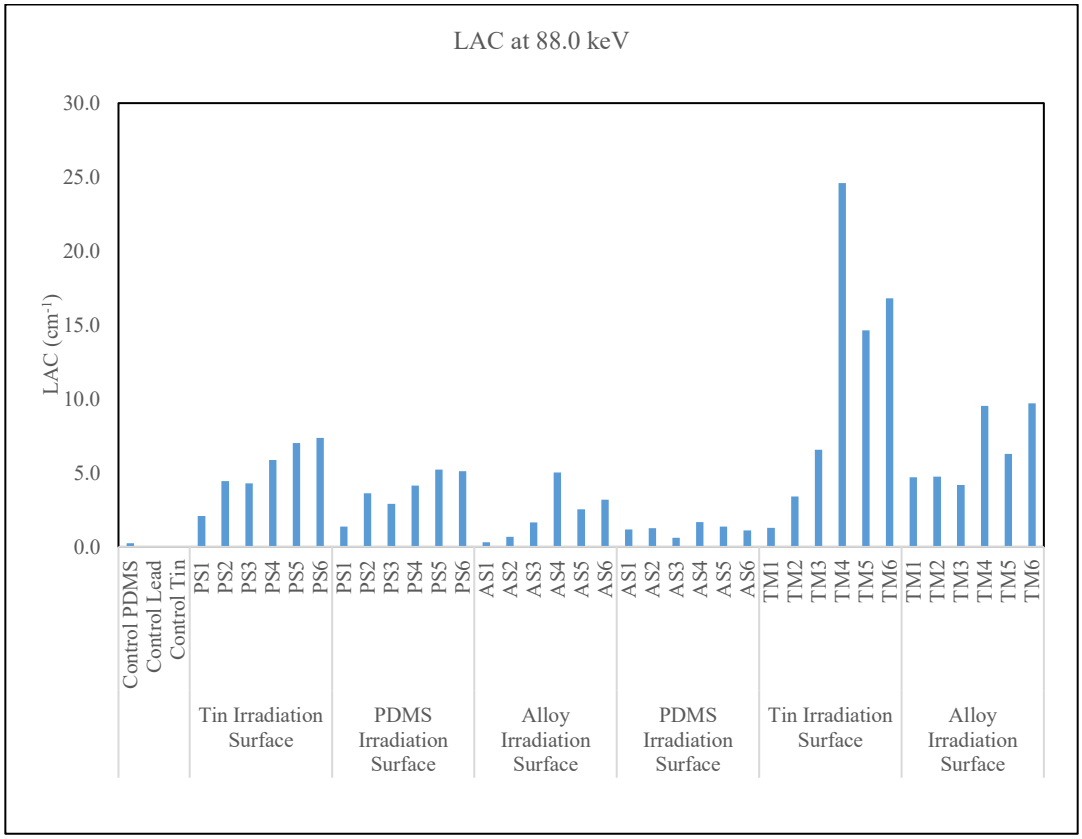


Figure 4.18 LAC of Fabricated Composite at 88.0 keV

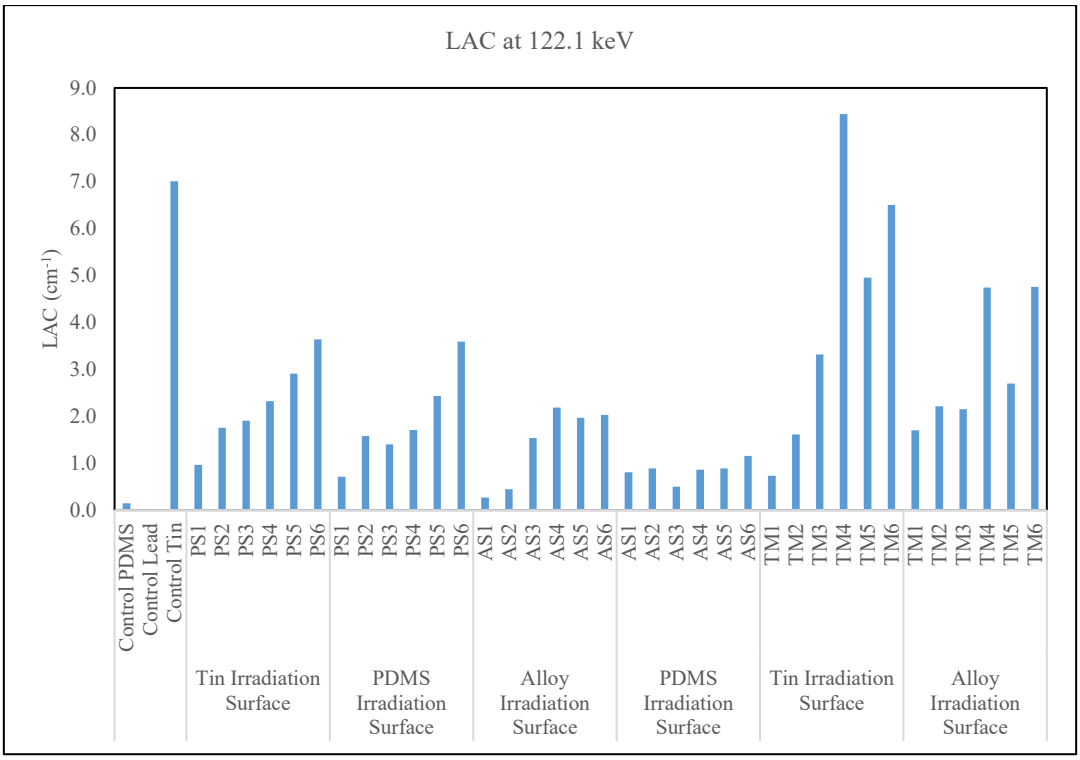


Figure 4.19 LAC of Fabricated Composite at 122.1 keV

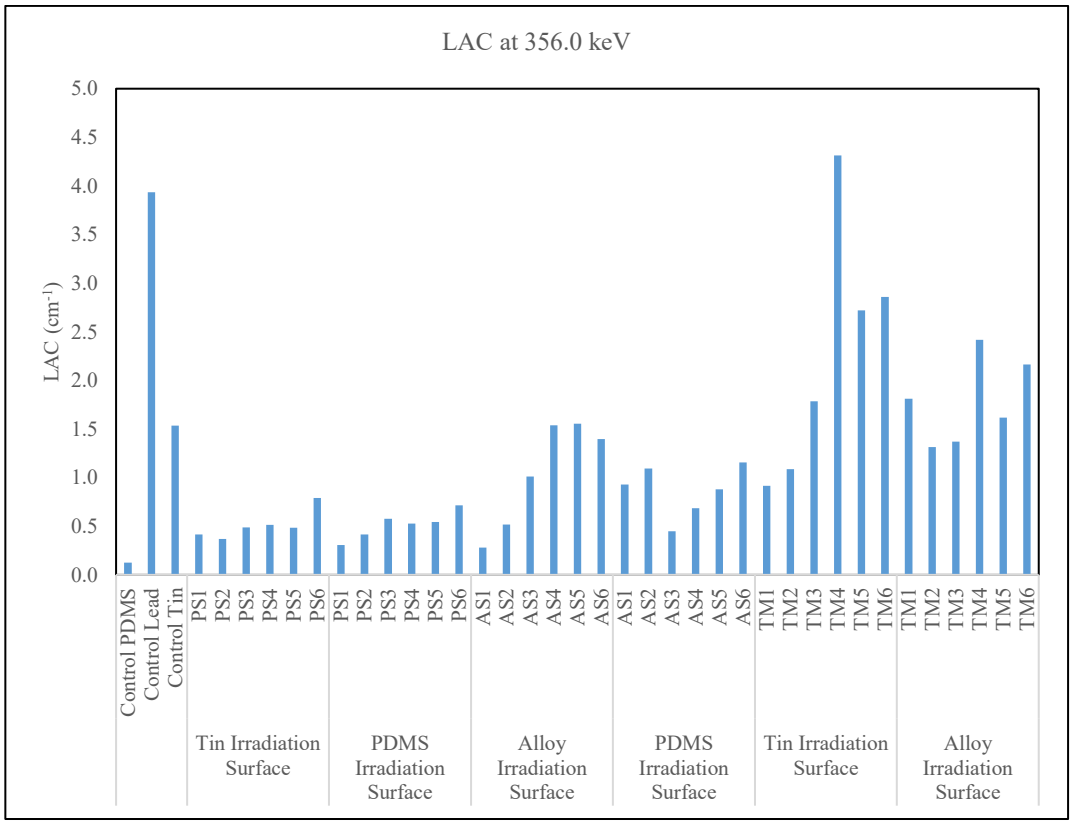


Figure 4.20 LAC of Fabricated Composite at 356.0 keV

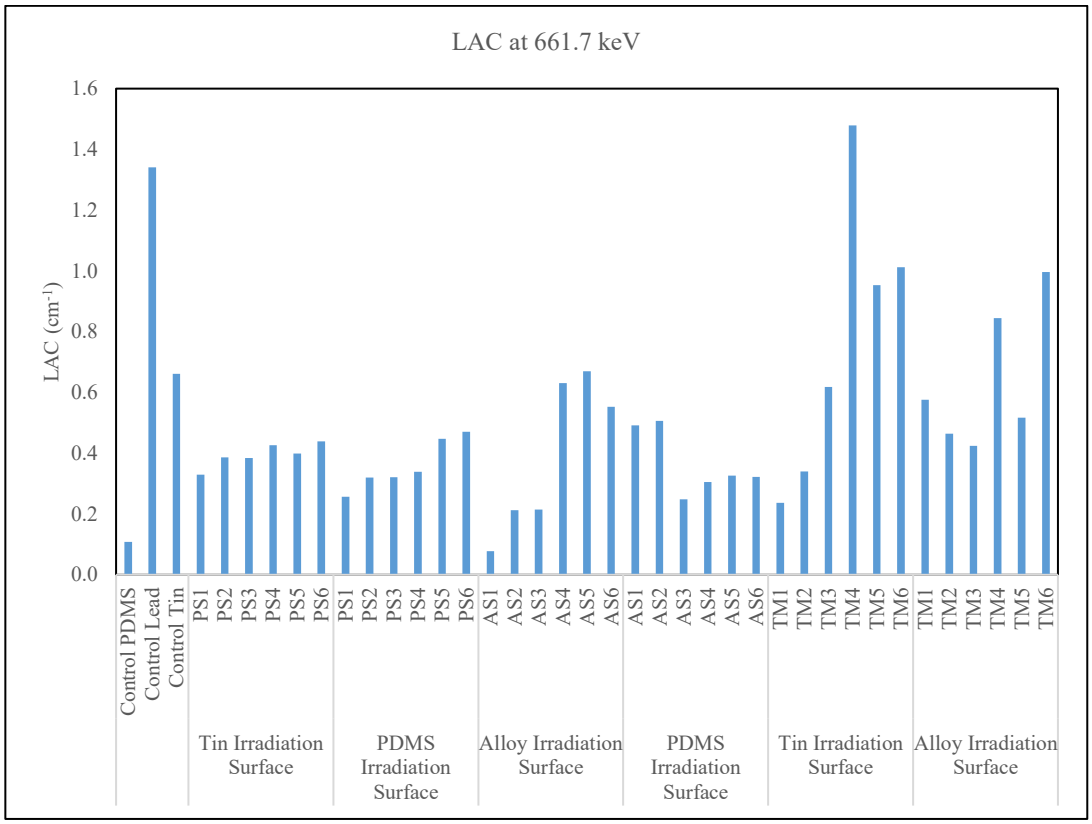


Figure 4.21 LAC of Fabricated Composite at 661.7 keV

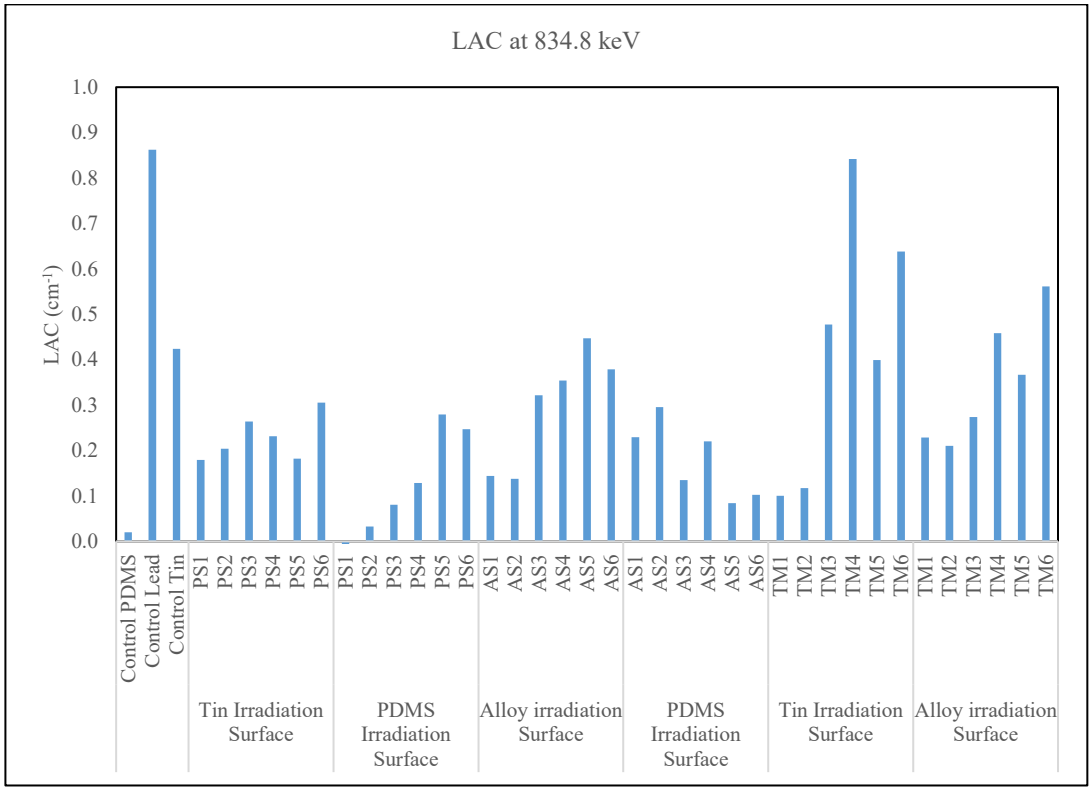


Figure 4.22 LAC of Fabricated Composite at 834 keV

On the alloy irradiation surface, TM composites similarly show strong attenuation, with LAC values ranging from 4.712–9.711 $cm^{-1}$ at 88 keV and 0.425 – 0.996 $cm^{-1}$ at 661.7 keV, reinforcing the effectiveness of dual-layer metal–polymer configurations.

Across all materials, a decreasing LAC trend is evident with increasing photon energy, consistent with theoretical expectations. At lower energies, the photoelectric effect dominates, particularly for high-density elements such as tin and lead; at intermediate energies, Compton scattering becomes the prevailing interaction, leading to reduced attenuation efficiency; and at higher energies (661 keV), pair production begins to emerge, though its influence remains minor within the studied range.

In summary, the data confirm that both material composition and irradiation surface orientation critically influence gamma-ray attenuation. High-density layers facing the incident beam significantly enhance absorption, while the underlying PDMS layer contributes to mechanical support and secondary photon moderation. The TM series exhibits the most balanced and effective performance, validating its suitability as a high-efficiency, flexible gamma-ray shielding composite (Gilys et al., 2022).

### 4.7.2 Mass Attenuation Coefficient

The MAC results presented in Table 4.6 and illustrated in Figures 4.23 to 4.27 provide a density-normalised assessment of gamma-ray attenuation performance, enabling direct comparison between materials with different densities and thicknesses.

The data reveal a clear trend: high-density materials such as tin and lead exhibit significantly higher MAC values at low photon energies, primarily due to the dominance of the photoelectric effect in this energy region. For instance, control tin records a MAC of 0.9616 $cm^2\ g^{-1}$ at 122.1 keV, while lead shows 0.3470 $cm^2\ g^{-1}$at 356.0 keV, confirming the strong photon–electron interaction in high-density elements

In contrast, the control PDMS, characterised by its low atomic number and density, exhibits much lower MAC values across all photon energies (0.2571 $cm^2\ g^{-1}$ at 88 keV, decreasing to 0.0211 $cm^2\ g^{-1}$ at 834.8 keV), reaffirming its role as a flexible structural binder rather than a primary attenuator.

Table 4.6
MAC Values at Different Gamma Energies for Different Irradiation Surfaces.

| Surface irradiation | Samples | MAC ($cm^2 g^{-1}$) | | | | |
|---|---|---|---|---|---|---|
| | | **88.0 keV** | **122.1 keV** | **356.0 keV** | **661.7 keV** | **834.8 keV** |
| Control | Control PDMS | 0.2571 | 0.1493 | 0.1318 | 0.1131 | 0.0211 |
| | Control Lead | 0.0000 | 0.0000 | 0.3470 | 0.1183 | 0.0761 |
| | Control Tin | 0.0000 | 0.9616 | 0.2105 | 0.0908 | 0.0581 |
| Tin Irradiation Surface | PS1 | 1.544 | 0.7098 | 0.3058 | 0.2422 | 0.1316 |
| | PS2 | 3.255 | 1.2811 | 0.2687 | 0.2824 | 0.1490 |
| | PS3 | 2.354 | 1.0421 | 0.2675 | 0.2098 | 0.1441 |
| | PS4 | 3.019 | 1.1924 | 0.2639 | 0.2188 | 0.1185 |
| | PS5 | 3.003 | 1.2427 | 0.2076 | 0.1705 | 0.0778 |
| | PS6 | 2.337 | 1.1554 | 0.2507 | 0.1395 | 0.0970 |
| PDMS Irradiation Surface | PS1 | 1.012 | 0.5223 | 0.2266 | 0.1892 | 0.0118 |
| | PS2 | 2.650 | 1.1516 | 0.3036 | 0.2339 | 0.0240 |
| | PS3 | 1.594 | 0.7661 | 0.3152 | 0.1755 | 0.0440 |
| | PS4 | 2.129 | 0.8774 | 0.2697 | 0.1736 | 0.0659 |
| | PS5 | 2.233 | 1.0402 | 0.2328 | 0.1915 | 0.1193 |
| | PS6 | 1.627 | 1.1396 | 0.2266 | 0.1495 | 0.0783 |
| Alloy irradiation Surface | AS1 | 0.257 | 0.2159 | 0.2276 | 0.0629 | 0.1164 |
| | AS2 | 0.468 | 0.3078 | 0.3574 | 0.1468 | 0.0949 |
| | AS3 | 0.714 | 0.6627 | 0.4361 | 0.0927 | 0.1387 |
| | AS4 | 1.807 | 0.7832 | 0.5512 | 0.2259 | 0.1268 |
| | AS5 | 0.818 | 0.6336 | 0.4995 | 0.2156 | 0.1438 |
| | AS6 | 0.936 | 0.5940 | 0.4082 | 0.1618 | 0.1108 |
| PDMS Irradiation Surface | AS1 | 0.950 | 0.6484 | 0.7487 | 0.3970 | 0.1851 |
| | AS2 | 0.868 | 0.6138 | 0.7547 | 0.3491 | 0.2040 |
| | AS3 | 0.262 | 0.2150 | 0.1927 | 0.1070 | 0.0582 |
| | AS4 | 0.600 | 0.3081 | 0.2460 | 0.1096 | 0.0789 |
| | AS5 | 0.440 | 0.2868 | 0.2828 | 0.1049 | 0.0271 |
| | AS6 | 0.329 | 0.3378 | 0.3379 | 0.0943 | 0.0299 |
| Tin Irradiation Surface | TM1 | 0.725 | 0.4128 | 0.5178 | 0.1339 | 0.0567 |
| | TM2 | 1.385 | 0.6538 | 0.4404 | 0.1376 | 0.0474 |
| | TM3 | 2.029 | 1.0246 | 0.5514 | 0.1909 | 0.1474 |
| | TM4 | 6.209 | 2.1323 | 1.0893 | 0.3735 | 0.2126 |
| | TM5 | 3.122 | 1.0563 | 0.5798 | 0.2032 | 0.0850 |
| | TM6 | 3.160 | 1.2234 | 0.5373 | 0.1902 | 0.1200 |
| Alloy irradiation surface | TM1 | 2.662 | 0.9599 | 1.0244 | 0.3257 | 0.1292 |
| | TM2 | 1.926 | 0.8950 | 0.5323 | 0.1882 | 0.0852 |
| | TM3 | 1.293 | 0.6644 | 0.4229 | 0.1310 | 0.0845 |

| | | | | | |
|---|---|---|---|---|---|
| | TM4 | 2.407 | 1.1986 | 0.6101 | 0.2134 | 0.1157 |
| | TM5 | 1.342 | 0.5758 | 0.3449 | 0.1102 | 0.0782 |
| | TM6 | 1.825 | 0.8946 | 0.4066 | 0.1873 | 0.1055 |

A pronounced enhancement in attenuation performance is observed for the tin–PDMS bilayer composites, especially when the pure tin surface is irradiated by the incident radiation source. In this configuration, photons first interact with the high-density tin atoms, maximising photoelectric absorption and substantially reducing photon flux before reaching the low-density PDMS layer. Similarly, PS6 demonstrates 2.337 $cm^2$ $g^{-1}$ (tin irradiation surface) versus 1.627 $cm^2$ $g^{-1}$ (PDMS irradiation surface) at 88 keV, clearly indicating the beneficial effect of proper layer orientation on shielding efficiency.

For example, the PS5 (tin irradiation surface) sample achieves a MAC of 3.003 $cm^2$ $g^{-1}$ at 88 keV, compared with 2.233 $cm^2$ $g^{-1}$ for the corresponding PDMS irradiation surface. Similarly, PS6 demonstrates 2.337 $cm^2$ $g^{-1}$ (tin irradiation surface) versus 1.627 $cm^2$ $g^{-1}$ (PDMS irradiation surface) at 88 keV, clearly indicating the beneficial effect of proper layer orientation on shielding efficiency.

In contrast, when PDMS faces the radiation source, a substantial portion of the incoming photons passes through with minimal interaction before reaching the tin layer, leading to reduced attenuation and lower MAC values across all energies. This effect becomes especially apparent at low photon energies, where the photoelectric effect is most significant.

The alloy irradiation surfaces exhibit intermediate MAC values (AS4 = 1.807 $cm^2$ $g^{-1}$ at 88 keV, decreasing to 0.1268 $cm^2$ $g^{-1}$ at 834.8 keV), indicating that while alloying may offer practical benefits such as enhanced flexibility and reduced density, the dilution of high-density constituents inevitably limits low-energy photon absorption compared to pure metallic layers.A similar pattern is observed for the TM series composites, where samples TM3 to TM6 show particularly high MAC values at lower energies (TM4 = 6.209 $cm^2$ $g^{-1}$ at 88 keV) that progressively decrease with increasing photon energy (0.2126 $cm^2$ $g^{-1}$ at 834.8 keV). This continuous decline across all configurations aligns well with theoretical expectations: at low energies, photoelectric absorption dominates; at intermediate energies (Zainal Abidin, Mukhtar, Mahmood, Abdul Wahab, Zainon, & Roslan, 2025).

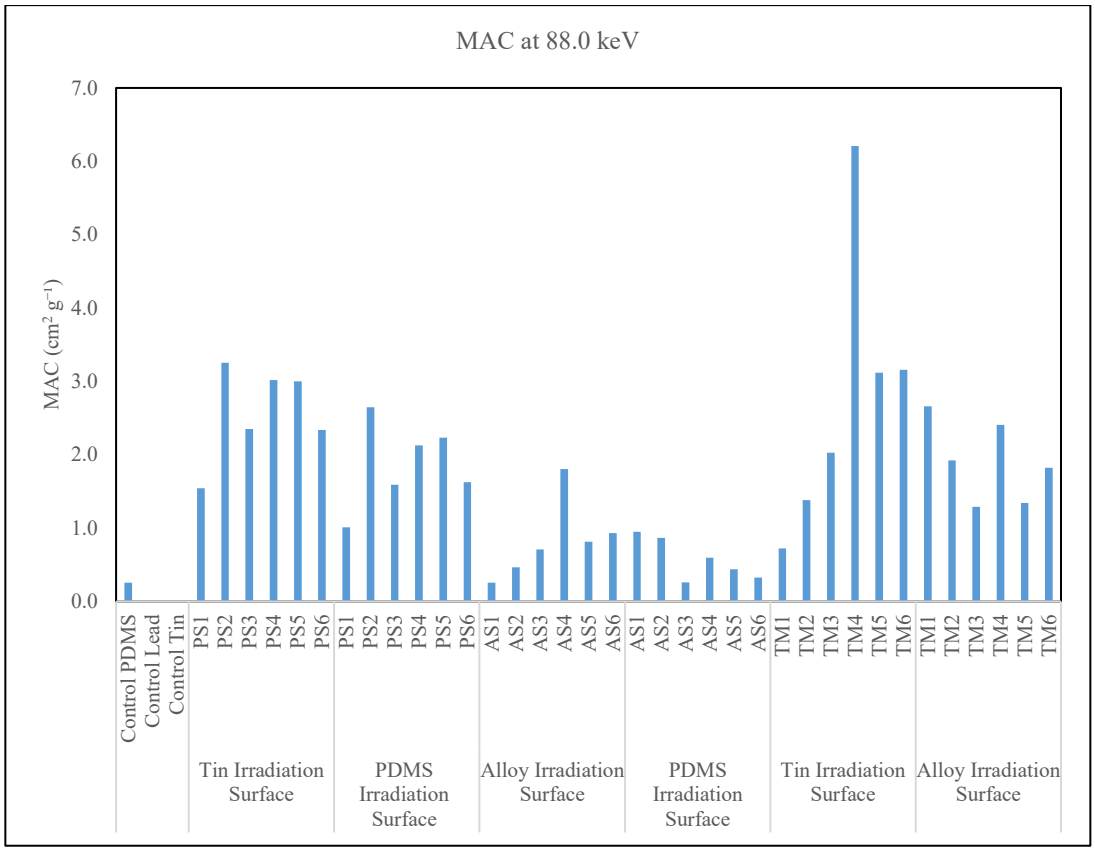


Figure 4.23 MAC of Fabricated Composite at 88.0 keV

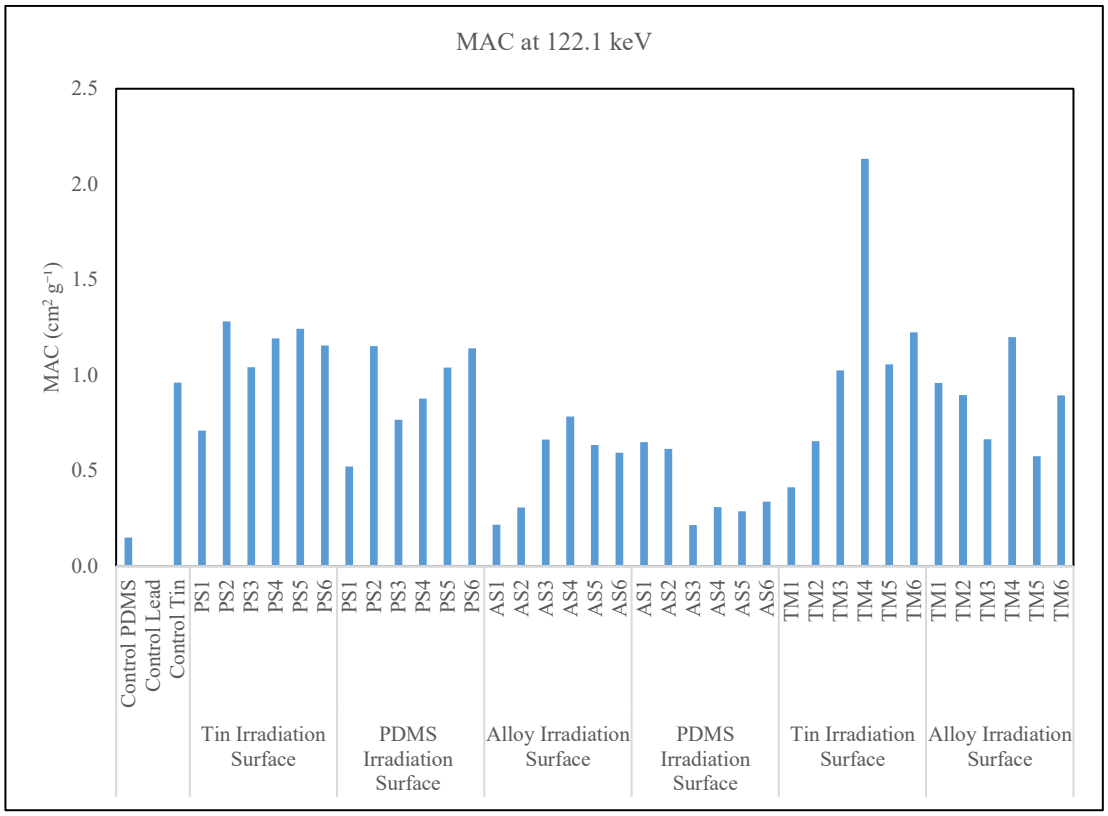


Figure 4.24 MAC of Fabricated Composite at 122.1 keV

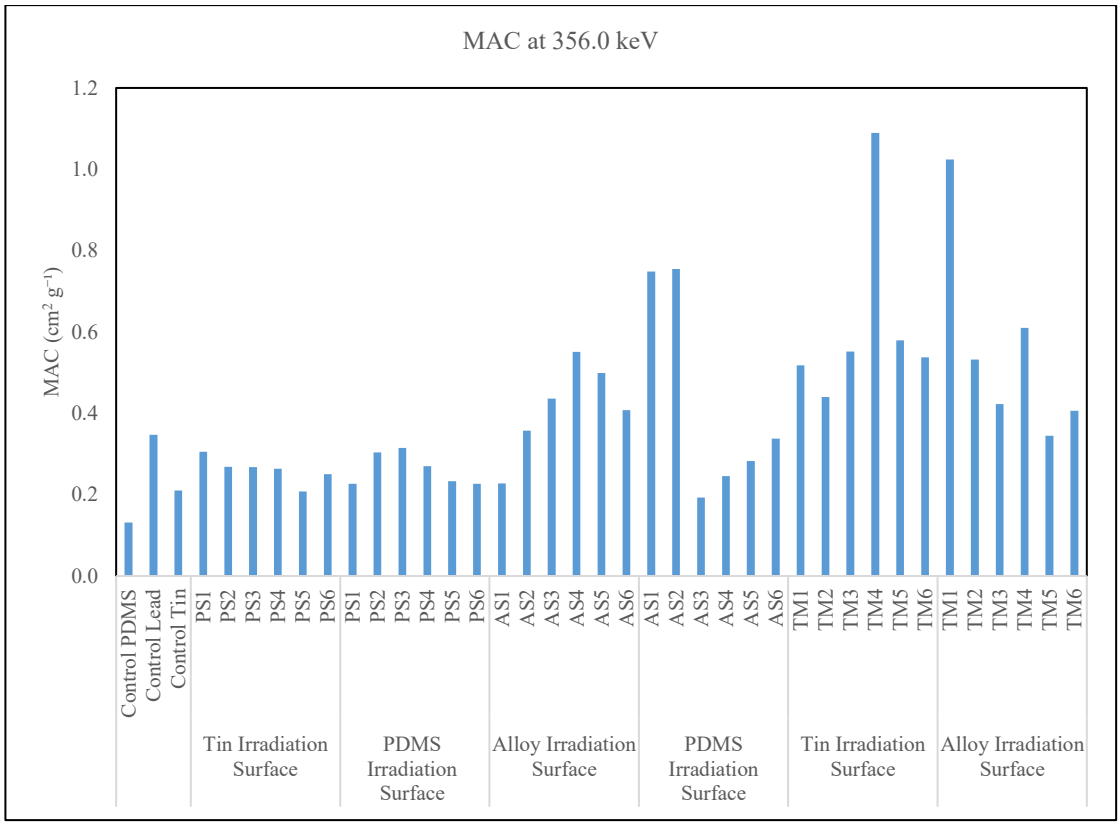


Figure 4.25 MAC of Fabricated Composite at 356.0 keV

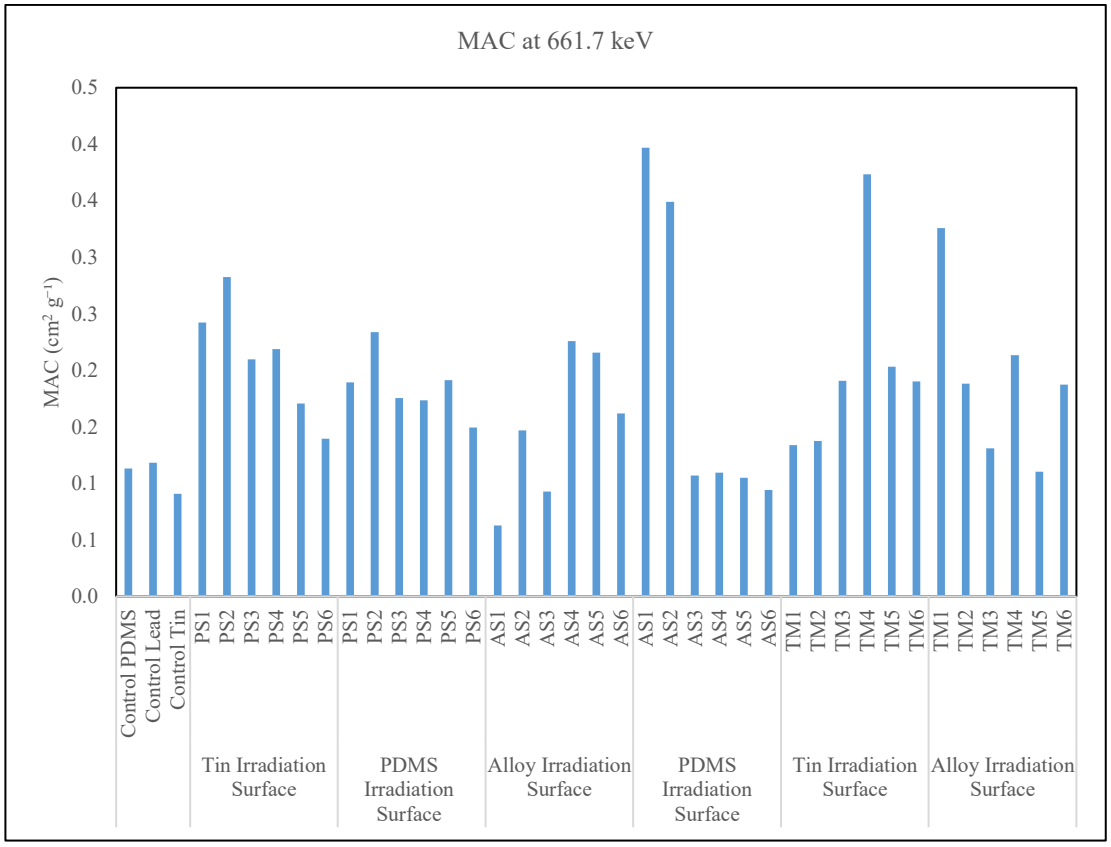


Figure 4.26 MAC of Fabricated Composite at 661.7 keV

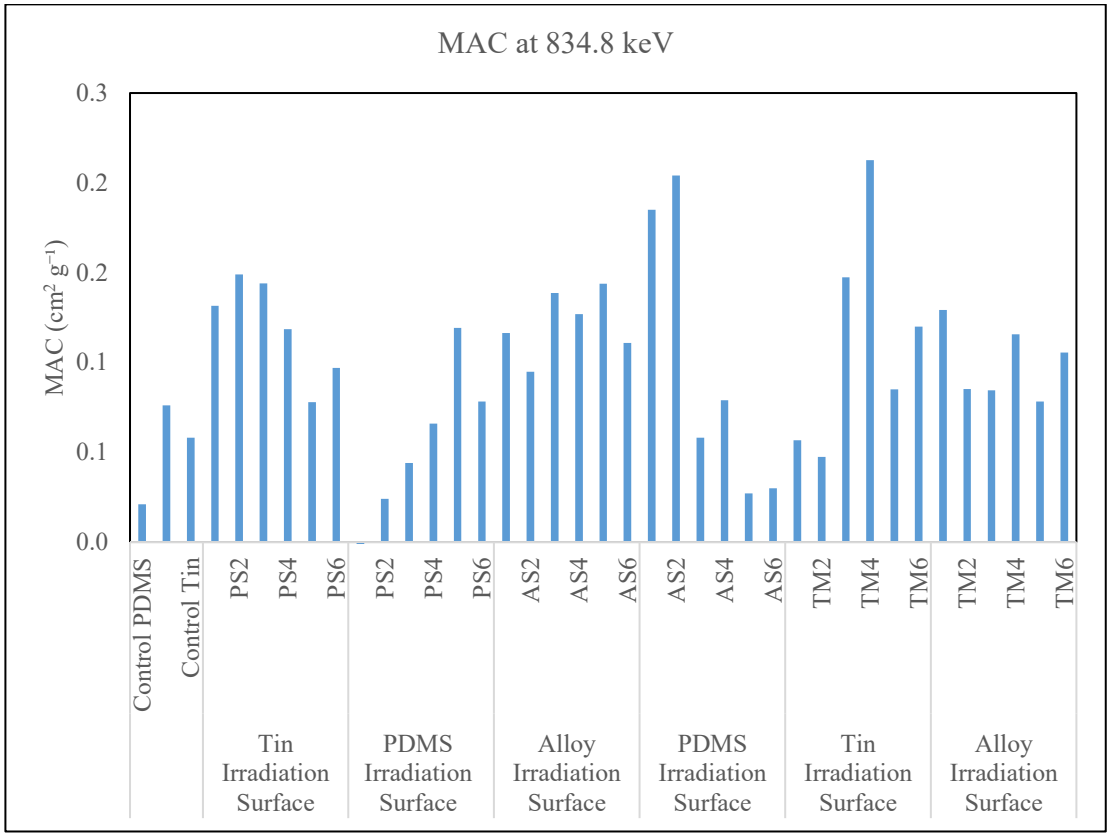


Figure 4.27 MAC of Fabricated Composite at 834.8 keV

Compton scattering becomes the main interaction mechanism, and at higher energies, attenuation efficiency diminishes further due to reduced interaction cross-sections [32]. In several PDMS irradiation surfaces, especially at higher photon energies, the MAC values approach zero or become slightly negative (PS1 = 0.0118 $cm^2$ $g^{-1}$ at 834.8 keV). These anomalous results are attributed to statistical uncertainties and low attenuation differentials at high energies, where photon transmission is nearly complete.

Overall, the graphical trends in Figures 4.22 to Figure 4.24 reinforce these findings, showing a distinct separation between high-density, bilayer, and polymer-only configurations. The results highlight the critical influence of material selection, atomic number, and layer orientation on gamma-ray attenuation efficiency in composite shielding systems (Roslan et al., 2026; Zainal Abidin. H et al., 2026).

### 4.7.3 Half Value Layer

The HVL results presented in Table 4.7 and illustrated in Figures 4.28 to 4.32 provide a thickness-based evaluation of gamma-ray shielding performance by indicating the material thickness required to reduce the incident photon intensity by 50%. Lower HVL values correspond to greater attenuation efficiency; this parameter offers a straightforward means of comparing the shielding capabilities of different materials and layer orientations (Ozyurt et al., 2018).

Among the control materials, lead exhibits exceptionally low HVL values, particularly at lower photon energies where the photoelectric effect dominates. For instance, at 356 keV, lead requires only 0.176 cm to halve the photon intensity, while at 661.7 keV and 834.8 keV, the HVL values increase modestly to 0.517 cm and 0.804 cm, respectively, demonstrating its superior shielding efficiency across a broad energy range. Tin also performs effectively, showing low HVL values at low energies due to its relatively high atomic number. At 122.1 keV, tin achieves an HVL of 0.099 cm, increasing to 1.047 cm and 1.635 cm at 661.7 keV and 834.8 keV, respectively.

Although slightly less effective than lead, tin remains a highly efficient attenuator within the tested energy range(AbuAlRoos et al., 2019; Almuqrin, Sayyed, Alorain, et al., 2024; Azman et al., 2023; Safari et al., 2024). In contrast, the control PDMS shows very high HVL values at all photon energies, confirming its poor attenuation performance.

For example, at 88.0 keV, the HVL is 2.803 cm, which increases significantly to 34.198 cm at 834.8 keV. These values highlight that PDMS, owing to its low density and low atomic number, is unsuitable as a standalone gamma-ray shield. Instead, it serves more effectively as a flexible binder or matrix within composite structures. A marked improvement in attenuation behaviours is evident in the bilayer tin–PDMS composites, particularly when the tin irradiation surface faces the incident photons (Gilys et al., 2022).

Table 4.7
HVL values at different gamma energies for different irradiation surfaces.

| Surface irradiation | Samples | HVL (cm) | | | | |
|---|---|---|---|---|---|---|
| | | **88.0 keV** | **122.1 keV** | **356.0 keV** | **661.7 keV** | **834.8 keV** |
| Control | Control PDMS | 2.803 | 4.827 | 5.468 | 6.369 | 34.198 |
| | Control Lead | 0.000 | 0.000 | 0.176 | 0.517 | 0.804 |
| | Control Tin | 0.000 | 0.099 | 0.452 | 1.047 | 1.635 |
| Tin Irradiation Surface | PS1 | 0.330 | 0.718 | 1.667 | 2.105 | 3.872 |
| | PS2 | 0.155 | 0.395 | 1.883 | 1.791 | 3.395 |
| | PS3 | 0.161 | 0.363 | 1.416 | 1.806 | 2.629 |
| | PS4 | 0.118 | 0.298 | 1.347 | 1.625 | 3.000 |
| | PS5 | 0.099 | 0.238 | 1.427 | 1.737 | 3.807 |
| | PS6 | 0.094 | 0.190 | 0.878 | 1.578 | 2.268 |
| PDMS Irradiation Surface | PS1 | 0.504 | 0.976 | 2.249 | 2.694 | 43.353 |
| | PS2 | 0.191 | 0.439 | 1.667 | 2.163 | 21.069 |
| | PS3 | 0.238 | 0.494 | 1.202 | 2.158 | 8.604 |
| | PS4 | 0.167 | 0.405 | 1.318 | 2.047 | 5.398 |
| | PS5 | 0.133 | 0.285 | 1.273 | 1.547 | 2.483 |
| | PS6 | 0.135 | 0.193 | 0.971 | 1.471 | 2.811 |
| Alloy irradiation Surface | AS1 | 2.179 | 2.590 | 2.456 | 8.892 | 4.803 |
| | AS2 | 1.021 | 1.553 | 1.338 | 3.257 | 5.040 |
| | AS3 | 0.419 | 0.451 | 0.685 | 3.222 | 2.154 |
| | AS4 | 0.137 | 0.317 | 0.451 | 1.100 | 1.959 |
| | AS5 | 0.273 | 0.352 | 0.446 | 1.034 | 1.549 |
| | AS6 | 0.217 | 0.341 | 0.497 | 1.253 | 1.829 |
| PDMS Irradiation Surface | AS1 | 0.588 | 0.862 | 0.747 | 1.408 | 3.020 |
| | AS2 | 0.551 | 0.779 | 0.633 | 1.369 | 2.343 |
| | AS3 | 1.139 | 1.390 | 1.551 | 2.791 | 5.136 |
| | AS4 | 0.414 | 0.806 | 1.010 | 2.267 | 3.150 |
| | AS5 | 0.506 | 0.777 | 0.788 | 2.124 | 8.210 |
| | AS6 | 0.616 | 0.600 | 0.600 | 2.150 | 6.780 |
| Tin Irradiation Surface | TM1 | 0.540 | 0.949 | 0.756 | 2.925 | 6.912 |
| | TM2 | 0.203 | 0.429 | 0.637 | 2.039 | 5.925 |
| | TM3 | 0.105 | 0.209 | 0.388 | 1.121 | 1.452 |
| | TM4 | 0.028 | 0.082 | 0.161 | 0.469 | 0.823 |
| | TM5 | 0.047 | 0.140 | 0.255 | 0.727 | 1.738 |
| | TM6 | 0.041 | 0.106 | 0.242 | 0.685 | 1.086 |
| Alloy irradiation Surface | TM1 | 0.147 | 0.408 | 0.382 | 1.202 | 3.032 |
| | TM2 | 0.146 | 0.314 | 0.527 | 1.491 | 3.292 |
| | TM3 | 0.165 | 0.322 | 0.506 | 1.632 | 2.530 |

| | | | | | | |
|---|---|---|---|---|---|---|
| | TM4 | 0.073 | 0.146 | 0.287 | 0.820 | 1.513 |
| | TM5 | 0.110 | 0.257 | 0.428 | 1.341 | 1.890 |
| | TM6 | 0.071 | 0.146 | 0.320 | 0.696 | 1.235 |

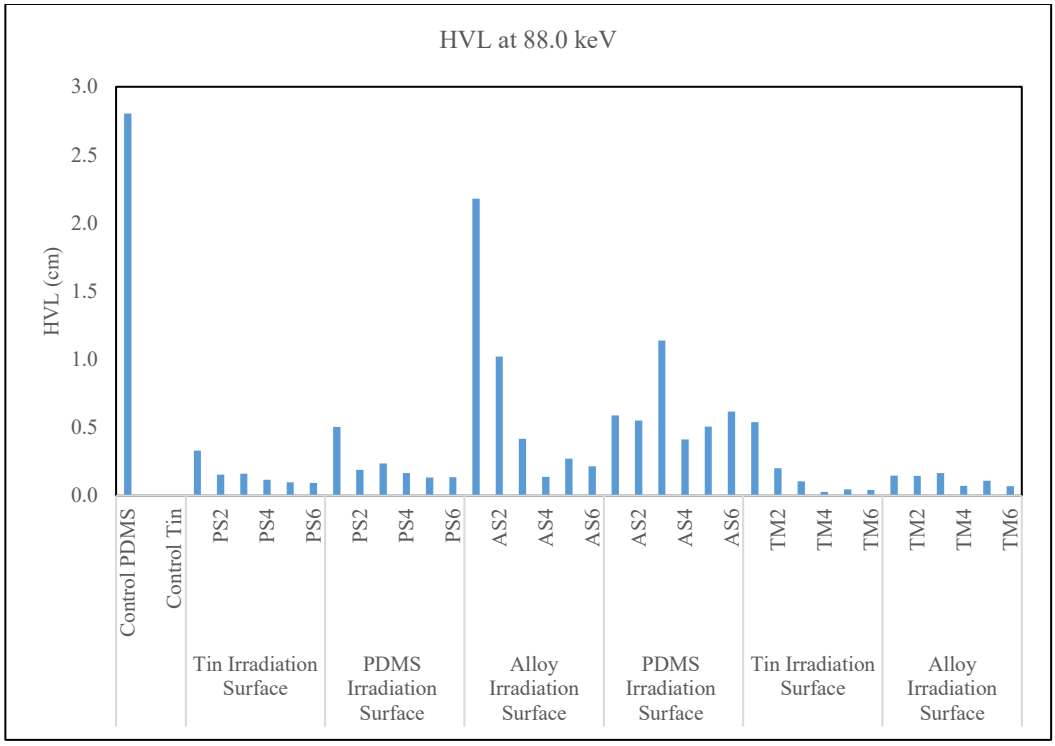


Figure 4.28 HVL of Fabricated Composite at 88.0 keV

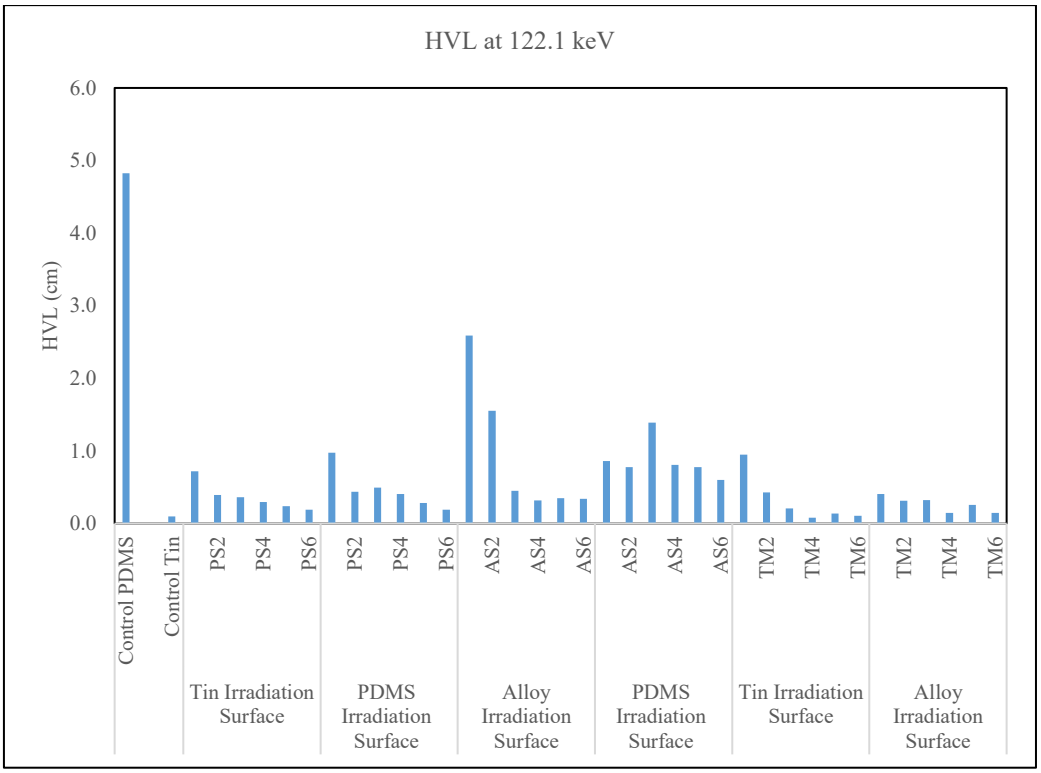


Figure 4.29 HVL of Fabricated Composite at 122.1 keV

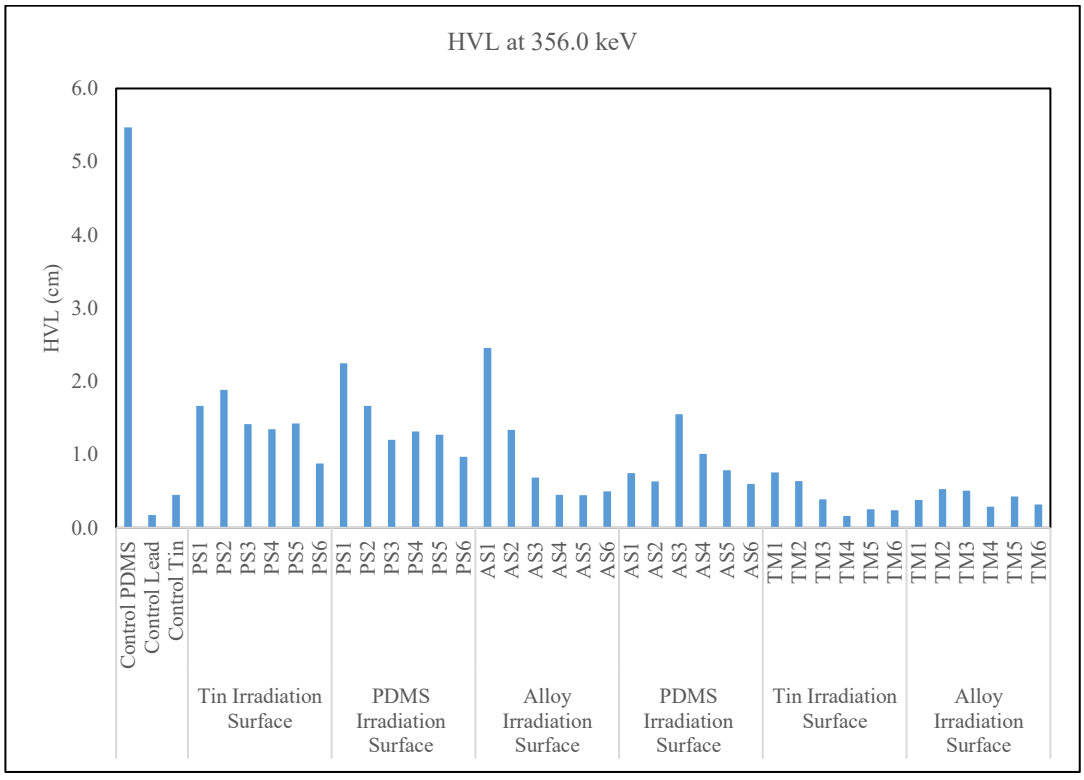


Figure 4.30 HVL of Fabricated Composite at 356.0 keV

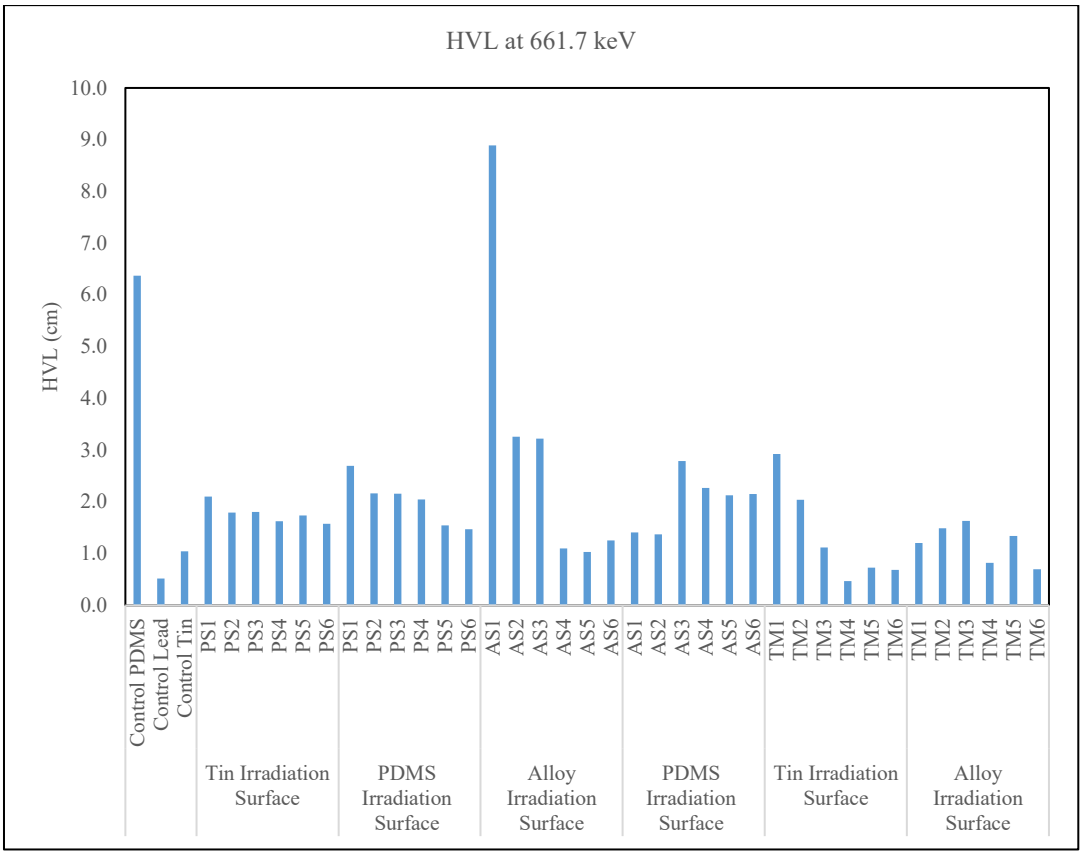


Figure 4.31 HVL of Fabricated Composite at 661.7 keV

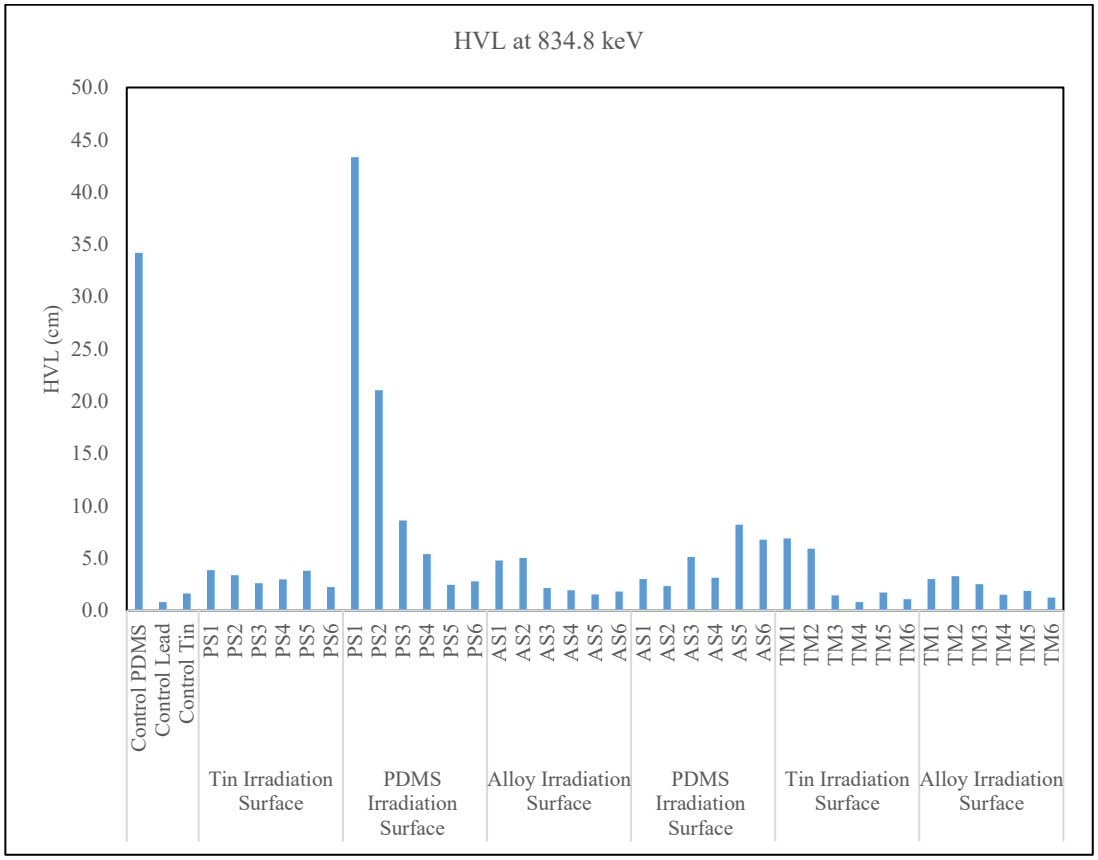


Figure 4.32 HVL of Fabricated Composite at 834.8 keV

In this configuration, the high-density tin layer acts as the primary barrier, absorbing and scattering a substantial portion of the radiation before it reaches the PDMS backing. For instance, PS5 exhibits an HVL of 0.099 cm at 88.0 keV and 1.737 cm at 661.7 keV, while PS6 achieves 0.094 cm and 1.578 cm at the same energies. These values are considerably lower than those of the corresponding PDMS irradiation surfaces, where the HVL values for PS5 and PS6 rise to 0.133 cm and 0.135 cm at 88.0 keV, and to 1.547 cm and 1.471 cm at 661.7 keV, respectively.

This clear difference emphasises the importance of layer orientation, as the PDMS irradiation surface allows greater photon penetration before reaching the metallic layer, thereby reducing overall attenuation efficiency (Roslan et al., 2025). The alloy irradiation surfaces show HVL values intermediate between those of the pure high-density layers and the PDMS-only samples. For example, AS4 records 0.137 cm at 88.0 keV and 1.100 cm at 661.7 keV, while AS5 shows 0.273 cm and 1.034 cm at the same energies. These intermediate values suggest that alloy-based configurations offer a balanced compromise between mass reduction and shielding efficiency, making them advantageous in applications where minimising weight is critical, such as aerospace systems, wearable PPE, or portable radiation barriers. Nevertheless, their performance remains slightly lower than that of pure tin or lead, particularly in the low-energy region where photoelectric interactions dominate.

A similar pattern is observed for the TM series, where the tin irradiation surfaces display notably low HVL values. For instance, TM4 achieves only 0.028 cm at 88.0 keV, increasing gradually to 0.469 cm at 661.7 keV and 0.823 cm at 834.8 keV, confirming its exceptional attenuation capability.

TM6 maintains strong performance with HVL values of 0.041 cm, 0.106 cm, and 0.242 cm at 88.0, 122.1, and 356.0 keV, respectively. Conversely, the alloy irradiation surfaces of the same group exhibit moderately higher HVL values, for example, TM4 (alloy irradiation surface) records 0.073 cm at 88.0 keV and 0.820 cm at 661.7 keV, reflecting the combined effect of material blending and reduced high-density concentration.

Overall, the HVL data demonstrate a consistent increase with photon energy across all materials and configurations. This trend aligns with theoretical expectations: as photon energy increases, the photoelectric effect contribution decreases, and Compton scattering becomes the dominant interaction mechanism, resulting in reduced attenuation and higher HVL values (AbuAlRoos et al., 2019). The graphical trends in

Figures 4.25 to 4.27 thus reaffirm the strong influence of both material composition and layer orientation on gamma-ray shielding performance, highlighting the superior efficiency of high-density, tin irradiation surface within multilayer composite systems.

### 4.7.4 Tenth Value Layer

The TVL results presented in Table 4.8 and illustrated in Figures 4.33 to Figure 4.37 offer a detailed assessment of the gamma-ray shielding efficiency of the studied composites and control materials. TVL represents the material thickness required to reduce the incident photon intensity by 90%, making it a critical indicator of shielding performance. Lower TVL values signify superior attenuation capability, while higher values indicate weaker radiation protection. The results cover photon energies from 88.0 to 834.8 keV, enabling direct comparison across control, single-filler (PS and AS series), and dual-filler (TM series).

The control samples exhibit the expected baseline characteristics. Lead achieves nearly zero TVL at lower photon energies (88.0 and 122.1 keV) and maintains excellent performance even at higher energies, with values of 0.585 cm at 356.0 keV, 1.717 cm at 661.7 keV, and 2.670 cm at 834.8 keV, due to its high atomic number and density. Tin, while less effective than lead, still demonstrates strong attenuation, recording 0.328 cm at 122.1 keV, 1.501 cm at 356.0 keV, 3.479 cm at 661.7 keV, and 5.433 cm at 834.8 keV. In contrast, pure PDMS exhibits very poor shielding capacity, with TVL values of 9.311 cm at 88.0 keV and escalating steeply to 113.602 cm at 834.8 keV, clearly demonstrating its inadequacy as a gamma-ray barrier without filler reinforcement.

The PS series (tin irradiation surfaces) shows a pronounced reduction in TVL values compared to unmodified PDMS, confirming improved attenuation efficiency. At 88.0 keV, TVL values range from 1.097 cm (PS1) to 0.313 cm (PS6), a nearly thirtyfold improvement over control PDMS. Although values increase with photon energy, they remain substantially lower than PDMS. At 356.0 keV, PS6 exhibits the lowest TVL (2.915 cm), while other samples range from 4.474 cm to 6.254 cm.

At 834.8 keV, the series records 7.536 to 12.864 cm, indicating significant though limited protection at high energies. When the PDMS surface is the irradiation side, similar trends appear but with slightly higher TVL values. PS5 and PS6 perform best, maintaining values below 1 cm at 122.1 keV and around 8–9 cm at 834.8 keV.

Table 4.8
TVL values at different gamma energies for different irradiation surfaces

| Surface irradiation | Samples | TVL (cm) | | | | |
|---|---|---|---|---|---|---|
| | | **88.0 keV** | **122.1 keV** | **356.0 keV** | **661.7 keV** | **834.8 keV** |
| Control | Control PDMS | 9.311 | 16.034 | 18.163 | 21.158 | 113.602 |
| | Control Lead | 0.000 | 0.000 | 0.585 | 1.717 | 2.670 |
| | Control Tin | 0.000 | 0.328 | 1.501 | 3.479 | 5.433 |
| Tin Irradiation Surface | PS1 | 1.097 | 2.385 | 5.536 | 6.991 | 12.864 |
| | PS2 | 0.516 | 1.312 | 6.254 | 5.951 | 11.279 |
| | PS3 | 0.535 | 1.207 | 4.703 | 5.998 | 8.734 |
| | PS4 | 0.391 | 0.990 | 4.474 | 5.397 | 9.965 |
| | PS5 | 0.328 | 0.792 | 4.740 | 5.770 | 12.645 |
| | PS6 | 0.313 | 0.633 | 2.915 | 5.240 | 7.536 |
| PDMS Irradiation Surface | PS1 | 1.673 | 3.241 | 7.470 | 8.948 | 144.014 |
| | PS2 | 0.634 | 1.459 | 5.536 | 7.185 | 69.990 |
| | PS3 | 0.790 | 1.642 | 3.992 | 7.169 | 28.581 |
| | PS4 | 0.555 | 1.346 | 4.378 | 6.801 | 17.931 |
| | PS5 | 0.441 | 0.946 | 4.227 | 5.140 | 8.250 |
| | PS6 | 0.449 | 0.641 | 3.225 | 4.888 | 9.337 |
| Alloy irradiation Surface | AS1 | 7.238 | 8.603 | 8.158 | 29.539 | 15.956 |
| | AS2 | 3.393 | 5.160 | 4.444 | 10.819 | 16.742 |
| | AS3 | 1.391 | 1.498 | 2.276 | 10.702 | 7.156 |
| | AS4 | 0.457 | 1.054 | 1.497 | 3.653 | 6.507 |
| | AS5 | 0.906 | 1.169 | 1.482 | 3.435 | 5.147 |
| | AS6 | 0.719 | 1.133 | 1.649 | 4.161 | 6.076 |
| PDMS Irradiation Surface | AS1 | 1.955 | 2.864 | 2.480 | 4.677 | 10.033 |
| | AS2 | 1.830 | 2.587 | 2.104 | 4.549 | 7.784 |
| | AS3 | 3.782 | 4.616 | 5.151 | 9.272 | 17.063 |
| | AS4 | 1.376 | 2.679 | 3.354 | 7.531 | 10.465 |
| | AS5 | 1.682 | 2.581 | 2.618 | 7.056 | 27.275 |
| | AS6 | 2.048 | 1.993 | 1.993 | 7.141 | 22.524 |
| Tin Irradiation Surface | TM1 | 1.794 | 3.151 | 2.512 | 9.718 | 22.960 |
| | TM2 | 0.673 | 1.426 | 2.117 | 6.775 | 19.681 |
| | TM3 | 0.350 | 0.694 | 1.289 | 3.723 | 4.822 |
| | TM4 | 0.094 | 0.273 | 0.534 | 1.557 | 2.735 |
| | TM5 | 0.157 | 0.465 | 0.847 | 2.416 | 5.773 |
| | TM6 | 0.137 | 0.354 | 0.806 | 2.276 | 3.607 |
| Alloy irradiation Surface | TM1 | 0.489 | 1.355 | 1.270 | 3.994 | 10.072 |
| | TM2 | 0.484 | 1.042 | 1.751 | 4.954 | 10.936 |
| | TM3 | 0.550 | 1.070 | 1.680 | 5.423 | 8.406 |

| | | | | | |
|---|---|---|---|---|---|
| TM4 | 0.242 | 0.485 | 0.953 | 2.724 | 5.025 |
| TM5 | 0.366 | 0.853 | 1.423 | 4.454 | 6.279 |
| TM6 | 0.237 | 0.484 | 1.065 | 2.311 | 4.101 |

An anomalous result for PS1 (144.014 cm at 834.8 keV) likely reflects experimental or computational artefacts. Overall, the PS series demonstrates that tin irradiation markedly enhances low-energy shielding, though efficiency decreases at higher photon energies (Yazdankish, 2024). The AS series (alloy irradiation surfaces) shows more stable performance across the photon energy spectrum. At 88.0 keV, TVL values decrease progressively from 7.238 cm (AS1) to 0.719 cm (AS6), highlighting the role of filler optimisation. At 356.0 keV, AS4 – AS6 outperform tin irradiation surface, exhibiting TVL values between 1.482 cm and 1.649 cm, comparable to pure tin. Even at 834.8 keV, the series maintains relatively low values of 5.147 – 7.156 cm, reflecting improved balance between low- and high-energy attenuation. On PDMS irradiation surfaces, the AS composites maintain reasonable efficiency, with TVL values between 1.376 – 3.782 cm at 88.0 keV and 10 – 22 cm at 834.8 keV. Minor fluctuations, particularly in AS5 and AS6, suggest variability in filler dispersion, yet the overall trend confirms that alloy irradiation enhances mid- and high-energy stability compared to tin irradiation surface.

The TM series (tin irradiation surfaces) exhibits the strongest attenuation performance among all investigated materials, approaching that of lead. At low energies, optimised samples TM4 to TM6 show extremely low TVL values (0.094 – 0.137 cm at 88.0 keV), rivalling lead's near-zero baseline.

At 356.0 keV, these samples maintain TVL below 1 cm (0.534 – 0.847 cm), and at 834.8 keV, they record 2.735 –3.607 cm, the lowest among all non-lead composites.

Lower metal filler of TM series (TM1 to TM3) show weaker performance, with TVL values up to 9.718 cm at 661.7 keV, but the higher metal filler composite, TM4 to TM6 clearly demonstrate the superior shielding potential of dual-filler metallic irradiation strategies (Kwon et al., 2023; Sushmita et al., 2022).The alloy-irradiated TM series follows a similar pattern, displaying slightly more balanced attenuation across all energies. At 88.0 keV, TVL values range from 0.237 cm (TM6) to 0.550 cm (TM3), comparable to tin irradiation surface of TM samples. At 356.0 keV, TM4 and TM6 sustain low TVL values (0.953 cm and 1.065 cm, respectively), while at 834.8 keV,

TM6 records 4.101 cm, only marginally higher than the tin irradiation surface but with a smoother energy-dependent response.

These results suggest that alloy fillers enhance uniformity and reduce abrupt fluctuations in attenuation behaviour, even if their absolute efficiency is slightly lower at certain energies. Collectively, the TVL results establish a consistent performance hierarchy that mirrors the RPE and HVL trends. Lead remains the reference material for shielding excellence but is limited by its toxicity and high density. PDMS alone performs inadequately, requiring impractically large thicknesses. Tin irradiation for the PS series provides substantial improvement, especially at low energies, but loses effectiveness at higher photon energies. Alloy irradiation of the AS series offers a more balanced performance profile, particularly in the mid-energy range. The TM composites, especially TM4–TM6, achieve the lowest TVL values overall, demonstrating the advantages of dual-filler metallic matrices. The alloy–TM samples further stabilise attenuation, offering smoother and more predictable performance across the full energy spectrum. Consequently, the TM-based composites, especially those employing alloy modification, emerge as the most effective lead-free alternatives, combining low TVL at low energies with durable high-energy protection (Gurumurthi & Rajasekar, 2025; Jamal AbuAlRoos et al., 2020b).

The TVL value of fabricated samples is presented in Figures 4.28 – 4.30. The control materials exhibit expected reference behaviour: lead maintains near-zero TVL at low energies with gradual increases to 2.670 cm at 834.8 keV, confirming its benchmark status. Tin follows a similar but weaker trajectory, while PDMS exhibits a steep slope exceeding 100 cm at 834.8 keV, underscoring its poor shielding capacity.

The PS series curves show substantial improvement at low energies, particularly PS5 and PS6, which fall below 0.4 cm at 88.0 keV but rise sharply beyond 7 – 13 cm at 834.8 keV, indicating energy-dependent decline. When irradiation occurs on the PDMS surface, the curves shift upward, confirming reduced attenuation due to the PDMS irradiation surface.

The AS series curves present a more balanced response, rising less steeply than those of the PS series. Optimised samples AS4, AS5, and AS6 maintain TVL values below 2 cm over much of the energy range, providing stable mid-energy performance. Their PDMS-surface counterparts produce flatter curves with moderate TVL (up to ~20 cm at 834.8 keV), reflecting uniform attenuation behaviour. The smoother progression

across energies highlights the synergistic effect of alloy fillers in distributing photon interactions more evenly (Bisht et al., 2025).

The TM series, particularly TM4 to TM6, exhibits the most impressive and stable behaviour. Their curves lie closest to lead across the energy range, maintaining extremely low values (<0.14 cm at 88.0 keV and <4 cm at 834.8 keV) with shallow slopes that demonstrate consistent energy stability. Earlier TM samples (TM1–TM3) follow steeper trends, but the optimised formulations cluster tightly near the lead reference, confirming the superiority of dual-filler metallic designs. The TM series displays comparably low but smoother curves; for instance, TM6 records 0.237 cm at 88.0 keV and 4.101 cm at 834.8 keV, producing one of the most stable attenuation profiles among all systems.

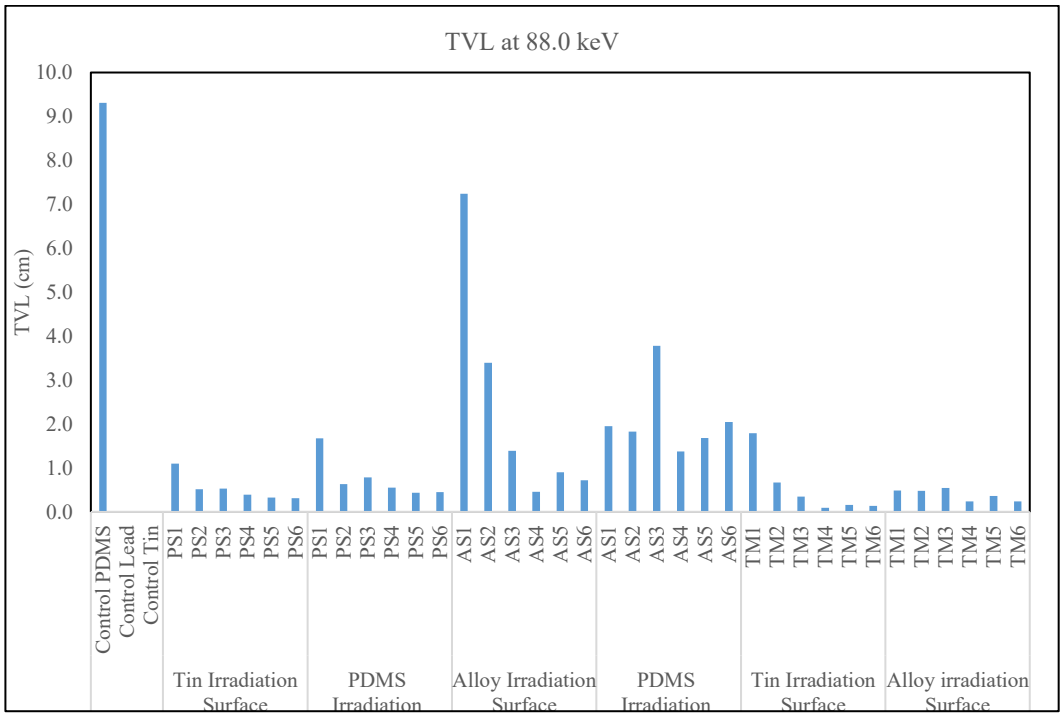


Figure 4.33 TVL of Fabricated Composite at 88.0 keV

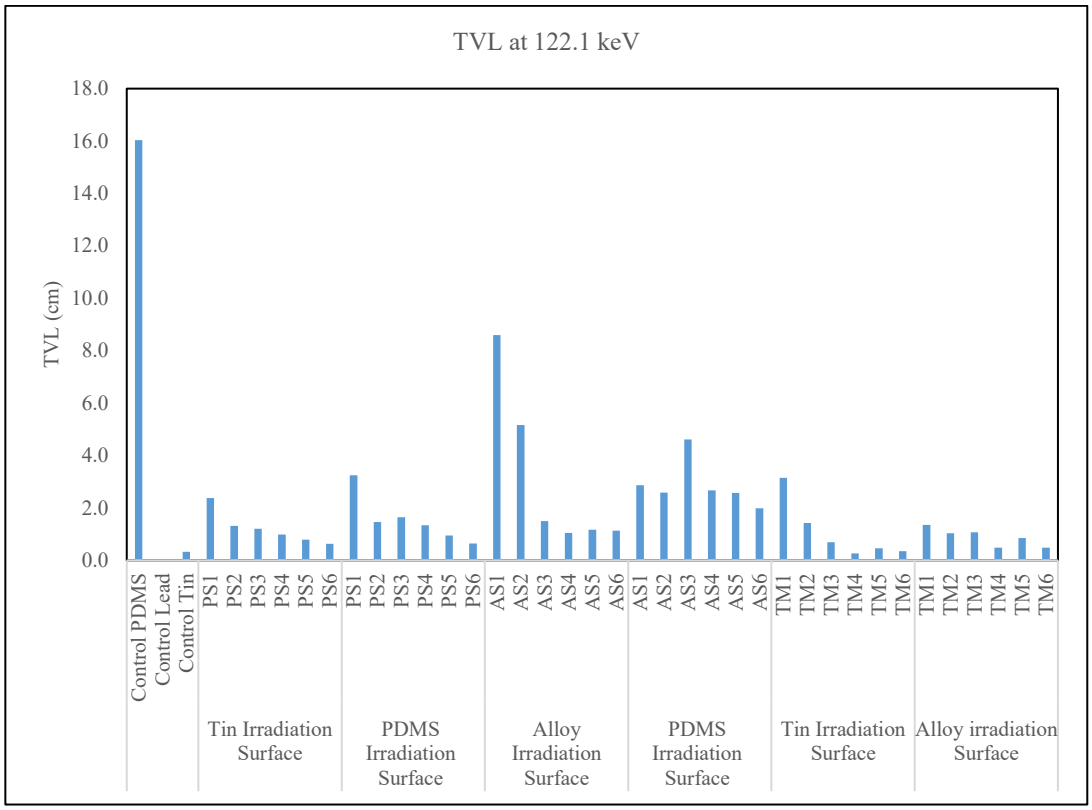


Figure 4.34 TVL of Fabricated Composite at 122.1 keV

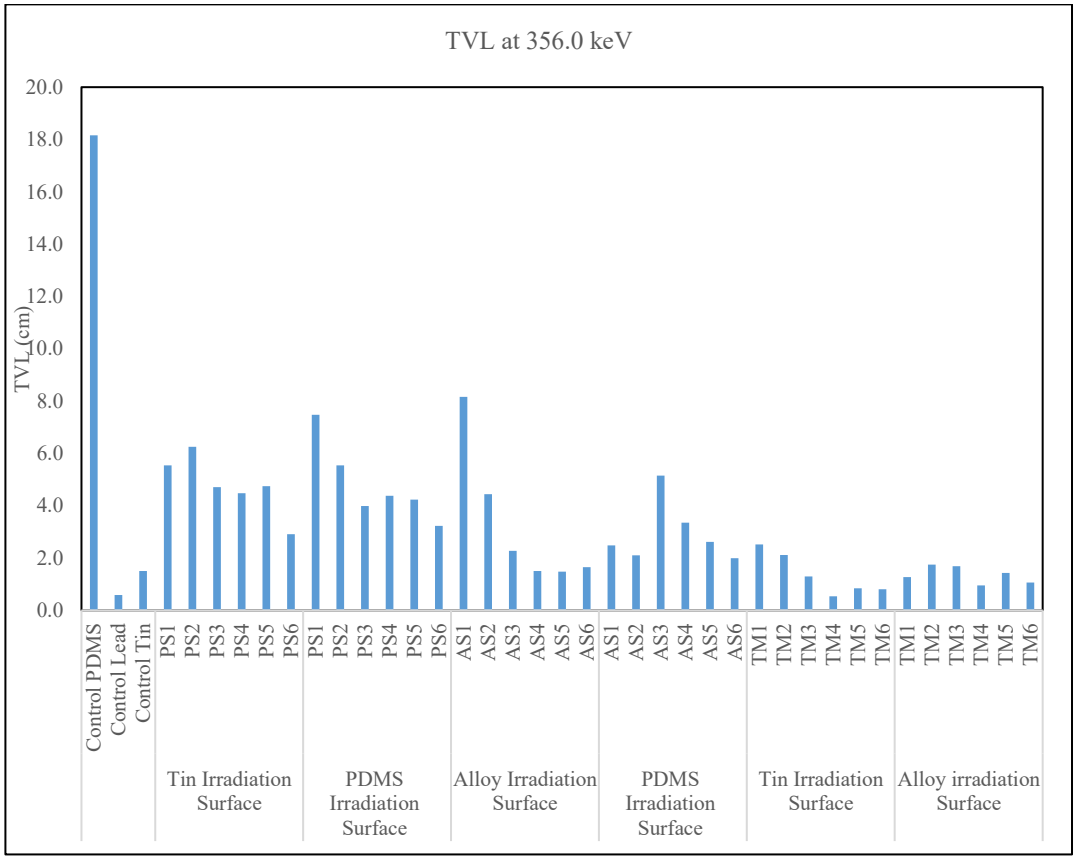


Figure 4.35 TVL of Fabricated Composite at 356.0 keV

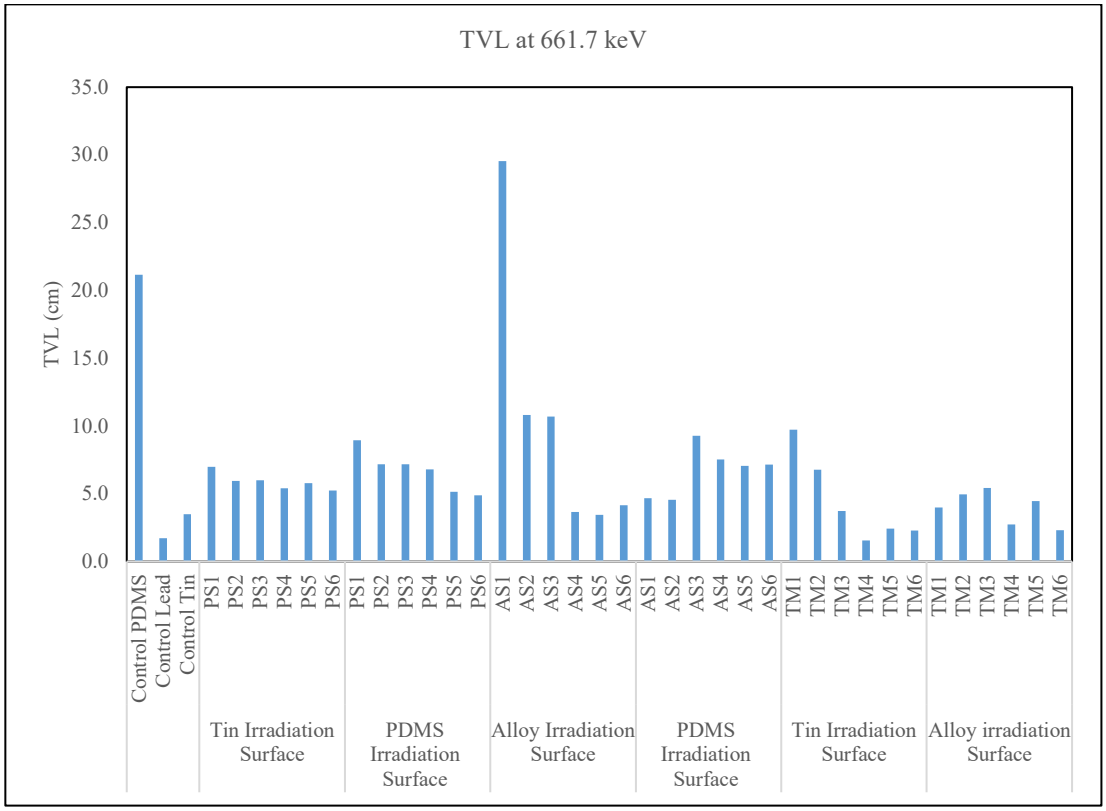


Figure 4.36 TVL of Fabricated Composite at 661.7 keV

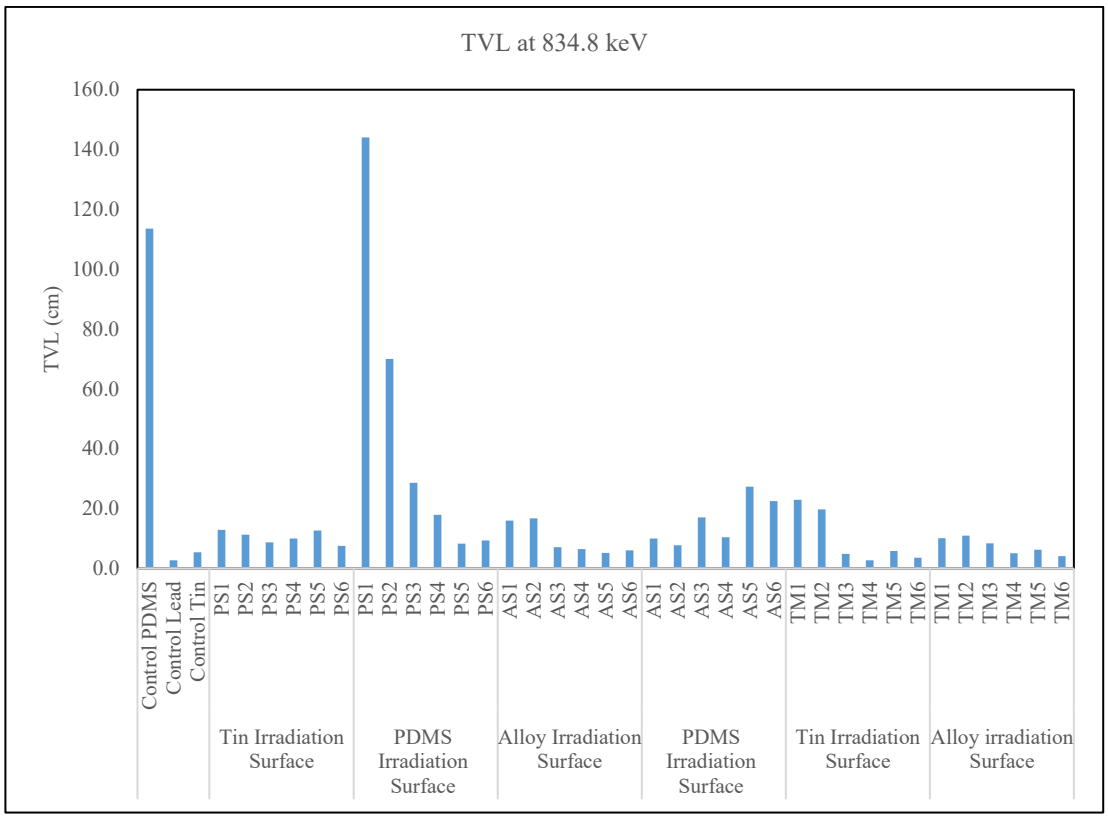


Figure 4.37 TVL of Fabricated Composite at 834.8 keV

Overall, the TVL curves illustrate a clear hierarchy of shielding performance. Lead remains the benchmark, PDMS performs poorest, PS composites deliver strong low-energy attenuation but weaken rapidly with energy, AS composites provide improved mid-range balance, and TM composites, TM4 and TM6, achieve near-lead attenuation with stable, low-energy dependence. The alloy–TM variants further enhance smoothness and consistency, making them highly promising candidates for lead-free, lightweight, and stable gamma-shielding applications.

### 4.7.5 Radiation Protection Efficiency

The RPE results presented in Table 4.9 provide a comprehensive comparison of the attenuation capabilities of the control samples, single filler composites (PS and AS series), and a mix of pure tin and tin alloy filler composites (TM series) across different irradiation surfaces and photon energies ranging from 88.0 to 834.8 keV.

The control samples display the expected baseline behaviour. Lead, as the high-density standard, demonstrates complete shielding at low photon energies, maintaining 100.00% efficiency at 88.0 and 122.1 keV before dropping sharply to 87.08% at 356.0 keV, 48.86% at 661.7 keV, and 35.02% at 834.8 keV. Tin follows a similar but weaker trend, with 100% at 88.0 keV and 96.99% at 122.1 keV, showing a faster decline to 53.57% at 356.0 keV, 28.17% at 661.7 keV, and 19.09% at 834.8 keV. In contrast, PDMS performs poorly across the entire spectrum, with only 12.06% at 88.0 keV, 7.19% at 122.1 keV, and less than 2% at the highest energy (1.04% at 834.8 keV), confirming its intrinsic inadequacy as a shielding medium due to its low density and lack of high-density elements (Domenech, 2017).

The PS series (tin irradiation surface) shows marked improvement over untreated PDMS, with efficiencies ranging from 40.84% (PS1 at 88.0 keV) to 86.02% (PS5 at 88.0 keV). At 122.1 keV, PS5 and PS6 performed best with 55.70% and 55.09% respectively, but values declined with increasing energy, reaching 12.718–15.90% at 356.0 keV, 9.21–10.57% at 661.7 keV, and only 4.37–6.50% at 834.8 keV.

On PDMS irradiation surfaces, the trend is similar but with slightly lower values: PS samples range from 30.08–69.19% at 88.0 keV, 16.86 – 49.44% at 122.1 keV and fall to 0.41–6.74% at 834.8 keV. These results confirm that tin irradiation surface enhances photon interaction at lower energies, but attenuation capacity decreases steeply at higher energies, limiting their broad-spectrum effectiveness

(Akhdar, 2025). The AS series (alloy irradiation surface) demonstrates a more gradual improvement in RPE compared to the PS series. AS1 begins at 13.33% at 88.0 keV and increases progressively to 50.55% in AS6 at the same energy. At mid-energies, AS6 maintains stronger attenuation than the PS series, reaching 26.44% at 356.0 keV and 11.46% at 661.7 keV, though still falling to 7.99% at 834.8 keV.

When alloy irradiation is applied to PDMS surfaces, the performance is moderate, with RPE ranging from 14.19% (AS1) to 43.38% (AS4) at 88.0 keV. Importantly, some samples retain better mid-energy stability, such as AS6, which achieves 34.03% at 356.0 keV. This indicates that alloy-treated PDMS composites offer a more balanced attenuation profile compared to pure tin treatments, showing less severe decline across the mid-energy range while still improving significantly over untreated PDMS (Akhdar, 2025).

The TM series (tin irradiation surface) exhibits the highest overall performance and underscores the advantage of dual-filler strategies. Efficiencies for this series start at 32.83% for TM1 at 88.0 keV and reach a maximum of 96.53% for TM6 at the same energy. More importantly, TM6 maintains high attenuation across the energy spectrum: 72.79% at 122.1 keV, 43.54% at 356.0 keV, 18.32% at 661.7 keV, and 11.98% at 834.8 keV. The strong retention of efficiency at high photon energies distinguishes TM6 from both the PS and AS series. Earlier TM samples (TM1 – TM3) show lower stability, but as filler optimisation improves in TM4 – TM6, performance becomes consistent and far superior to single-filler systems.

A similar trend is observed for the alloy irradiation of metallic matrix composites. TM1 begins at 48.29% at 88.0 keV and progresses to 91.17% in TM6 at the same energy. TM6 further demonstrates robust mid and high energy attenuation with 69.57% at 122.1 keV, 41.76% at 356.0 keV, 22.05% at 661.7 keV, and 13.09% at 834.8 keV. Compared to the tin irradiated TM series, the alloy irradiated TM composites show smoother energy dependence and slightly higher stability at elevated energies. This highlights the synergistic effect of combining irregular tin and spherical tin alloy particles, which improves packing density and enhances photon–matter interactions across a broader energy range (Akhdar, 2025; Domenech, 2017).

Table 4.9
RPE Values at Different Gamma Energies for Different Irradiation Surfaces.

| Surface irradiation | Samples | RPE (%) | | | | |
|---|---|---|---|---|---|---|
| | | **88.0 keV** | **122.1 keV** | **356.0 keV** | **661.7 keV** | **834.8 keV** |
| Control | Control PDMS | 12.06 | 7.19 | 6.37 | 5.50 | 1.04 |
| | Control Lead | 100.00 | 100.00 | 87.07 | 48.86 | 35.02 |
| | Control Tin | 100.00 | 96.99 | 53.57 | 28.17 | 19.09 |
| Tin Irradiation Surface | PS1 | 40.84 | 21.44 | 9.87 | 7.90 | 4.37 |
| | PS2 | 64.14 | 33.21 | 8.11 | 8.51 | 4.58 |
| | PS3 | 64.43 | 36.72 | 11.08 | 8.80 | 6.13 |
| | PS4 | 70.95 | 38.63 | 10.24 | 8.56 | 4.73 |
| | PS5 | 86.02 | 55.70 | 12.71 | 10.57 | 4.97 |
| | PS6 | 80.19 | 55.09 | 15.95 | 9.21 | 6.50 |
| PDMS Irradiation Surface | PS1 | 30.08 | 16.86 | 7.70 | 6.47 | 0.41 |
| | PS2 | 59.64 | 32.59 | 9.87 | 7.69 | 0.81 |
| | PS3 | 51.76 | 29.56 | 13.42 | 7.71 | 1.99 |
| | PS4 | 59.72 | 34.80 | 12.32 | 8.11 | 3.15 |
| | PS5 | 69.19 | 45.58 | 12.73 | 10.59 | 6.74 |
| | PS6 | 57.06 | 49.44 | 12.68 | 8.56 | 4.57 |
| Alloy irradiation Surface | AS1 | 13.33 | 10.09 | 11.92 | 6.66 | 4.21 |
| | AS2 | 20.06 | 13.69 | 15.71 | 6.78 | 4.43 |
| | AS3 | 28.18 | 25.43 | 18.32 | 7.40 | 4.16 |
| | AS4 | 55.37 | 29.50 | 21.81 | 9.59 | 5.50 |
| | AS5 | 36.72 | 29.86 | 24.39 | 11.36 | 7.73 |
| | AS6 | 50.55 | 36.04 | 26.44 | 11.46 | 7.99 |
| PDMS Irradiation Surface | AS1 | 14.19 | 9.92 | 11.36 | 6.19 | 2.93 |
| | AS2 | 15.08 | 10.92 | 13.26 | 6.36 | 3.77 |
| | AS3 | 20.65 | 17.26 | 15.62 | 9.00 | 4.99 |
| | AS4 | 43.38 | 25.34 | 20.81 | 9.87 | 7.20 |
| | AS5 | 36.34 | 25.50 | 25.18 | 10.20 | 2.74 |
| | AS6 | 33.29 | 34.02 | 34.03 | 10.95 | 3.61 |
| Tin Irradiation Surface | TM1 | 32.83 | 20.26 | 24.73 | 7.08 | 3.06 |
| | TM2 | 65.37 | 39.38 | 28.62 | 10.00 | 3.56 |
| | TM3 | 73.14 | 48.51 | 30.04 | 11.63 | 9.10 |
| | TM4 | 94.76 | 63.69 | 40.40 | 16.26 | 9.60 |
| | TM5 | 92.83 | 59.00 | 38.70 | 15.76 | 6.92 |
| | TM6 | 96.53 | 72.79 | 43.54 | 18.32 | 11.98 |
| Alloy irradiation Surface | TM1 | 48.29 | 21.16 | 22.41 | 7.75 | 3.15 |
| | TM2 | 66.51 | 39.85 | 26.09 | 10.13 | 4.72 |
| | TM3 | 73.83 | 49.78 | 35.50 | 12.70 | 8.39 |

| | | | | | |
|---|---|---|---|---|---|
| TM4 | 85.13 | 61.29 | 38.31 | 15.55 | 8.75 |
| TM5 | 87.47 | 58.98 | 41.36 | 15.68 | 11.39 |
| TM6 | 91.17 | 69.57 | 41.76 | 22.05 | 13.09 |

Taken together, the RPE results establish a clear performance hierarchy. Lead and tin controls dominate at low energies but lose efficiency quickly with increasing photon energy, while PDMS remains ineffective across all ranges. The PS series improves low-energy performance but suffers from poor high-energy stability due to morphological limitations. The TM series, particularly TM6, combines the advantages of both, delivering near-lead performance at low energies (96.53% at 88.0 keV) while retaining measurable attenuation at 834.8 keV (11.98–13.09%). This dual-filler metallic matrix approach represents the most promising pathway toward practical lead-free shielding, offering a balance of efficiency, stability, and reduced toxicity (Dai et al., 2016; Kwon et al., 2023; Nakamura et al., 2024b; Roslan et al., 2025; Safari et al., 2024). The RPE trends illustrated in Figures 4.31 to 4.33 complement the numerical results of Table 4.8 by providing a clear visualisation of how shielding performance evolves with increasing photon energy.

The RPE trends illustrated in Figures 4.38 to 4.42 visually complement the numerical findings of Table 4.12, providing a clearer depiction of how shielding performance evolves with increasing photon energy. The plotted curves establish the expected hierarchy: lead exhibits the highest attenuation efficiency at low energies, followed closely by tin, while PDMS remains at the lowest level throughout due to its low mass attenuation coefficient. The wide separation between the curves at 88.0 keV and 122.1 keV reflects the dominance of photoelectric absorption in the low-energy regime (Alanazi et al., 2024b).

As energy increases, the curves gradually converge, illustrating the diminishing advantage of atomic number in the Compton scattering domain (Bisht et al., 2025). However, the composites do not collapse to the same baseline. PS series composites maintain clear superiority over untreated PDMS at low energies, though its rapid decline with increasing keV is evident in the steep downward slope of the plotted lines. The AS series shows more gradual declines, with some curves, such as AS6, retaining visibly higher mid-energy stability than the tin irradiation surface. This behaviour highlights the contribution of alloying to filler dispersion and photon interaction, which is less apparent from tabulated values alone.

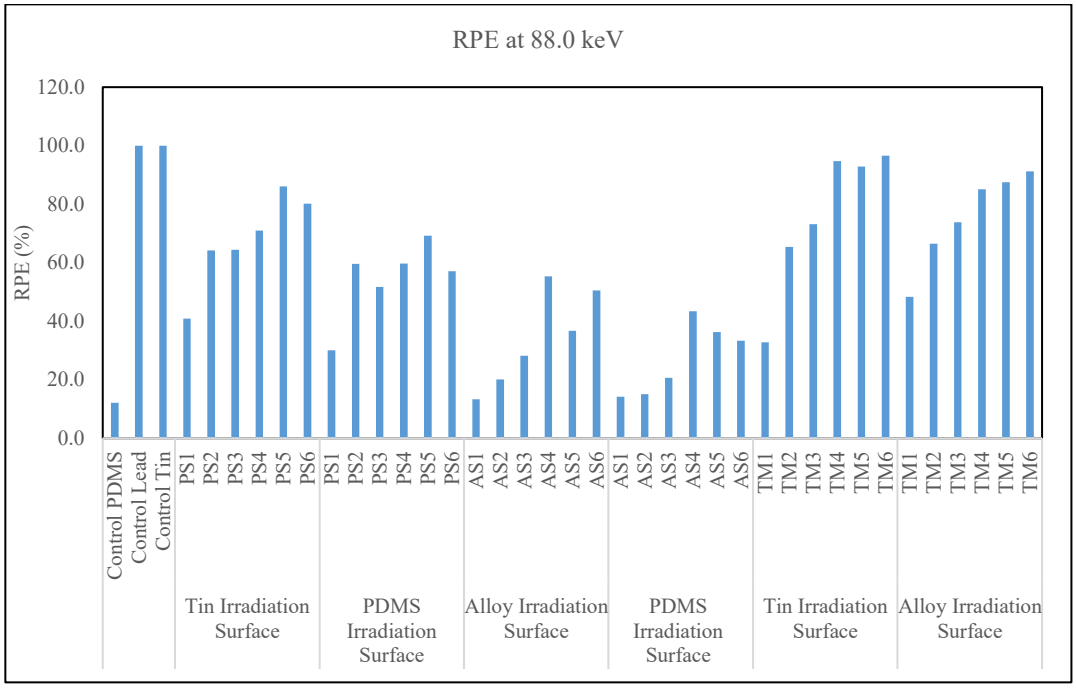


Figure 4.38 RPE of Fabricated Composite at 88.0 keV

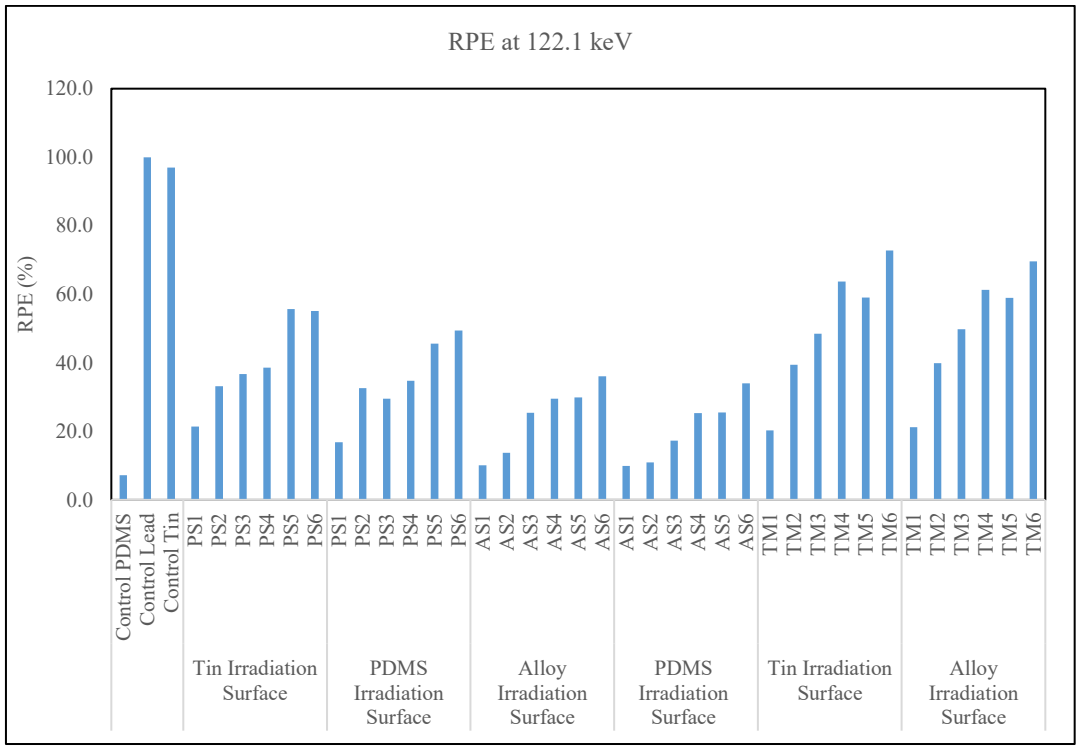


Figure 4.39 RPE of Fabricated Composite at 122.1 keV

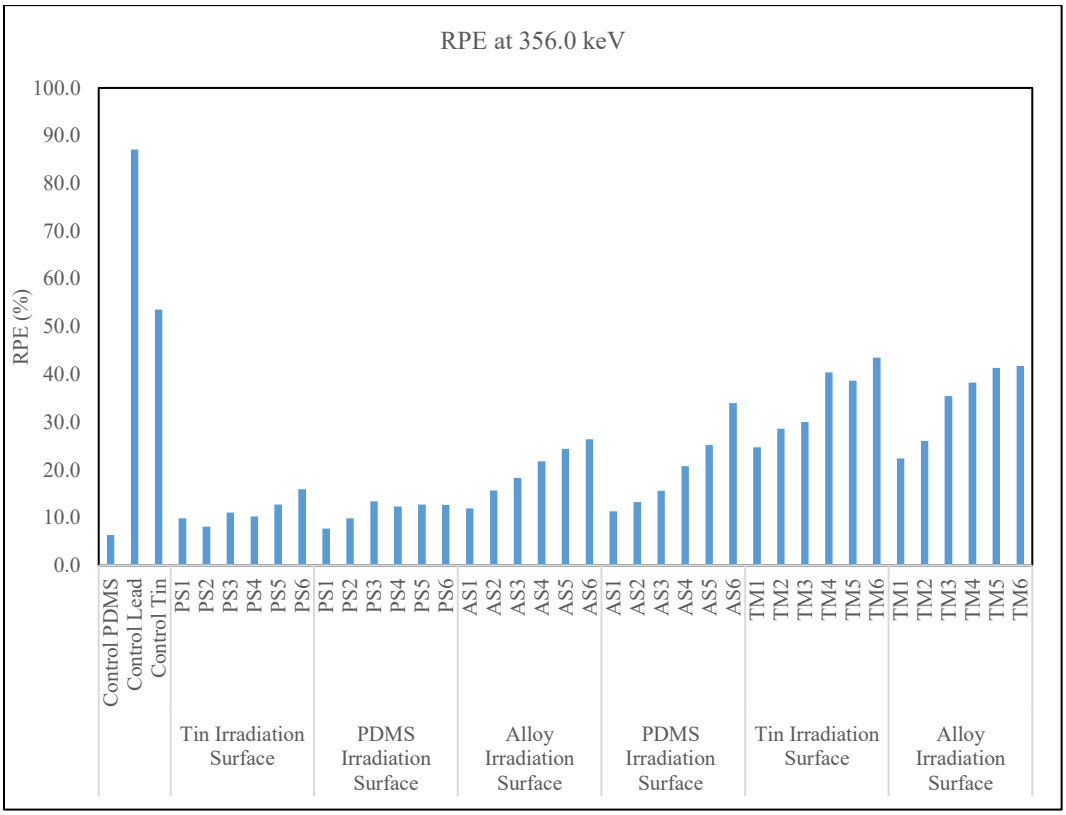


Figure 4.40 RPE of Fabricated Composite at 356.0 keV

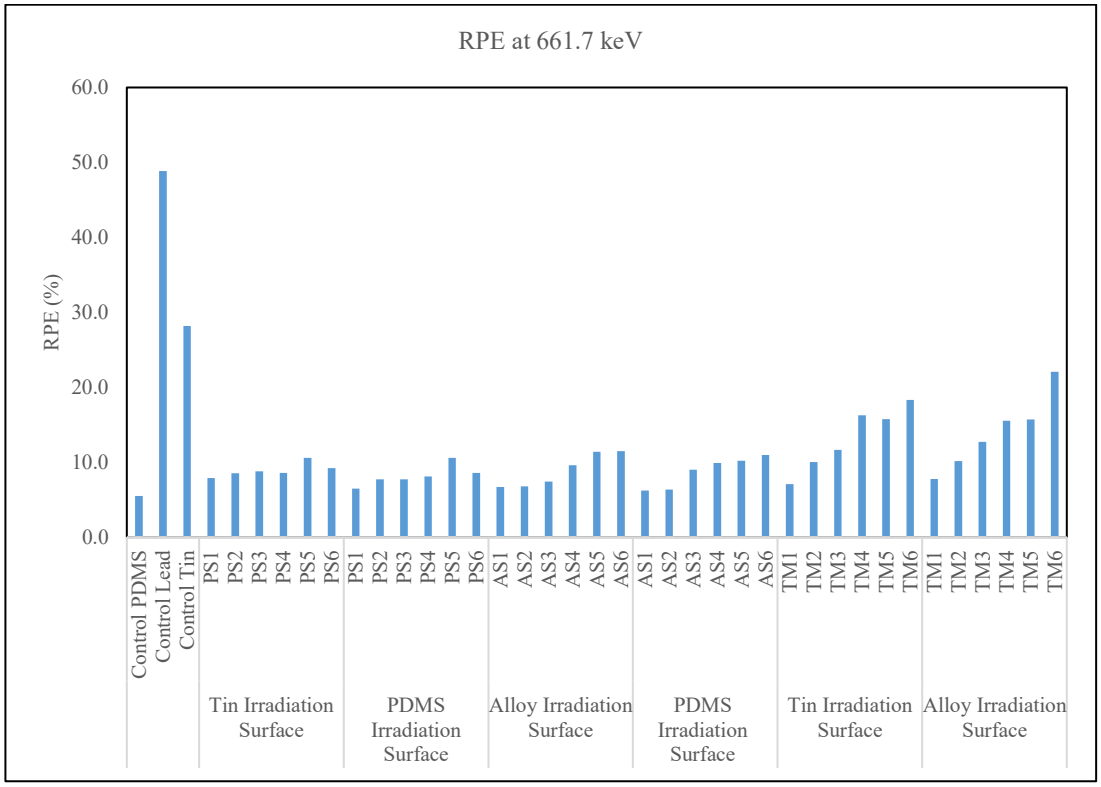


Figure 4.41 RPE of Fabricated Composite at 661.7 keV

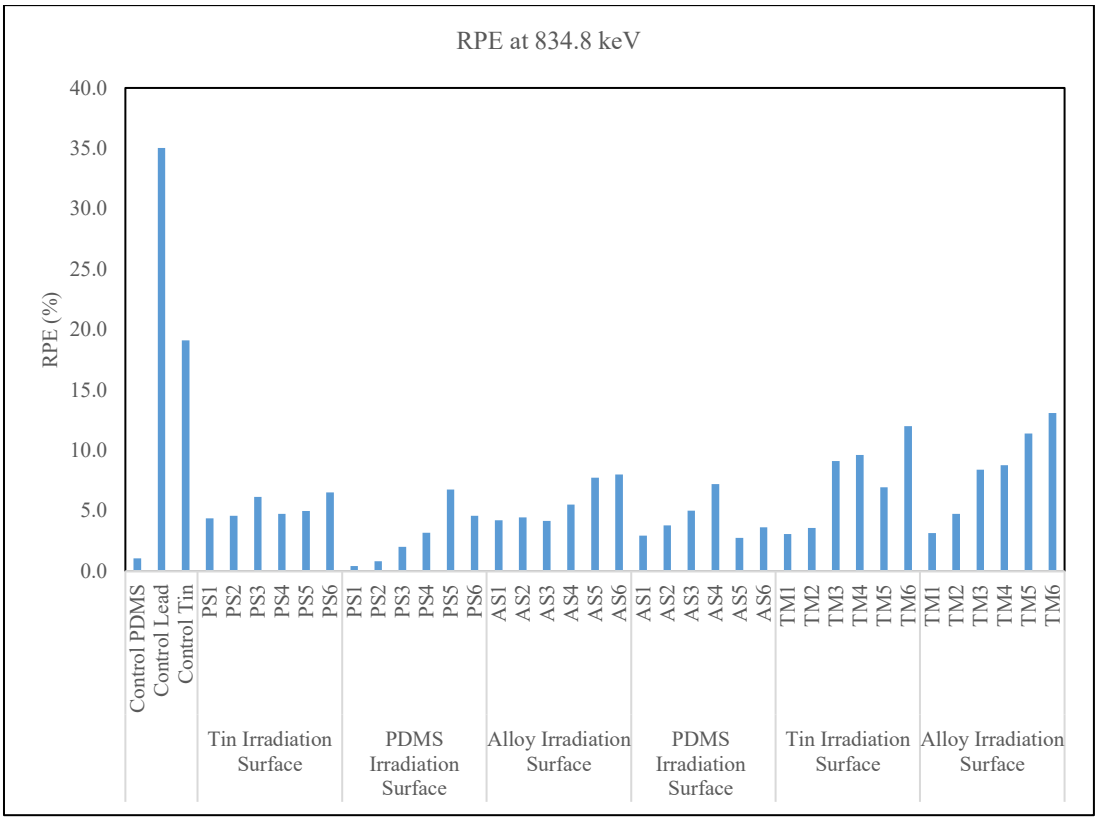


Figure 4.42 RPE of Fabricated Composite at 834.8 keV

The most striking feature of the plotted curves is the consistent separation of the TM series, especially TM4, TM5, and TM6, from all other non-lead systems. Taken together, the plotted curves confirm and extend the tabulated findings.

While the table establishes clear numerical hierarchies, the graphs reveal deeper insights into how layer orientation, filler type, and composite morphology govern the shape of attenuation behaviour across photon energies. The wide separation at low energies, curve convergence at higher energies, and persistent superiority of dual-filler TM composites collectively reinforce the practical importance of strategic material design in achieving lead-free, broad-spectrum radiation shielding.

When the results from all tables and graphs are considered together, several important conclusions emerge. The composition and arrangement of layers within a composite are critical determinants of gamma-ray shielding performance. Placing a high-density material such as tin at the radiation-facing surface consistently improves attenuation by maximising photoelectric interactions before photons reach lower-density layers.

The attenuation performance of all materials decreases with increasing photon energy, following well-established theoretical principles of photon–matter interactions, with photoelectric absorption dominating at low energies, Compton scattering at intermediate energies, and pair production at very high energies. Pure metals such as lead and tin remain the most effective shields, bilayer composites offer an appealing balance between performance, weight, and flexibility, making them suitable for practical applications where mobility and mechanical adaptability are important, such as in PPE for medical or industrial workers and in aerospace radiation shielding (Kwon et al., 2023).

The integration of the tabulated data with the graphical trends allows for a clearer understanding of the energy-dependent shielding behaviour and the effectiveness of different material configurations. The tables provide precise numerical values for direct reference, while the graphs illustrate the overall patterns and highlight the differences between configurations in a way that is easily interpretable. This combination strengthens the presentation of the results and provides a comprehensive foundation for discussing both the theoretical and practical implications of the findings (Akhdar, 2025).

## 4.8 Radiation Properties for the Best Optimised Samples

The optimised samples from each series, namely PS6, AS6 and TM6, were selected for detailed discussion. These samples represent the highest metal filler loading (60 wt%) investigated in the present study. The selection was based on the overall radiation shielding performance, considering the collective behaviour of the attenuation parameters together with the physical characteristics of the composites at a specific photon energy.

Although TM4 exhibited the highest LAC and MAC with the lowest HVL and TVL at 88 keV, TM6 demonstrated the highest RPE, achieving 96.83% attenuation of the incident photons. In addition, TM6 possessed the highest effective density of 5.32 g/cm³ and the lowest effective density percentage difference of 0.94%, indicating better material homogeneity and fabrication consistency when compared to TM4 with 1.91% percentage difference. Minor differences between the attenuation coefficients and RPE are considered to arise from experimental uncertainties associated with specimen geometry, such as slight variations in the measured sample thickness and exposed

measurement area, which directly influence the calculated attenuation coefficients. Consequently, TM6 was selected as the representative optimised sample for the TM series because it exhibited superior overall shielding performance when all evaluation criteria were considered collectively.

Following this justification, the radiation shielding properties of the optimised samples (PS6, AS6 and TM6) at 60 wt% metal filler loading are discussed in detail. Table 4.10 summarises the radiation shielding parameters for the optimised composites at low (88.0 keV), moderate (356.0 keV), and high (834.8 keV) photon energies, benchmarked against control materials: PDMS, tin, and lead. The parameters include the LAC, MAC, RPE, HVL, and TVL. Together, these indicators describe the fundamental interaction processes between gamma photons and the composite materials, reflecting both their attenuation capability and material efficiency across energy ranges (Domenech, 2017).

At 88.0 keV, where photoelectric absorption dominates, the effect of high atomic number constituents is most pronounced. As expected, lead and tin achieved complete attenuation (RPE = 100%) with zero HVL and TVL, confirming their benchmark performance. In contrast, pure PDMS exhibited poor shielding (RPE = 12.06%), with very low LAC (0.247 $cm^{-1}$) and a large HVL (2.8029 cm), indicating weak photon absorption due to its low atomic number composition (Domenech, 2017).

Among the composites, TM6 (tin irradiation surface) demonstrated the highest attenuation, achieving a LAC of 16.811 $cm^{-1}$ and MAC of 3.160 $cm^2\ g^{-1}$, corresponding to RPE = 96.53%, HVL = 0.0412 cm, and TVL = 0.137 cm. These values closely approach those of lead, confirming that TM6 provides near-complete attenuation at low energy while maintaining a flexible, lead-free structure. The alloy-irradiated TM6 also performed excellently, with LAC = 9.711 $cm^{-1}$, MAC = 1.825 $cm^2\ g^{-1}$, RPE = 91.17%, HVL = 0.0714 cm, and TVL = 0.237 cm, slightly lower in absolute efficiency but exhibiting smoother and more stable attenuation behaviour.

PS6 (tin irradiation surface) recorded moderate efficiency (LAC = 7.360 $cm^{-1}$, RPE = 80.19%), while AS6 (alloy irradiation surface) performed less strongly (LAC = 3.202 $cm^{-1}$, RPE = 50.55%), though still markedly better than pure PDMS. The improvement in PS6 and TM6 over PDMS demonstrates the dominant role of tin and copper atoms in photoelectric absorption at low photon energies. Overall, the data confirm that low-energy gamma attenuation is primarily affected by atomic number and

density, with TM6 achieving the highest performance among all lead-free systems (Nambiar & Yeow, 2012).

At 356.0 keV, photon interactions are dominated by the Compton scattering process, which depends less on atomic number and more on material electron density. As expected, all samples show reduced LAC and RPE compared with the low-energy regime. Lead maintained the best performance (LAC = 3.935 $cm^{-1}$, MAC = 0.3470 $cm^2$ $g^{-1}$, RPE = 87.07%, HVL = 0.1762 cm, TVL = 0.585 cm), followed by tin (LAC = 1.534 $cm^{-1}$, RPE = 53.57%).

Among composites, TM6 (tin irradiation surface) exhibited the highest attenuation (LAC = 2.858 $cm^{-1}$, MAC = 0.5373 $cm^2$ $g^{-1}$, RPE = 43.54%), along with very low HVL (0.2425 cm) and TVL (0.806 cm), indicating strong mid-energy performance. The alloy-irradiated TM6 also performed effectively (LAC = 0.638 $cm^{-1}$, RPE = 41.76%), maintaining consistent shielding efficiency with a slightly higher HVL (0.3205 cm).

AS6 and PS6 displayed moderate attenuation (LAC = 1.396 $cm^{-1}$ and 0.790 $cm^{-1}$, respectively), corresponding to RPE = 26.44% for AS6 and 15.95% for PS6. Although these are lower than TM6, both composites significantly outperform PDMS, which recorded only LAC = 0.127 $cm^{-1}$, RPE = 6.37%, and a large HVL of 5.4677 cm. The moderate-energy results therefore emphasise the beneficial effect of dual fillers in TM6, where both tin and tin alloy contribute complementary scattering mechanisms, enhancing mid-energy gamma attenuation.

At 834.8 keV, pair production begins to contribute, although Compton scattering remains the dominant interaction. Under these high-energy conditions, all materials show reduced attenuation due to the higher photon penetration depth. Lead again achieved the best performance (LAC = 0.862 $cm^{-1}$, MAC = 0.0761 $cm^2$ $g^{-1}$, RPE = 35.02%, HVL = 0.8037 cm, TVL = 2.670 cm), followed by tin (LAC = 0.424 $cm^{-1}$, RPE = 19.09%)Among composites, TM6 (tin irradiation surface) retained the strongest high-energy shielding with LAC = 0.638 $cm^{-1}$, MAC = 0.1200 $cm^2$ $g^{-1}$, RPE = 11.98%, HVL = 1.0857 cm, and TVL = 3.607 cm. The alloy-irradiated TM6 performed comparably (LAC = 0.561 $cm^{-1}$, RPE = 13.09%, HVL = 1.2345 cm, TVL = 4.101 cm), indicating stable attenuation at high photon energies with smoother response curves than tin irradiation surface.

Table 4.10
Radiation Properties of The Optimised Samples at Low Energy (88.0 keV), Moderate Energy (356.0 keV), and High Energy (834.8 keV)

| Energy (keV) | Shielding parameter | Sample - Surface irradiation surface | | | | | | |
|---|---|---|---|---|---|---|---|---|
| | | PDMS | Lead | Tin | PS6-Tin | AS6-Alloy | TM6-Tin | TM6-Alloy |
| 88.0 | LAC ($cm^{-1}$) | 0.247 | 0 | 0 | 7.360 | 3.202 | 16.811 | 9.711 |
| | MAC ($cm^2\ g^{-1}$) | 0.257 | 0 | 0 | 2.337 | 0.936 | 3.160 | 1.825 |
| | RPE (%) | 12.07 | 100 | 100 | 80.19 | 50.56 | 96.53 | 91.17 |
| | HVL (cm) | 2.803 | 0 | 0 | 0.094 | 0.217 | 0.041 | 0.071 |
| | TVL (cm) | 9.311 | 0 | 0 | 0.313 | 0.719 | 0.137 | 0.237 |
| 356.0 | LAC ($cm^{-1}$) | 0.127 | 3.935 | 1.534 | 0.790 | 1.396 | 2.858 | 0.638 |
| | MAC ($cm^2\ g^{-1}$) | 0.132 | 0.347 | 0.210 | 0.250 | 0.408 | 0.537 | 0.407 |
| | RPE (%) | 6.37 | 87.07 | 53.57 | 15.95 | 26.44 | 43.54 | 41.76 |
| | HVL (cm) | 5.4677 | 0.1762 | 0.4517 | 0.8776 | 0.4965 | 0.243 | 0.321 |
| | TVL (cm) | 18.163 | 0.585 | 1.501 | 2.915 | 1.649 | 0.806 | 1.065 |
| 834.8 | LAC ($cm^{-1}$) | 0.020 | 0.862 | 0.424 | 0.306 | 0.379 | 0.638 | 0.561 |
| | MAC ($cm^2\ g^{-1}$) | 0.0211 | 0.0761 | 0.0581 | 0.0970 | 0.1108 | 0.1200 | 0.106 |
| | RPE (%) | 1.04 | 35.02 | 19.09 | 6.50 | 7.99 | 11.98 | 13.09 |
| | HVL (cm) | 34.197 | 0.8037 | 1.6354 | 2.2685 | 1.829 | 1.0857 | 1.2345 |
| | TVL (cm) | 113.60 | 2.670 | 5.433 | 7.536 | 6.076 | 3.607 | 4.101 |

AS6 showed moderate efficiency (LAC = 0.379 $cm^{-1}$, RPE = 7.99%), outperforming PS6 (LAC = 0.306 $cm^{-1}$, RPE = 6.50%), while PDMS remained ineffective (LAC = 0.020 $cm^{-1}$, RPE = 1.04%). Although absolute attenuation decreases at higher energy for all composites, TM6 maintains the lowest HVL and TVL among the lead-free materials, confirming its superior capacity to slow and scatter high-energy photons through multiple interaction mechanisms.

At low energy (88.0 keV), TM6 composites rival lead in performance, primarily due to dominant photoelectric absorption facilitated by high-density tin and copper atoms. At moderate energy (356.0 keV), TM6 maintains effective attenuation through enhanced Compton scattering supported by dense filler networks. At high energy (834.8 keV), although all materials show reduced attenuation, TM6 continues to outperform other lead-free composites, achieving the lowest HVL and TVL values.

In contrast, PS6 exhibits strong low-energy shielding but declines sharply at higher energies, while AS6 provides more stable mid-energy attenuation, likely due to improved filler dispersion and alloy morphology (Zainal Abidin, Mukhtar, Mahmood, Abdul Wahab, Zainon, Roslan, et al., 2025). The TM6 composites, especially under tin irradiation, combine both benefits: high atomic contribution and efficient layer interaction, resulting in consistent and high performance across all energies.

Overall, Table 4.9 conclusively demonstrates that the dual-filler TM6 composites are the most effective lead-free shielding materials, achieving near-lead attenuation at low energies and sustainable performance at moderate and high energies. The inclusion of alloy interfaces further improves the uniformity and stability of photon interactions, establishing TM6 as an optimal design for lightweight, flexible, and efficient radiation protective materials suitable for PPE and structural shielding applications.

### 4.8.1 Comparison of Radiation Shielding Performance with Previous Findings

Table 4.11 summarises and compares the radiation shielding parameters of the present PS series and AS series composites with previous studies involving metal or metal oxide fillers in PDMS and other polymer matrices. The data encompass different fabrication techniques (mixing, casting, doping, roll milling, and layering), metal loadings, thicknesses, and photon energy ranges. Collectively, this comparison establishes the performance benchmark of the developed composites and highlights the contribution of the layering approach to achieving high attenuation efficiency using lead-free materials.

Earlier research focused primarily on $SnO_2$, ZnO, $Bi_2O_3$, and PbO-based PDMS composites prepared through mixing and curing (Showahy et al., 2022), (Aladailah et al., 2022). These studies generally reported LAC values between 0.059 and 1.332 $cm^{-1}$ and RPE between 16 and 98%, depending on metal concentration and energy level.

Although these composites achieved acceptable shielding at low photon energies (<0.2 MeV), their efficiency dropped significantly at moderate and high energies due to random filler dispersion and limited interfacial photon absorption.

Similarly, (Nazeri et al., 2025) and (El-Khatib, Zard, et al., 2024b) demonstrated that combining multiple high-density oxides ($Bi_2O_3$, $WO_3$, $SnO_2$) improved attenuation, but the results remained strongly dependent on filler ratio, particle size, and uniformity within the polymer network. The layering method, as reported in (Gilys et al., 2022) and (Kwon et al., 2023), introduced an alternative approach by arranging high-density layers sequentially within a flexible matrix.

This architecture improved photon–electron interactions by allowing sequential attenuation, where each layer contributes to a different dominant interaction process (photoelectric, Compton, and pair production). However, that previous multilayer composite primarily used tungsten or bismuth with high densities and reduced elasticity.

The present study extends the concept of layered design to tin-PDMS composites, creating both pure tin and tin alloy configurations with controlled layer orientation and different irradiation surfaces such as tin irradiation surface and alloy irradiation surface, including PDMS irradiation surface. Across all energies, 0.088 MeV (low), 0.356 MeV (moderate), and 0.834 MeV (high). The results demonstrate superior performance compared with earlier Sn–PDMS systems produced by simple mixing or curing.

For the tin-PDMS layered composite, the LAC values reached 7.360 $cm^{-1}$, 0.790 $cm^{-1}$, and 0.306 $cm^{-1}$ at the respective energies, with corresponding RPE values of 80.19%, 15.95%, and 6.50%. These results already exceed or match prior $SnO_2$–PDMS composites (Showahy et al., 2022), (El-Khatib, Zard, et al., 2024b), which exhibited maximum LAC of ~3.2 $cm^{-1}$ and RPE of only 16 and 17%.

When the tin irradiation surface was oriented toward the gamma source, performance improved markedly: LAC increased to 16.811 $cm^{-1}$ at 0.088 MeV, with RPE up to 96.53%, approaching that of traditional lead-based shields. The introduction of tin alloy layers further enhanced photon absorption and scattering balance. The TM series achieved LAC values of 3.202–0.379 $cm^{-1}$ and RPE between 50.55–7.99%, outperforming most oxide-based PDMS composites at similar thicknesses. The dual-layered TM series orientation tin irradiation surface and alloy irradiation surface structures achieved even higher attenuation due to layered density gradients, promoting stepwise energy loss of photons through multiple interactions. For instance, at 0.088

MeV, the TM series (tin irradiation surface) composite recorded LAC = 16.81 $cm^{-1}$, MAC = 3.160 $cm^2/g$, and RPE = 96.53%, surpassing most prior PDMS-based shields and approaching lead-equivalent performance.

The superior attenuation of the layered composites arises from the sequential interaction mechanism during photon penetration. When gamma photons encounter the high-density tin or tin alloy layer, photoelectric absorption dominates, removing low-energy photons and generating secondary electrons. As photons pass into the lower-density polymer layer, the energy is redistributed, and Compton scattering becomes the main interaction process, reducing photon energy and directionality. Subsequent reflections and scattering between layers increase the effective photon path length, resulting in higher overall absorption.

Table 4.11
Comparison with The Previous Study That Used Similar Sn and PDMS

| Ref. | Metal - Polymer | Fabrication Technique | Metal (%) | Thickness (cm) | Radiation Energy (MeV) | Radiation properties | | | | |
|---|---|---|---|---|---|---|---|---|---|---|
| | | | | | | LAC ($cm^{-1}$) | MAC ($cm^2 g^{-1}$) | HVL (cm) | TVL (cm) | RPE (%) |
| (Gilys et al., 2022) | Sn, $CeO_2$, $WO_3$, Bi - PDMS | Layering | 8.7<br>21.6<br>42.6<br>14.3 | 3.949 – 4.161 | 0.020 - 0.160 | 3.949 – 4.161 | 0.020 – 0.160 | 0.12 – 0.50 | 0 – 50 | 94-99 |
| (Gouda et al., 2023) | Nano-particle-$SnO_2$ - Si,<br>Micro-particle-$SnO_2$ - Si | Mixing and curing | 20, 50<br>20, 50 | 0.5 | 0.0596 - 1.408 | ~ 0.25-2.125, ~0.5-6.5<br>~0.25-1.625, ~0.5-~5.1 | 0.053 - 3.187 | 0.01-9 | 0.1-25 | 11-100 |
| (Aladailah et al., 2022) | ZnO - PDMS | Mixing and curing | 0<br>2.5<br>5<br>7.5<br>10<br>15 | 0.1-0.2 | 0.059 – 1.332 | 2.10 – 0.09 | 1.80 – 0.07 | 0.18 – 0.97 | 0.35 – 1.54 | 72 – 94 |
| (El-Khatib, Zard, et al., 2024b) | Micro-particle - $SnO_2$, CdO, $Bi_2O_3$ - PDMS<br>Nano-particle - $SnO_2$, | Mixing and curing | 0<br>20 | - | 0.05954 – 1.408 | 0.01-10 | 0.2186-0.0578<br>1.1663-0.0570 | 0.03 –10 | 0.10 – 35 | - |

| Ref. | Metal - Polymer | Fabrication Technique | Metal (%) | Thickness (cm) | Radiation Energy (MeV) | Radiation properties | | | | |
|---|---|---|---|---|---|---|---|---|---|---|
| | | | | | | LAC ($cm^{-1}$) | MAC ($cm^2 g^{-1}$) | HVL (cm) | TVL (cm) | RPE (%) |
| | CdO, $Bi_2O_3$ - PDMS | | 50 | | | | 2.5578-0.0537 | | | |
| (Nazeri et al., 2025) | $Bi_2O_3$, $WO_2$, $SnO_2$ - PDMS | Mixing and casting | - | 0.08 | 0.059 – 1.332 | 5.50 – 0.055 | 4.10 – 0.06 | 0.11 – 0.45 | 0.36 – 1.48 | - |
| (El-Khatib et al., 2022) | PbO - PDMS | Mixing and curing | 50 | 1.00 | 0.059–1.332 | 4.71 – 0.12 | 3.65 – 0.10 | 0.15 – 1.30 | 0.40 – 3.95 | 93 – 98 |
| (Yılmaz et al., 2020) | $Bi_2O_3$ - PDMS | Roll mill | 10<br>20<br>40 | 2.0<br>6.1-6.3<br>8.0-8.4 | 0.059 – 1.332 | 3.20 – 0.14 | 2.45 – 0.10 | 0.10 – 0.42 | 0.31 – 1.32 | 85 – 96 |
| (Kwon et al., 2023) | W, Bi, Sn, Te - TPU | Layering | - | 0.195-0.415 | 0.060-0.090 | 266.53<br>71.44<br>12.60<br>96.25 | - | 0.007-0.002 | - | 15 - 70 |
| (El-Khatib, Zard, et al., 2024a) | $CaCO_3$<br>Bi<br>W<br>$Bi_2WO_6$ - PDMS,TPV | Doping | - | 0.2-0.5 | 0.080 – 0.120 | 0.178 – 0.347 | 0.0182 – 0.0355 | 0.17-1.54 | - | - |
| Present | PS5 | Layering | 50 | 0.5 | 0.088<br>0.356<br>0.834 | 7.028<br>0.486<br>0.182 | 3.003<br>0.2076<br>0.0778 | 0.0986<br>1.427<br>3.807 | 0.3280<br>4.740<br>12.65 | 86.02<br>12.71<br>4.97 |

| Ref. | Metal - Polymer | Fabrication Technique | Metal (%) | Thickness (cm) | Radiation Energy (MeV) | Radiation properties | | | | |
|---|---|---|---|---|---|---|---|---|---|---|
| | | | | | | LAC ($cm^{-1}$) | MAC ($cm^2 g^{-1}$) | HVL (cm) | TVL (cm) | RPE (%) |
| | PS6 | Layering | 60 | 0.5 | 0.088 | 7.360 | 2.337 | 0.0942 | 0.313 | 80.19 |
| | | | | | 0.356 | 0.790 | 0.2507 | 0.8776 | 2.915 | 15.95 |
| | | | | | 0.834 | 0.306 | 0.0970 | 2.2685 | 7.536 | 6.50 |
| | AS5 | Layering | 50 | 0.5 | 0.088 | 2.543 | 0.818 | 0.2726 | 0.906 | 36.72 |
| | | | | | 0.356 | 1.553 | 0.4995 | 0.4462 | 1.482 | 24.39 |
| | | | | | 0.834 | 0.447 | 0.1438 | 1.549 | 5.147 | 7.73 |
| | AS6 | Layering | 60 | 0.5 | 0.088 | 3.202 | 0.936 | 0.2165 | 0.719 | 50.55 |
| | | | | | 0.356 | 1.396 | 0.4082 | 0.4965 | 1.649 | 26.44 |
| | | | | | 0.834 | 0.379 | 0.1108 | 1.829 | 6.076 | 7.99 |
| | TM5 | Layering | 50 | 0.5 | 0.088 | 6.295 - 14.64 | 1.342 - 3.122 | 0.1101 - 0.0473 | 0.366 - 0.157 | 87.47 - 92.83 |
| | | | | | 0.356 | 1.618 - 2.719 | 0.3449 - 0.5798 | 0.4285 - 0.2549 | 1.423 - 0.847 | 41.36 - 38.7 |
| | | | | | 0.834 | 0.367 - 0.399 | 0.0782 - 0.085 | 1.89 - 1.738 | 6.279 - 5.773 | 11.39 - 6.92 |
| | TM6 | Layering | 60 | 0.5 | 0.088 | 9.7111 - 16.81 | 1.825 - 3.16 | 0.0714 - 0.0412 | 0.237 - 0.137 | 91.17 - 96.53 |
| | | | | | 0.356 | 2.163 - 2.858 | 0.4066 - 0.5373 | 0.3205 - 0.2425 | 1.065 - 0.806 | 41.76 - 43.54 |
| | | | | | 0.834 | 0.561 - 0.638 | 0.1055 - 0.12 | 1.235 - 1.0857 | 4.101 - 3.607 | 13.09 - 11.98 |

### 4.8.2 Lead Equivalent of Optimised Sample

The lead-equivalent thickness $t_{Pb}$ of the optimised metal filler composites was evaluated across photon energies ranging from 88.0 keV to 834.8 keV, as presented in Table 4.12. The $t_{Pb}$ value represents the equivalent thickness of lead required to provide the same radiation shielding as the tested composite, measured in millimeters of lead (mmPb) (Kamislioglu et al., 2025).

The lead equivalent can be calculated as Equation (4.1) (Kamislioglu et al., 2025), where the $t_{Pb}$ is lead equivalent thickness, $\mu_{sample}$ is LAC of the sample, $\mu_{lead}$ is LAC of the control lead, t refers to thickness, $\rho_{sample}$ refers to the density of the sample, and $\rho_{lead}$ refers to the density of the control lead. Lower $t_{Pb}$ indicates a greater shielding efficiency of the material.

$$t_{Pb} = \frac{\mu_{sample}}{\mu_{lead}} \times \frac{\rho_{sample}}{\rho_{lead}} \times t_{sample} \quad (4.1)$$

Table 4.12
Lead Equivalent Thickness of Optimised Metal Filler Composite

| Irradiation surface | Samples | tPb (mmPb) | | |
|---|---|---|---|---|
| | | 356.0 | 661.7 | 834.8 |
| Tin Irradiation Surface | PS4 | 0.10 | 0.25 | 0.21 |
| | PS5 | 0.14 | 0.33 | 0.23 |
| | PS6 | 0.23 | 0.37 | 0.40 |
| Alloy Irradiation Surface | AS4 | 0.48 | 0.58 | 0.50 |
| | AS5 | 0.55 | 0.70 | 0.73 |
| | AS6 | 0.62 | 0.72 | 0.77 |
| Tin Irradiation Surface | TM4 | 1.23 | 1.23 | 1.09 |
| | TM5 | 1.46 | 1.50 | 0.98 |
| | TM6 | 1.53 | 1.59 | 1.56 |
| Alloy Irradiation Surface | TM4 | 0.69 | 0.70 | 0.59 |
| | TM5 | 0.87 | 0.81 | 0.90 |
| | TM6 | 1.16 | 1.57 | 1.37 |

At photon energies of 88.0 keV and 122.1 keV, all samples recorded a tPb value of 0 mmPb. This result occurred because the LAC of the control lead sample was either zero or undetectable at these low energies, rendering the calculation of lead equivalence invalid. Consequently, reliable comparison and interpretation of lead equivalence values are only possible at 356.0 keV and higher photon energies, where measurable LAC values were obtained. The corresponding relationship between tPb and relative percentage error (RPE) is illustrated in Figures 4.43, 4.44 and 4.45, demonstrating the variation of shielding performance with photon energy.

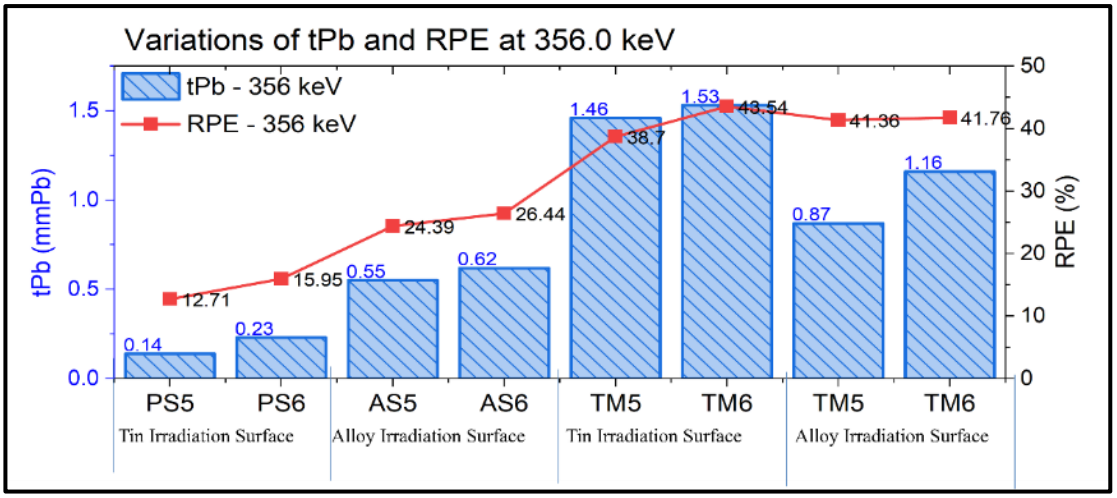


Figure 4.43 Variation of tPb and RPE of 50% and 60% Samples at 356.0 keV

From 356.0 keV to 834.8 keV, distinct variations in lead equivalent thickness were observed among the composite types and irradiation surfaces. The PS series (tin irradiation surface) exhibited the lowest tPb values, ranging from 1.012 mmPb to 4.527 mmPb, indicating relatively limited attenuation capability. Although these values suggest some degree of photon absorption, the shielding effectiveness remains modest due to the lower atomic number and density associated with the tin-based matrix. The gradual increase in tPb values with energy indicates that higher photon energies reduce the attenuation effectiveness of these composites.

The AS series (alloy irradiation surface) demonstrated moderate performance, with tPb values between 4.331 mmPb and 6.361 mmPb. This improvement relative to the PS series is attributed to the presence of multiple metallic elements within the alloy, which enhances photon absorption through an increased probability of interaction with high-Z constituents. Nevertheless, since lower tPb values correspond to superior

shielding performance, the AS series still required a thicker material layer to achieve equivalent attenuation compared to the TM series.

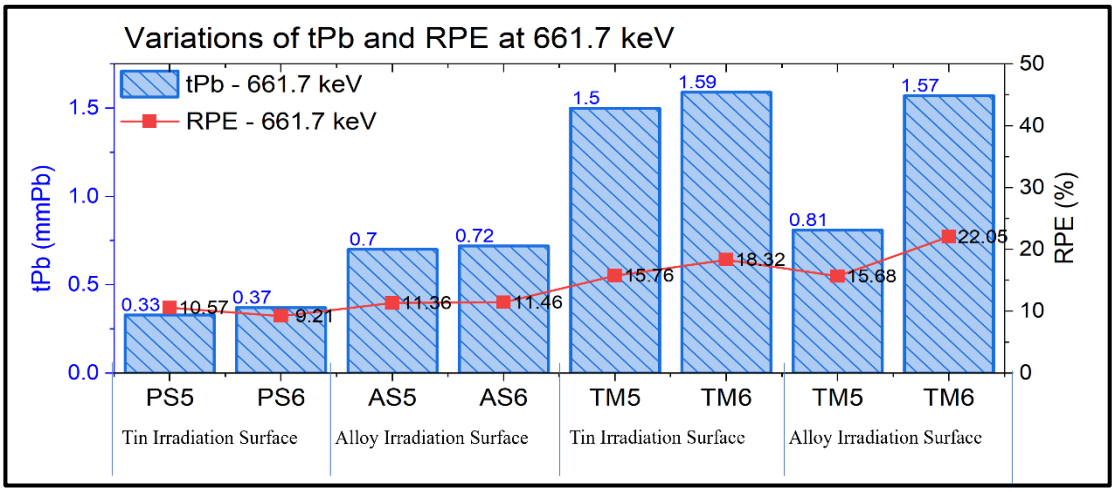


Figure 4.44 Variation of tPb and RPE of 50% to 60% Samples at 661.7 keV

The TM series displayed significantly higher tPb values, confirming its superior radiation attenuation capability compared to both PS and AS composites. Under tin irradiation, the TM samples achieved tPb values between 13.719 mmPb and 18.868 mmPb, whereas under alloy irradiation, the range was 7.651 mmPb to 17.426 mmPb. Among all samples tested, TM4 (tin irradiation surface) recorded the highest tPb value of 18.868 mmPb at 661.7 keV, representing the best shielding capability observed. This implies that TM4 could attenuate radiation as effectively as a lead sheet of 18.868 mm thickness, despite being a lighter, polymer-based composite. Such performance highlights the potential of TM composites for applications where both lightweight and effective radiation shielding are required.

A clear trend was observed where attenuation decreased as photon energy increased, particularly beyond 661.7 keV. This reduction in tPb values aligns with theoretical expectations, as photoelectric absorption diminishes and Compton scattering becomes the dominant interaction mechanism at higher photon energies, leading to reduced overall photon attenuation. Comparing the two irradiation conditions, it was evident that alloy-irradiated TM samples (particularly TM5 and TM6) consistently exhibited lower tPb values than their tin-irradiated counterparts. This suggests that alloy irradiation enhances photon attenuation efficiency by improving the uniformity of the material's energy absorption and scattering behavior. Among all the tested composites,

TM5 (alloy irradiation) demonstrated the most balanced performance, combining relatively low tPb values with consistent attenuation across the tested energy range, making it the most efficient and stable shielding composite.

At the highest photon energy of 834.8 keV (Figure 4.45), tPb values generally decrease for all samples as Compton scattering becomes dominant. The PS series maintains the lowest tPb values (0.23–0.40 mmPb), while the TM series retains the highest (0.90 – 1.56 mmPb). The RPE trend remains consistent, where samples with greater tPb (notably TM6 and TM5) also display higher RPE values (13.09 – 13.99%), signifying that these composites retain strong attenuation characteristics even under high-energy photon exposure.

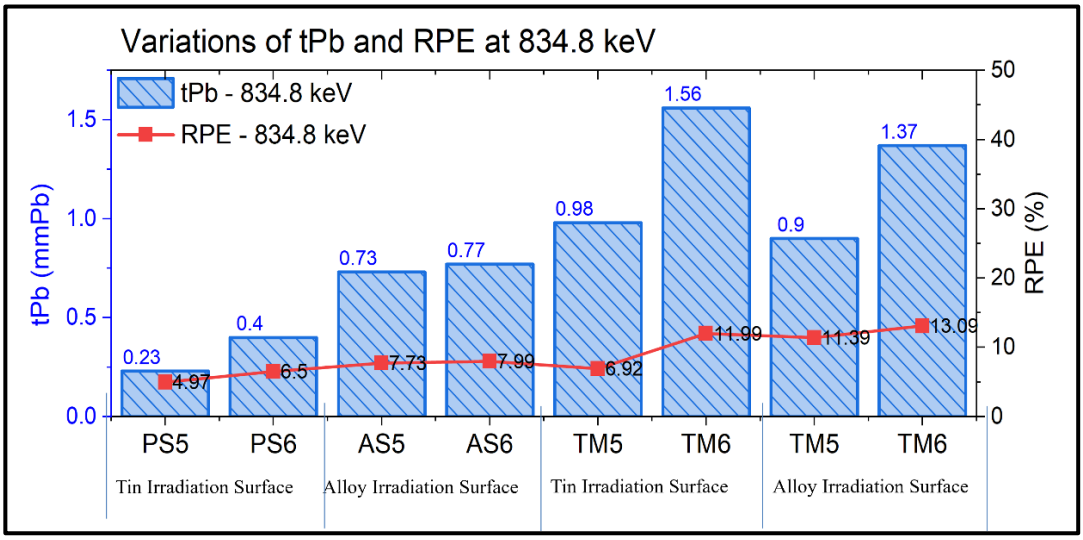


Figure 4.45 Variation of tPb and RPE of 50% to 60% Samples at 834.8 keV

Overall, the comparison of tPb and RPE across Figures 4.43 – 4.45 demonstrates that the TM series composites consistently achieve the highest RPE and moderately low tPb values relative to their attenuation performance. This correlation confirms that the TM composites, particularly TM5 and TM6 under alloy irradiation, exhibit the most effective combination of high photon absorption efficiency (indicated by higher RPE) and low lead equivalent thickness requirement (indicating better shielding per unit thickness).

In conclusion, among all tested samples, the TM5 composite under alloy irradiation provides the most favorable balance of high RPE and low tPb, confirming it as the best composite for radiation shielding at higher photon energies.

# CHAPTER 5
# CONCLUSIONS

## 5.1 Conclusion

The objectives set for this research were successfully achieved through a systematic experimental design and comprehensive analysis. The successful fabrication of the double-layered tin–PDMS composites represents the primary achievement of this study. The layering method produced uniform composite structures with strong interfacial adhesion between adjacent layers. The fabrication process proved effective in embedding metallic tin and tin alloy fillers within the PDMS matrix while maintaining the polymer's flexibility and integrity.

Comprehensive structural and morphological characterisation further confirmed the successful development of the composites. The elemental composition, surface morphology, chemical bonding and crystalline phases were systematically investigated using EDX, FESEM, FTIR and XRD analyses. The results confirmed uniform particle distribution without agglomeration, a smooth polymer surface, and excellent interfacial bonding between fillers and matrix. FTIR spectra showed no formation of new chemical bonds, verifying that the incorporation of tin did not alter the PDMS backbone, while XRD patterns identified the crystalline phases of tin and tin alloys, confirming successful filler integration.

The radiation shielding performance of the fabricated composites was comprehensively evaluated through gamma-ray attenuation studies. The results demonstrated a significant improvement in radiation absorption performance compared with pure PDMS, confirming the potential of the double-layered tin–PDMS composites for radiation shielding applications. Among all samples, the dual-filler TM6 composite exhibited the highest attenuation efficiency, with a linear attenuation coefficient of 16.81 $cm^{-1}$ and RPE of 96.5% at 88 keV. These findings demonstrate that the study has effectively met all objectives, establishing the layering method as a reliable approach for developing high-performance, lead-free tin–PDMS composites with superior radiation shielding capability.

The findings highlight the potential of tin–PDMS composites as lightweight, flexible, and environmentally friendly alternatives to conventional lead-based shields,

particularly for applications in medical imaging facilities such as protective aprons and shielding barriers. Other application is nuclear installations, radiation laboratories, and aerospace systems, where reduced toxicity, mechanical durability, and effective radiation protection are critical. Overall, the dual-filler layering strategy presents a promising and scalable pathway for the development of next-generation polymer-based radiation shielding materials.

## 5.2 Recommendation for Future Work

Although the present study successfully developed and characterised double-layered tin–PDMS composites for radiation shielding, several limitations encountered during fabrication and testing provide valuable insight for future improvement.

Maintaining a consistent layer thickness of 0.25 cm for each layer was one of the primary fabrication challenges. Variations in the viscosity and curing behaviour of PDMS containing high metal filler loadings made it difficult to achieve uniform thickness throughout the composite. Future work should optimise mould design and pouring techniques, possibly employing controlled casting or compression moulding methods to achieve uniform layer thickness and reproducibility.

Sedimentation of the tin alloy particles during curing represented another limitation of the fabrication process. Owing to the higher density of the alloy particles, gravitational settling occurred during curing, resulting in the formation of an unintended three-layer structure in the TM series. Future work should consider viscosity modification, faster curing systems, or dynamic stirring during the curing stage to prevent particle settling and maintain homogeneity throughout the composite.

Optimising the curing temperature was also a critical challenge during fabrication. Preliminary trials demonstrated that curing temperatures above the optimised range induced polymer shrinkage because of excessive thermal exposure, ultimately affecting the dimensional stability of the composite. Future studies should explore alternative curing protocols, such as stepwise or UV-assisted curing, to maintain dimensional stability while ensuring complete polymerisation.

By addressing these limitations, subsequent research can achieve greater fabrication consistency, structural integrity, and experimental reliability, further advancing the development of high-performance lead-free radiation shielding materials.

# REFERENCES


Abdullah, R., Aziz, S., Mamand, S., Hassan, A., Hussein, S., & Kadir, M. (2019). Reducing the Crystallite Size of Spherulites in PEO-Based Polymer Nanocomposites Mediated by Carbon Nanodots and Ag Nanoparticles. *Nanomaterials*, *9*(6), 874. https://doi.org/10.3390/nano9060874

AbuAlRoos, N. J., Baharul Amin, N. A., & Zainon, R. (2019). Conventional and new lead-free radiation shielding materials for radiation protection in nuclear medicine: A review. *Radiation Physics and Chemistry*, *165*, 108439. https://doi.org/10.1016/j.radphyschem.2019.108439

Abualroos, N. J., Idris, M. I., Ibrahim, H., Kamaruzaman, M. I., & Zainon, R. (2024). Physical, mechanical, and microstructural characterisation of tungsten carbide-based polymeric composites for radiation shielding application. *Scientific Reports*, *14*(1), 1375. https://doi.org/10.1038/s41598-023-49842-3

Adeniyi, A. G., & Ighalo, J. O. (2021). A systematic review of pure metals reinforced plastic composites. *Iranian Polymer Journal*, *30*(7), 751–768. https://doi.org/10.1007/s13726-021-00922-z

Ahmed, B., Shah, G. B., Malik, A. H., Aurangzeb, & Rizwan, M. (2020). Gamma-ray shielding characteristics of flexible silicone tungsten composites. *Applied Radiation and Isotopes*, *155*. https://doi.org/10.1016/j.apradiso.2019.108901

Akhdar, H. (2025). Theoretical Investigation of Photon Interaction and X-Ray Imaging Performance of PEEK-Based Composites for Medical Implants. *Polymers*, *17*(7), 996. https://doi.org/10.3390/polym17070996

Aladailah, M. W., Tashlykov, O. L., Volozheninov, T. P., Kaskov, D. O., Iuzbashieva, K. S., Al-Abed, R., Acikgoz, A., Yorulmaz, N., Yaşar, M. M., Al-Tamimi, W., & Alshipli, M. (2022). Exploration of physical and optical properties of ZnO nanopowders filled with polydimethylsiloxane (PDMS) for radiation shielding applications. Simulation and theoretical study. *Optical Materials*, *134*, 113197. https://doi.org/10.1016/j.optmat.2022.113197

Alanazi, S. F., Alotaibi, N. M., Alsuhybani, M., Alnassar, N., Almasoud, F. I., & Almurayshid, M. (2024a). Fabrication, Structural Characterization, and Photon Attenuation Efficiency Investigation of Polymer-Based Composites. *Polymers*, *16*(9), 1212. https://doi.org/10.3390/polym16091212

Alanazi, S. F., Alotaibi, N. M., Alsuhybani, M., Alnassar, N., Almasoud, F. I., &

Almurayshid, M. (2024b). Fabrication, Structural Characterization, and Photon Attenuation Efficiency Investigation of Polymer-Based Composites. *Polymers*, *16*(9). https://doi.org/10.3390/polym16091212

Al-Balushi, M. A., Ahmed, N. M., Zyoud, S. H., Ali, M. K. M., Akhdar, H., Aldaghri, O. A., & Ibnaouf, K. H. (2022). Ionization radiation shielding effectiveness of lead acetate, lead nitrate, and bismuth nitrate-doped zinc oxide nanorods thin films: A comparative evaluation. *Materials*, *15*(1). https://doi.org/10.3390/ma15010003

Al-Balushi, M. A., Ahmed, N. M., Zyoud, S. H., Mohammed Ali, M. K., Akhdar, H., Aldaghri, O. A., & Ibnaouf, K. H. (2021). Ionization Radiation Shielding Effectiveness of Lead Acetate, Lead Nitrate, and Bismuth Nitrate-Doped Zinc Oxide Nanorods Thin Films: A Comparative Evaluation. *Materials*, *15*(1), 3. https://doi.org/10.3390/ma15010003

Aldawood, S., Asemi, N. N., Kassim, H., Aziz, A. A., Saeed, W. S., & Al-Odayni, A.-B. (2024a). Gamma radiation shielding by titanium alloy reinforced by polymeric composite materials. *Journal of Radiation Research and Applied Sciences*, *17*(1), 100793. https://doi.org/10.1016/j.jrras.2023.100793

Aldawood, S., Asemi, N. N., Kassim, H., Aziz, A. A., Saeed, W. S., & Al-Odayni, A.-B. (2024b). Gamma radiation shielding by titanium alloy reinforced by polymeric composite materials. *Journal of Radiation Research and Applied Sciences*, *17*(1), 100793. https://doi.org/10.1016/j.jrras.2023.100793

Alım, B. (2020). A comprehensive study on radiation shielding characteristics of Tin-Silver, Manganin-R, Hastelloy-B, Hastelloy-X and Dilver-P alloys. *Applied Physics A*, *126*(4), 262. https://doi.org/10.1007/s00339-020-3442-7

Al-mugren, K. S., Almalki, L., Alshehri, R., Alamri, S., Almurayshid, M., Alsuhybani, M., Alharbi, R., & Khandaker, M. U. (2024). Development of lead-free metal carbides and ceramic decorated HDPE composites for low energy X-ray shielding applications. *Radiation Physics and Chemistry*, *220*. https://doi.org/10.1016/j.radphyschem.2024.111688

Almuqrin, A. H., Sayyed, M. I., Alorain, D. A., & Elsafi, M. (2024). Multilayer radiation shields for nuclear and radiological centers using free-lead materials and nanoparticles. *Annals of Nuclear Energy*, *200*, 110404. https://doi.org/10.1016/j.anucene.2024.110404

Almuqrin, A. H., Sayyed, M. I., Khandaker, M. U., & Elsafi, M. (2024). Exploring the

impact of Bi2O3 particle size on the efficacy of dimethylpolysiloxane for medical gamma/X-rays shielding applications. *Radiation Physics and Chemistry*, *220*. https://doi.org/10.1016/j.radphyschem.2024.111629

Almurayshid, M., Alsagabi, S., Alssalim, Y., Alotaibi, Z., & Almsalam, R. (2021). Feasibility of polymer-based composite materials as radiation shield. *Radiation Physics and Chemistry*, *183*. https://doi.org/10.1016/j.radphyschem.2021.109425

Alotaibi, F. A., Cornett, R. J., & Herod, M. N. (2021). Rapid and efficient autoclave digestion for the extraction of iodine-129 from urine samples. *Journal of Environmental Radioactivity*, *228*. https://doi.org/10.1016/j.jenvrad.2020.106528

Anderson, L., Govindaraj, P., Ang, A., Mirabedini, A., & Hameed, N. (2021). Modelling, fabrication and characterization of graphene/polymer nanocomposites for electromagnetic interference shielding applications. *Carbon Trends*, *4*, 47. https://doi.org/10.1016/j.cartre.2021.10

António, D., Di Maria, S., Matela, N., Vieira, S., & Vaz, P. (2020). Dose assessment and reconstruction algorithm optimization in simultaneous breast and lung CT imaging. *Radiation Physics and Chemistry*, *176*, 108972. https://doi.org/10.1016/j.radphyschem.2020.108972

Ariati, R., Sales, F., Souza, A., Lima, R. A., & Ribeiro, J. (2021). Polydimethylsiloxane Composites Characterization and Its Applications: A Review. *Polymers*, *13*(23), 4258. https://doi.org/10.3390/polym13234258

Ashraff Rosdi, M. A., Goh, P. S., Idris, F., Shalbi, S., Sarkawi, M. S., Mohd Ali, N. S., Jamsari, N. L., Ramli, A. S., & Azman, A. (2018). Neutron and gamma ray fluences measurement at radial Beam Port 1 of TRIGA MARK II PUSPATI research reactor. *IOP Conference Series: Materials Science and Engineering*, *298*(1). https://doi.org/10.1088/1757-899X/298/1/012033

Avcıoğlu, C. (2025). γ-Ray, Charged Particle, and Neutron Attenuation Characteristics of Cadmium-Containing 211 MAX Phase Carbides, M2CdC (M = Ti, Zr, and Hf). *ACS Omega*. https://doi.org/10.1021/acsomega.5c04825

Azman, M. N., Abualroos, N. J., Yaacob, K. A., & Zainon, R. (2023). Feasibility of nanomaterial tungsten carbide as lead-free nanomaterial-based radiation shielding. *Radiation Physics and Chemistry*, *202*, 110492. https://doi.org/10.1016/j.radphyschem.2022.110492

Behzadmehr, R., Doostkami, M., Sarchahi, Z., Dinparast Saleh, L., & Behzadmehr, R. (2021). Radiation protection among health care workers: knowledge, attitude,

practice, and clinical recommendations: a systematic review. *Reviews on Environmental Health*, *36*(2), 223–234. https://doi.org/10.1515/reveh-2020-0063

Bisht, N., Vishwakarma, J., Jaiswal, S., Kumar, P., Srivastava, A. K., Dhand, C., & Dwivedi, N. (2025). Synergizing chemistry: unveiling the potential of hybrid fillers for enhanced performance in shape memory polymers. *Advanced Composites and Hybrid Materials*, *8*(1), 7. https://doi.org/10.1007/s42114-024-01059-2

Bistričić, L., Borjanović, V., Mikac, L., & Dananić, V. (2013a). Vibrational spectroscopic study of poly(dimethylsiloxane)-ZnO nanocomposites. *Vibrational Spectroscopy*, *68*, 1–10. https://doi.org/10.1016/j.vibspec.2013.05.005

Bistričić, L., Borjanović, V., Mikac, L., & Dananić, V. (2013b). Vibrational spectroscopic study of poly(dimethylsiloxane)-ZnO nanocomposites. *Vibrational Spectroscopy*, *68*, 1–10. https://doi.org/10.1016/j.vibspec.2013.05.005

Boice, J., Dauer, L. T., Kase, K. R., Mettler, F. A., & Vetter, R. J. (2020). Evolution of radiation protection for medical workers. *The British Journal of Radiology*, *93*(1112). https://doi.org/10.1259/bjr.20200282

Brown, K. (2020). Introduction to Health Physics, 5th Edition. Author: Thomas E.Johnson. McGraw-Hill Education, New York, 2017. Paperback: 944 pp. Price: $66.51. ISBN 9780071835275. *Medical Physics*, *47*(4), 2044–2044. https://doi.org/10.1002/mp.13777

Buonanno, M., Grilj, V., & Brenner, D. J. (2019). Biological effects in normal cells exposed to FLASH dose rate protons. *Radiotherapy and Oncology*, *139*, 51–55. https://doi.org/10.1016/j.radonc.2019.02.009

Burns, K. M., Shoag, J. M., Kahlon, S. S., Parsons, P. J., Bijur, P. E., Taragin, B. H., & Markowitz, M. (2017). Lead Aprons Are a Lead Exposure Hazard. *Journal of the American College of Radiology*, *14*(5), 641–647. https://doi.org/10.1016/j.jacr.2016.10.024

Calderón - Gerstein, W. S., & Torres - Samaniego, G. (2021). High altitude and cancer: An old controversy. In *Respiratory Physiology and Neurobiology* (Vol. 289). Elsevier B.V. https://doi.org/10.1016/j.resp.2021.103655

Cardis, E., Vrijheid, M., Blettner, M., Gilbert, E., Hakama, M., Hill, C., Howe, G., Kaldor, J., Muirhead, C. R., Schubauer-Berigan, M., Yoshimura, T., Bermann, F., Cowper, G., Fix, J., Hacker, C., Heinmiller, B., Marshall, M., Thierry-Chef, I., Utterback, D., … Veress, K. (2005). Risk of cancer after low doses of ionising

radiation: retrospective cohort study in 15 countries. *BMJ*, *331*(7508), 77. https://doi.org/10.1136/bmj.38499.599861.E0

Chang, Q., Guo, S., & Zhang, X. (2023). Radiation shielding polymer composites: Ray-interaction mechanism, structural design, manufacture and biomedical applications. In *Materials and Design* (Vol. 233). Elsevier Ltd. https://doi.org/10.1016/j.matdes.2023.112253

Chen, S., Nambiar, S., Li, Z., Osei, E., Darko, J., Zheng, W., Sun, Z., Liu, P., & Yeow, J. T. W. (2019). Bismuth oxide-based nanocomposite for high-energy electron radiation shielding. *Journal of Materials Science*, *54*(4), 3023–3034. https://doi.org/10.1007/s10853-018-3063-0

Chen, S., Zhou, F., Reggetz, B. N., Lee, E. G., Virji, M. A., Afshari, A., Jun, M. B. G., & Akin, S. (2025). Polymer metallization via cold spray: an investigation into the effects of particle hardness and morphology. *Manufacturing Letters*, *44*, 325–331. https://doi.org/10.1016/j.mfglet.2025.06.039

Chen, Z., Li, X., Lu, L., Yuan, B., Wang, L., Li, Z., & Li, H. (2023). Non-Toxic and Flexible Radiation-Shielding Composites Based on Natural Rubber Containing Elemental W Fillers for Efficient Shielding against X/γ-rays. *Processes*, *11*(3), 674. https://doi.org/10.3390/pr11030674

Dai, Z., Ansaloni, L., & Deng, L. (2016). Recent advances in multi-layer composite polymeric membranes for CO2 separation: A review. *Green Energy & Environment*, *1*(2), 102–128. https://doi.org/10.1016/j.gee.2016.08.001

Daniel, O. A., & Xaviera, I. C. (2018). Integrity test of lead apron and its effect on personnel and carers. *Bangabandhu Sheikh Mujib Medical University Journal*, *11*(1), 34–37. https://doi.org/10.3329/bsmmuj.v11i1.35360

Deng, W. M., Zhao, Y. J., Cao, Y. T., Lv, P., Zhang, S., Zhao, J. T., Zhang, L. M., Wang, T. S., & Chen, L. (2023). Mechanical property changes of borosilicate glass induced by mono and sequential ion-irradiations. *Journal of Non-Crystalline Solids*, *622*. https://doi.org/10.1016/j.jnoncrysol.2023.122685

Dikra, B., Fellah, M., Barille, R., Weiß, S., Abdul Samad, M., Alburaikan, A., Abd El-Wahed khalifa, H., & Obrosov, A. (2024a). Improvement of photocatalytic performance and sensitive ultraviolet photodetectors using AC-ZnO/ZC-Ag2O/AZ-CuO multilayers nanocomposite prepared by spin coating method. *Journal of Science: Advanced Materials and Devices*, *9*(1). https://doi.org/10.1016/j.jsamd.2023.100642

Dikra, B., Fellah, M., Barille, R., Weiß, S., Abdul Samad, M., Alburaikan, A., Abd El-Wahed khalifa, H., & Obrosov, A. (2024b). Improvement of photocatalytic performance and sensitive ultraviolet photodetectors using AC-ZnO/ZC-Ag2O/AZ-CuO multilayers nanocomposite prepared by spin coating method. *Journal of Science: Advanced Materials and Devices*, *9*(1). https://doi.org/10.1016/j.jsamd.2023.100642

Ding, Z., Wang, H., Luo, J., & Li, N. (2021). A review on forming technologies of fibre metal laminates. *International Journal of Lightweight Materials and Manufacture*, *4*(1), 110–126. https://doi.org/10.1016/j.ijlmm.2020.06.006

Domenech, H. (2017). Shielding. In *Radiation Safety* (pp. 97–109). Springer International Publishing. https://doi.org/10.1007/978-3-319-42671-6_7

El-Khatib, A. M., Abbas, M. I., Hammoury, S. I., Gouda, M. M., Zard, K., & Elsafi, Mohamed. (2022). Effect of PbO-nanoparticles on dimethyl polysiloxane for use in radiation shielding applications. *Scientific Reports*, *12*(1), 15722. https://doi.org/10.1038/s41598-022-20103-z

El-Khatib, A. M., Alabsy, M. T., El-Khatib, A. Y., Dib, M. F., & Abbas, M. I. (2024). Superiority of micro/nano tungsten carbide reinforced poly-methyl methacrylate composites in shielding gamma radiation. *Nuclear Engineering and Technology*, *56*(10), 4103–4114. https://doi.org/10.1016/j.net.2024.05.013

El-Khatib, A. M., Zard, K., Abbas, M. I., & Gouda, M. M. (2024a). Novel composite based on silicone rubber and a nano mixture of SnO2, Bi2O3, and CdO for gamma radiation protection. *Scientific Reports*, *14*(1), 1578. https://doi.org/10.1038/s41598-024-51965-0

El-Khatib, A. M., Zard, K., Abbas, M. I., & Gouda, M. M. (2024b). Novel composite based on silicone rubber and a nano mixture of SnO2, Bi2O3, and CdO for gamma radiation protection. *Scientific Reports*, *14*(1). https://doi.org/10.1038/s41598-024-51965-0

Farahani, S., Pradeep, S. A., & Pilla, S. (2020). Integration Concept of Injection, Forming and Foaming: A Practical Approach to Manufacture Hybrid Structures. In *Advances in Polymer Processing 2020* (pp. 205–218). Springer Berlin Heidelberg. https://doi.org/10.1007/978-3-662-60809-8_17

Fidan, M., Acikgoz, A., Demircan, G., Yilmaz, D., & Aktas, B. (2022). Optical, structural, physical, and nuclear shielding properties, and albedo parameters of TeO2–BaO–B2O3–PbO–V2O5 glasses. *Journal of Physics and Chemistry of*

*Solids*, *163*, 110543. https://doi.org/10.1016/j.jpcs.2021.110543

Ghule, P. G., Bholane, G. T., Joshi, R. P., Dahiwale, S. S., Shelke, P. N., & Dhole, S. D. (2024). Gamma radiation shielding properties of unsaturated polyester /Bi2O3 composites: An experimental, theoretical and simulation approach. *Radiation Physics and Chemistry*, *216*, 111452. https://doi.org/10.1016/j.radphyschem.2023.111452

Gilys, L., Griškonis, E., Griškevičius, P., & Adlienė, D. (2022). Lead Free Multilayered Polymer Composites for Radiation Shielding. *Polymers*, *14*(9), 1696. https://doi.org/10.3390/polym14091696

Glaser, M., Matthes, S., Hildebrand, J., Pierre Bergmann, J., & Schaaf, P. (2023). Hybrid Thermoplastic-Metal joining based on Al/Ni multilayer foils – Analysis of the joining zone. *Materials & Design*, *226*, 111561. https://doi.org/10.1016/j.matdes.2022.111561

Gouda, M. M., Abbas, M. I., Hammoury, S. I., Zard, K., & M.El-Khatib, A. (2023). Nano tin oxide/dimethyl polysiloxane reinforced composite as a flexible radiation protecting material. *Scientific Reports*, *13*(1), 210. https://doi.org/10.1038/s41598-023-27464-z

Graeff, C., Volz, L., & Durante, M. (2023). Emerging technologies for cancer therapy using accelerated particles. *Progress in Particle and Nuclear Physics*, *131*, 104046. https://doi.org/10.1016/j.ppnp.2023.104046

Gurumurthi, S. H. P., & Rajasekar, V. (2025). Comparative Analysis of Effectiveness of Traditional Lead Aprons versus Newer Generation Lead-free Aprons in Radiation Protection. *Journal of Medical Physics*, *50*(1), 1–7. https://doi.org/10.4103/jmp.jmp_152_24

Hamouni, S., Arous, O., Abdessemed, D., Nezzal, G., & Van der Bruggen, B. (2019). Alcohol and Alkane Organic Extraction Using Pervaporation Process. *Macromolecular Symposia*, *386*(1). https://doi.org/10.1002/masy.201800247

Hubbell, J., & Seltzer, S. (1995). *Tables of X-Ray Mass Attenuation Coefficients and Mass Energy-Absorption Coefficients 1 keV to 20 MeV for Elements Z = 1 to 92 and 48 Additional Substances of Dosimetric Interest*. http://physics.nist.gov/PhysRefData/XrayMassCoef/cover.html.

Hussain, H. S., Al-Bayati, A. hussain A., & Jaffer, H. I. (2011). Dependence of gamma-ray absorption coefficient on the size of lead particle. *Baghdad Science Journal*, *8*(2), 613–617. https://doi.org/10.21123/bsj.2011.8.2.613-617

I. J. Boniface, & N. M. A. Mukhtar. (2020). A Study on the Importance of Personal Protective Equipment (PPE) Use in Occupational Radiation Protection. *Virtual Science Invention Innovation Conference (SIIC)*, (9), 291–294. https://ir.uitm.edu.my/id/eprint/81553/1/81553.pdf

*IAEA Safety Standards for protecting people and the environment General Safety Guide No. GSG-7 Occupational Radiation Protection Jointly sponsored by*. (n.d.). Retrieved http://www-ns.iaea.org/standards/

J. A. Kamarolzeman, & N. M. A, M. (2020). A Review on The Personal Protective Equipment (PPE) Used in Occupational Radiation Protective. *Virtual Science Invention Innovation Conference (SIIC)*, (9), 299–300. https://ir.uitm.edu.my/id/eprint/81553/1/81553.pdf

Jadav, G. L., Aswal, V. K., & Singh, P. S. (2013). Preparation of bifunctional poly(dimethylsiloxane) membrane by dual X-linking. *Journal of Materials Chemistry A*, *1*(15), 4893. https://doi.org/10.1039/c3ta10358g

Jamal AbuAlRoos, N., Azman, M. N., Baharul Amin, N. A., & Zainon, R. (2020a). Tungsten-based material as promising new lead-free gamma radiation shielding material in nuclear medicine. *Physica Medica*, *78*, 48–57. https://doi.org/10.1016/j.ejmp.2020.08.017

Jamal AbuAlRoos, N., Azman, M. N., Baharul Amin, N. A., & Zainon, R. (2020b). Tungsten-based material as promising new lead-free gamma radiation shielding material in nuclear medicine. *Physica Medica*, *78*, 48–57. https://doi.org/10.1016/j.ejmp.2020.08.017

Jayakumar, S., Saravanan, T., & Philip, J. (2023). A review on polymer nanocomposites as lead-free materials for diagnostic X-ray shielding: Recent advances, challenges and future perspectives. *Hybrid Advances*, *4*, 100100. https://doi.org/10.1016/j.hybadv.2023.100100

Jung, J., Yoon, S., Kim, B., & Kim, J. B. (2023). Development of High-Performance Flexible Radiative Cooling Film Using PDMS/TiO2 Microparticles. *Micromachines*, *14*(12). https://doi.org/10.3390/mi14122223

Kaewpirom, S., Chousangsuntorn, K., & Boonsang, S. (2022). Evaluation of Micro- and Nano-Bismuth(III) Oxide Coated Fabric for Environmentally Friendly X-Ray Shielding Materials. *ACS Omega*, *7*(32), 28248–28257. https://doi.org/10.1021/acsomega.2c02578

Kamislioglu, M., Kupeli, D., Buyuk, B., & Kocak, I. (2025). Studies of novel

tungsten-embedded silicone rubber flexible materials for diagnostic x-ray protection. *Physica Scripta*, *100*(12), 125301. https://doi.org/10.1088/1402-4896/ae2298

Kato, M., Chida, K., Munehisa, M., Sato, T., Inaba, Y., Suzuki, M., & Zuguchi, M. (2021). Non-Lead Protective Aprons for the Protection of Interventional Radiology Physicians from Radiation Exposure in Clinical Settings: An Initial Study. *Diagnostics*, *11*(9), 1613. https://doi.org/10.3390/diagnostics11091613

Kellens, P.-J., De Hauwere, A., Gossye, T., Peire, S., Tournicourt, I., Strubbe, L., De Pooter, J., & Bacher, K. (2022). Integrity of personal radiation protective equipment (PRPE): a 4-year longitudinal follow-up study. *Insights into Imaging*, *13*(1), 183. https://doi.org/10.1186/s13244-022-01323-3

Kim, S.-C. (2023). Metal Particle Pencil Beam Spray-Coating Method for High-Density Polymer–Resin Composites: Evaluation of Radiation-Shielding Sheet Properties. *Materials*, *16*(18), 6092. https://doi.org/10.3390/ma16186092

Kumar, L., Kumar, P., Narayan, A., & Kar, M. (2013). Rietveld analysis of XRD patterns of different sizes of nanocrystalline cobalt ferrite. *International Nano Letters*, *3*(1), 8. https://doi.org/10.1186/2228-5326-3-8

Kwon, D. E., Han, D. H., Kim, J. O., Jung, K. H., & Baek, C. H. (2023). Multi-layered structures for lightweight providing shielding from unintended radiation exposure for pediatric patients. *Radiation Physics and Chemistry*, *204*. https://doi.org/10.1016/j.radphyschem.2022.110720

Laysandra, L., Bazliah, D., Sentosa, D. M., Heksa, A. C., Bui, H.-K., Li, Y.-C., & Chiu, Y.-C. (2025). The rise of rubber-like synthetic polymers in next-gen transistor technologies. *Chemical Science*, *16*(43), 20181–20228. https://doi.org/10.1039/D5SC05680B

Li, Y., Wu, D., Zhang, Y., Wang, L., & Xue, S. (2021). Effects of trace oxygen content on microstructure and performances of Au-20Sn/Cu solder joints. *Crystals*, *11*(6). https://doi.org/10.3390/cryst11060601

Libeesh, N. K., Naseer, K. A., Mahmoud, K. A., Sayyed, M. I., Arivazhagan, S., Alqahtani, M. S., Yousef, E. S., & Khandaker, M. U. (2022). Applicability of the multispectral remote sensing on determining the natural rock complexes distribution and their evaluability on the radiation protection applications. *Radiation Physics and Chemistry*, *193*, 110004. https://doi.org/10.1016/j.radphyschem.2022.110004

Lunsford, T. R., & Contoyannis, B. (2019). Materials Science. *Atlas of Orthoses and Assistive Devices, Fifth Edition*, 7–41. https://doi.org/10.1016/B978-0-323-48323-0.00002-0

Mahmoud, K. A., Lacomme, E., Sayyed, M. I., Özpolat, F., & Tashlykov, O. L. (2020). Investigation of the gamma ray shielding properties for polyvinyl chloride reinforced with chalcocite and hematite minerals. *Heliyon*, *6*(3). https://doi.org/10.1016/j.heliyon.2020.e03560

McGinley, Patton H., Miner, & Marc S. (1995). A History of Radiation Shielding of X-Ray Therapy Rooms. *Health Physics* , *65*(5), 759–765.

Mohammed, S. I., & Mosa, Z. Q. (2025). Theoretical Calculation of Radiation Shielding Properties of B2O3–Bi2O3–Al2O3–MgO Glasses Alloyed with MnO. *Baghdad Science Journal*, *22*(5), 1578–1585. https://doi.org/10.21123/bsj.2024.10508

More, C. V., Alsayed, Z., Badawi, Mohamed. S., Thabet, Abouzeid. A., & Pawar, P. P. (2021a). Polymeric composite materials for radiation shielding: a review. *Environmental Chemistry Letters*, *19*(3), 2057–2090. https://doi.org/10.1007/s10311-021-01189-9

More, C. V., Alsayed, Z., Badawi, Mohamed. S., Thabet, Abouzeid. A., & Pawar, P. P. (2021b). Polymeric composite materials for radiation shielding: a review. *Environmental Chemistry Letters*, *19*(3), 2057–2090. https://doi.org/10.1007/s10311-021-01189-9

N. M. A. Mukhtar, A. Mahmood, A. N. Suhaimi, N. F. H. Noor Azman, J. A. Kamarolzerman, I. J. Boniface, & A. Safian. (2024). The Effects of Educational Level on Radiation Professionals' Knowledge and Implimentation of ALARA Principles For Occupational Radiation Protection. *Journal of Islamic, Social, Economics and Development (JISED)*, *9*(60), 82–92. https://doi.org/10.55573/jised.096010

Nagaraja, N., Manjunatha, H. C., Seenappa, L., Sridhar, K. N., & Ramalingam, H. B. (2020). Radiation shielding properties of silicon polymers. *Radiation Physics and Chemistry*, *171*, 108723. https://doi.org/10.1016/j.radphyschem.2020.108723

Nakamura, K., Kubo, K., Hirata, M., Sakai, Y., Nakamura, Y., Kosaka, H., & Monzen, H. (2024a). Evaluation of the shielding effectiveness of a non-toxic, double-layered BaSO4/W composite against diagnostic X-rays. *Radiation Physics and Chemistry*, *219*, 111684.

https://doi.org/10.1016/j.radphyschem.2024.111684

Nakamura, K., Kubo, K., Hirata, M., Sakai, Y., Nakamura, Y., Kosaka, H., & Monzen, H. (2024b). Evaluation of the shielding effectiveness of a non-toxic, double-layered BaSO4/W composite against diagnostic X-rays. *Radiation Physics and Chemistry*, *219*. https://doi.org/10.1016/j.radphyschem.2024.111684

Nambiar, S., & Yeow, J. T. W. (2012). Polymer-Composite Materials for Radiation Protection. *ACS Applied Materials & Interfaces*, *4*(11), 5717–5726. https://doi.org/10.1021/am300783d

Nanda Karmaker, Kazi M. Maraz, Farhana Islam, Md. Marjanul Haque, Md. Razzak, M.Z.I. Mollah, M. R. I. Faruque, & Ruhul A. Khan. (2021a). Fundamental characteristics and application of radiation. *GSC Advanced Research and Reviews*, *7*(1), 064–072. https://doi.org/10.30574/gscarr.2021.7.1.0043

Nanda Karmaker, Kazi M. Maraz, Farhana Islam, Md. Marjanul Haque, Md. Razzak, M.Z.I. Mollah, M. R. I. Faruque, & Ruhul A. Khan. (2021b). Fundamental characteristics and application of radiation. *GSC Advanced Research and Reviews*, *7*(1), 064–072. https://doi.org/10.30574/gscarr.2021.7.1.0043

Nanda Karmaker, Kazi M. Maraz, Farhana Islam, Md. Marjanul Haque, Md. Razzak, M.Z.I. Mollah, M. R. I. Faruque, & Ruhul A. Khan. (2021c). Fundamental characteristics and application of radiation. *GSC Advanced Research and Reviews*, *7*(1), 064–072. https://doi.org/10.30574/gscarr.2021.7.1.0043

Nazeri, A. A., Malekzadeh, R., Mehnati, P., & Refahi, S. (2025). The Effects of Single and Bimetallic Silicon Composite Shields in Medical Imaging Methods: A Monte Carlo Study. *Frontiers in Biomedical Technologies*, *12*(1), 127–135. https://doi.org/10.18502/fbt.v12i1.17741

Nguyen, K.-N., Sao, L., Kyllo, K., Hernandez, D., Salomon, S., Shah, K., Oh, D., & Kao, K. C. (2024). Antibiofilm Activity of PDMS/TiO2 against Candida glabrata through Inhibited Hydrophobic Recovery. *ACS Omega*, *9*(41), 42593–42601. https://doi.org/10.1021/acsomega.4c07869

Nikeghbal, K., Zamanian, Z., Shahidi, S., Spagnuolo, G., & Soltani, P. (2020). Designing and Fabricating Nano-Structured and Micro-Structured Radiation Shields for Protection against CBCT Exposure. *Materials*, *13*(19), 4371. https://doi.org/10.3390/ma13194371

Occupational Safety and Health Administration U.S. Department of Labor. (2005). *Best Practices for Hospital-Based First Receivers of Victims from Mass Casualty*

# AUTHOR'S PROFILE



Nurul Syafiqah Binti Roslan began her academic journey by completing her Foundation in Science at the Foundation Centre, Universiti Teknologi MARA in 2019. She obtained her Bachelor of Science (Hons.) in Materials Science and Technology from Universiti Teknologi MARA in 2024. She is currently pursuing her Master of Science in Materials Science and Technology at the same institution. Her postgraduate research focuses on the development and radiation shielding performance of double layer metal–polymer composites, particularly tin-filled polydimethylsiloxane (PDMS). Her work involves material characterisation techniques such as Fourier Transform Infrared Spectroscopy (FTIR), X-ray Diffraction (XRD), Field Emission Scanning Electron Microscopy (FESEM), and gamma ray spectroscopy to evaluate structural morphology and shielding efficiency of the fabricated samples. In addition, a hardness test and thermal analysis technique (TGA) have also been carried out for the optimised samples.

## LIST OF PUBLICATIONS

**Roslan, N. S**., Mukhtar, N. M. A., Mahmood, A., Wahab, N. A. A., Zainon, R., Abidin, H. Z., Shah, A. Z., & Izaham, N. I. N. (2026). Double-Layered Tin-Polydimethylsiloxane (PDMS) Composites: Evaluation of Porosity and Structural Morphology of Polymeric Composites. *Baghdad Science Journal*, *23*(1), 138–150. https://doi.org/10.21123/2411-7986.5141

**Roslan, N. S.,** Mukhtar, N. M. A., Mahmood, A., Wahab, N. A. A., Zainon, R., & Abidin, H. Z. (2024). Fabrication and analysis of tin-polydimethylsiloxane

(PDMS) composite layers for enhanced radiation shielding: An alternative to lead (Pb) material [Extended abstract]. International Journal of Applied Health Science, 8(3), Supplement.

**Roslan, N. S**., Mukhtar, N. M. A., Zainal Abidin, H., Mahmood, A., & Abdul Wahab, N. A. (2025). Double-layer tin-PDMS composites: A novel shielding absorber for radiation protection against gamma rays [Extended abstract]. In 3rd International Invention, Innovation and Design Expo (INoDEx 2025) e-proceedings book (pp. 194–200).

Abidin, H. Z., Mukhtar, N. M. A., Mahmood, A., Abdul Wahab, N. A., Zainon, R., **Roslan, N. S**., Nor Izaham, N. I., & Shah, A. Z. (2025). Effect of tin filler composition on porosity in tin-polydimethylsiloxane composites. Pure and Applied Chemistry, 97(8), 825–840. https://doi.org/10.1515/pac-2024-0347

Abidin, H. Z., Mukhtar, N. M. A., Mahmood, A., Abdul Wahab, N. A., Zainon, R., **Roslan, N. S**., Nor Izaham, N. I., & Shah, A. Z. (2025). Porosity and structural integrity of tin-polydimethylsiloxane (PDMS) composites for radiation shielding application. Baghdad Science Journal, 23(1), Article 10. https://doi.org/10.21123/2411-7986.5143

Abidin, H. Z., Mukhtar, N. M. A., **Roslan, N. S**., Mahmood, A., & Abdul Wahab, N. A. (2025). Radiation shielding properties of tin-polydimethylsiloxane (PDMS) composites against gamma ray at 356 keV. International Journal of Innovation and Industrial Revolution, 7(20), 356–369. https://doi.org/10.35631/IJIREV.720023

Abidin, H. Z., Mukhtar, N. M. A., **Roslan, N. S**., Mahmood, A., & Abdul Wahab, N. A. (2024). Tin-PDMS composite: Innovative structure as a shield against ionising radiation [Extended abstract]. International Journal of Applied Health Science, 8(3), Supplement.

Abidin, H. Z., Mukhtar, N. M. A., **Roslan, N. S**., Mahmood, A., & Abdul Wahab, N. A. (2025). Lead-free tin-PDMS-based composite: A novel metal-polymeric material for radiation [Extended abstract]. In 3rd International Invention, Innovation and Design Expo (INoDEx 2025) e-proceedings book (pp. 188–193).

Abidin, H. Z., **Roslan, N. S**., Nor Izaham, N. I., Mahmood, A., Mukhtar, N. M. A., & Zainon, R. (2024). TiPhAny: Innovative teaching aids for engaging learning on

thermodynamics topics. In International Teaching Assistant Competition (ITAC2024) e-proceedings.

## LIST OF CONFERENCE ATTENDED

| No | Title Presented | Conference Name | Location | Date | Role |
|---|---|---|---|---|---|
| 1 | Double-Layered Tin-Polydimethylsiloxane (PDMS) Evaluation of Porosity and Structural Morphology of Polymeric Composites | International Conference on Discoveries in Applied Sciences & Advanced Technology 2025 (Dasat 2025) | Resort World Awana, Genting Highland, Pahang, Malaysia | 6-7 February 2025 | Presenter |
| 2 | - | 9th International Conference for Young Chemists (ICYC 2024) | Bayview Hotel, George Town, Penang, Malaysia | 9-11 October 2024 | Attendee |

## LIST OF COPYRIGHTS

| No. | Title | Copyright ID | Year |
|---|---|---|---|
| 1 | Fabrication and Analysis of Tin-Polydimethylsiloxane (PDMS) Composite Layers for Enhanced Radiation Shielding: An Alternative to Lead (Pb) Material | CRLY2024P03669 | 2024 |
| 2 | An Innovation of The Double Layer Polymeric Composites Enriched with Tin Fillers As Radiation Shielding Material at Low Energy Gamma Rays | CRLY2025P00378 | 2025 |
| 3 | Double-Layer Tin-PDMS Composites: A Novel Shielding Absorber for Radiation Protection Against Gamma Rays | CRLY2025P06218 | 2025 |
| 4 | Tin-PDMS Composite: Innovative Structure As a Shield Against Ionizing Radiation | CRLY2024P03668 | 2024 |

| | | | |
|---|---|---|---|
| 5 | Tin-Reinforced Polydimethylsiloxane Composites: A Lead Free Innovation for Superior Gamma Radiation Shielding | CRLY2025P003709 | 2025 |
| 6 | Lead-Free Tin-PDMS-Based Composite: A Novel Metal-Polymeric Material for Radiation Shielding | CRLY2025P06217 | 2025 |
| 7 | NMaM method: An Innovative Mix-Mixing Method of Nano-Microparticle Tin-PDMS-Based Composite to Block Radiation Penetration | CRLY2024P03665 | 2024 |
| 8 | TiPhAny: Innovative Teaching Aids for Engaging Learning on Thermodynamics Topics | CRLY2024P03665 | 2024 |

## LIST OF INNOVATION AWARDS

| No. | Innovation Competition | Innovation Project | Medal of the award |
|---|---|---|---|
| 1 | 3rd International Invention, Innovation and Design (INoDEx 2025)<br><br>Organised by: Institute of Nano Optoelectronics Research and Technology (INOR) | Double-Layer Tin-PDMS Composites: A Novel Shielding Absorber for Radiation Protection Against Gamma Rays | ***Diamond**<br><br>Gold |
| 2 | The 6th Malaysia-Japan International Conference on Nanoscience, Nanotechnology, and Nanoengineering (MJIC 2025)<br><br>Organised by: Institute of Science at Universiti Teknologi MARA (UiTM) | An Innovation of The Double Layer Polymeric Composites Enriched with Tin Fillers As Radiation Shielding Material at Low Energy Gamma Rays | Gold |
| 3 | IIUM Research & Innovation Day 2024 (IRID 2024)<br><br>Organised by: Research Management Centre, International Islamic University Malaysia (IIUM) | Tin-PDMS Composite: Innovative Structure As a Shield Against Ionizing Radiation | Gold |
| 4 | The 6th Malaysia-Japan International Conference on Nanoscience, Nanotechnology, and Nanoengineering (MJIC 2025) | Tin-Reinforced Polydimethylsiloxane Composites: A Lead Free Innovation for Superior | Gold |

| | | | |
|---|---|---|---|
| | Organised by: Institute of Science at Universiti Teknologi MARA (UiTM) | Gamma Radiation Shielding | |
| 5 | 3rd International Invention, Innovation and Design (INoDEx 2025)<br><br>Organised by: Institute of Nano Optoelectronics Research and Technology (INOR) | Lead-Free Tin-PDMS-Based Composite: A Novel Metal-Polymeric Material for Radiation Shielding | Gold |
| 6 | INNOMed 2025: Innovation Pitching Powered by PERANTIM<br><br>Organised by: Pihak Berkuasa Peranti Perubatan, Kementerian Kesihatan Malaysia (KKM) | NMaM method: An Innovative Mix-Mixing Method of Nano-Microparticle Tin-PDMS-Based Composite to Block Radiation Penetration | Gold |
| 7 | International Teaching Aid Competition 2024 (ITAC 2024)<br><br>Organised by: Special Interest Group – Public Interest Centre of Excellence (SIG – PICE) of Universiti Teknologi MARA Kedah | TiPhAny: Innovative Teaching Aids for Engaging Learning on Thermodynamics Topics | Silver |
| 8 | IIUM Research & Innovation Day 2024 (IRID 2024)<br><br>Organised by: Research Management Centre, International Islamic University Malaysia (IIUM) | Fabrication and Analysis of Tin-Polydimethylsiloxane (PDMS) Composite Layers for Enhanced Radiation Shielding: An Alternative to Lead (Pb) Material | Bronze |
| 9 | UiTM Postgraduate Image Competition 2025<br><br>Organised by: Special Interest Group - Advanced Mechanics Research (SIG – ADMECH) of Universiti Teknologi MARA Penang | Field Emission Scanning Electron Microscopy (FESEM) Analysis of a Novel Tin- Polydimethylsiloxane (PDMS) Composite for Radiation Shielding Applications | - |